GRAIN REFINEMENT OF AUSTENITIC STAINLESS STEEL WELDS TO FACILITATE ULTRASONIC INSPECTION

By
Nicholas Harvey Tyas
Magdalene College
Cambridge

A dissertation submitted for the degree of
Doctor of Philosophy
at the University of Cambridge
May 2000

"Excellent. Continue the research."

— MONTGOMERY BURNS, Springfield (1994)

Asked why there were so few scientists from the Black Country, he replied, "Mate, we'um blessed with the gift of perfect vision, but cursed by the inability to look."

— STEPHEN SILVESTER, Dudley (1999)

Preface

This dissertation is submitted for the degree of Doctor of Philosophy in Natural Sciences at the University of Cambridge. It contains an account of research carried out between October 1996 and May 2000 at the Department of Materials Science and Metallurgy, Cambridge, under the supervision of Prof. H.K.D.H. Bhadeshia. Except where appropriately referenced or acknowledged, the work is original and is not the result of collaboration. Neither this, nor any substantially similar dissertation has been, or is currently being, submitted for any degree, diploma or other qualification at this or any other university. This dissertation contains less than 60,000 words.

N. Tyas

Nicholas Tyas

May 2000

Acknowledgements

I wish to thank Prof. A. Windle for the provision of laboratory facilities in the Department of Materials Science and Metallurgy at the University of Cambridge. I am indebted to Harry Bhadeshia for his encouragement and enthusiasm throughout the course of my research.

I would like to thank both the EPSRC and BNFL for providing financial support for this project, and especially Brian Quayle of BNFL's Materials and NDT Development Section for helpful discussions and the interest he has shown in this work.

I am also most grateful to the scientists and technical staff throughout the department, the country and even the world (!) who have graciously lent their assistance whenever required, particularly Dr. A. Leonard (Project Leader) and Mr. C. Hardy (Welding Technician) of TWI for their involvement in the planning and performing of the welding experiments, Prof. F. DiSalvo and Dr. L. Cario of Cornell University for the preparation and supply of CeN and YN powders, Brian Barber, Carol Best and Keith Papworth for their expert guidance on photographic matters, and David Tricker for his help with TEM. I must also thank all the many members (past and present) of the Phase Transformations and Complex Properties Group who have helped make my course of research such an enjoyable time, and especially John Street, Mike Lord, Richard Segar, Catherine Neal and Dorothy Downs for their additional help with technical, computing and theoretical problems.

Much praise must also be heaped upon the other members of the well-schooled North Romsey Croquet Association—Cole, Connolly, Telling and Westwood (Man)—the eternally mirthful company of Alice "Julia" Clark, Colin "Rallyist" Stamper and Goggi the Cat, Pete Staves for not visiting during the writing-up process, Mrs. Melanie and Mr. Darren (Sir, Mr. Hart, Sir), Paul Chilton ('cos I said I would), Bob Pearce for "coo-wer-ell" adventures through Beerland with the Force, Ste V. Vibe of Cul for giving me all the essential advice about "them", Trish for her ever loving insistence that I "get the damn thing done", and lastly my dad for being too drunk to notice that I haven't been at home for the past $6\frac{1}{2}$ years !!!

Abstract

Welded joints of austenitic stainless steel possess coarse columnar microstructures. When subject to ultrasonic inspection, the interaction of sound waves with such highly textured grain assemblies causes the applied beam to be unpredictably skewed. Consequently, although ultrasonic testing is the desired method, it is not satisfactory for non-destructive evaluation of austenitic weldments employed in safety critical situations, *e.g.* nuclear fuel reprocessing plant.

The aim of the work presented in this thesis was to induce grain refinement in austenitic stainless steel welds, thereby producing equiaxed microstructures that would facilitate ultrasonic inspection. To achieve this an inoculant addition was sought that would provide potent nucleation sites for austenite during weld pool solidification.

Initially, a procedure based on lattice matching and solubility criteria was used to predict potentially useful inoculant compounds. This was subsequently extended on the basis of experimental results to include electrostatic, density and chemical reactivity factors.

TaN satisfied all of the procedure's requirements, and was firmly established as an effective nucleant for austenite. Grain refinement was attained as a result of TaN additions for a number of weld geometries and procedures. Ultrasonic experiments performed on a TaN inoculated multipass weld demonstrated that the refined microstructure permits improved ultrasonic transmittance, hence the prime objective of the project was achieved.

Contents

CHAPTER 5 - SINGLE-PASS WELDS : PART 1

CHAPTER 6 - SINGLE-PASS WELDS : PART 2

CHAPTER 7 - EXTENDED INOCULANT SELECTION AND ACCOMPANYING WELDS

Nomenclature and abbreviations

A	Constant in temperature dependent equilibrium solubility product
A_p	Area of plate covered by inoculant flux
A_{SL}	Solid/liquid interfacial area
A_{SM}	Solid/substrate interfacial area
A_w	Transverse cross-sectional area of weld deposit
a	Lattice parameter
a_M	Activity of M
a_{MX}	Activity of MX
a_X	Activity of X
Δa	Magnitude of the difference between two lattice parameters
B	Constant in temperature dependent equilibrium solubility product
C_0	Nominal composition of binary alloy
C_L^*	Equilibrium interfacial liquid composition
C_S^*	Equilibrium interfacial solid composition
c	Constant in Arrhenius relationship
$(Cr)_{eq}$	Chromium equivalent
d	Grain size
$d[uvw]_m$	Interatomic spacing along $[uvw]_m$
$d[uvw]_s$	Interatomic spacing along $[uvw]_s$
E_{v_p}	Statistical error in v_p
G_{het}^*	Free energy barrier to heterogeneous nucleation
G_{hom}^*	Free energy barrier to homogeneous nucleation
G_L	Thermal gradient in the liquid
ΔG_{het}	Free energy change for heterogeneous nucleation of solid
ΔG_{hom}	Free energy change for homogeneous nucleation of solid
ΔG_V	Magnitude of free energy difference per unit volume of solid and liquid
g	Gravitational constant
ΔH_f	Heat of formation of a compound
$(hkl)_m$	Low index plane of the substrate
$(hkl)_s$	Low index plane of the solid
k	Equilibrium solubility product; equilibrium partition coefficient

k_y	Constant associated with deformation propagation across grain boundaries
L	Liquid
l	Length of weld deposit
M	Substitutional metal atom
m	As a subscript refers to a substrate
m_i	Mass of inoculant flux
m_p	Mass of inoculant flux per unit area of plate covered
$\overline{m}_p$	Mean value of m_p
m_w	Mass of weld metal
N	Number density; number of measurements
N_A	Number of interceptions of inclusions per unit test area
N_L	Number of interceptions of inclusions per unit length of test line
N_V	Number of inclusions per unit volume
$(Ni)_{eq}$	Nickel equivalent
Q	Heat of dissolution of MX
R	Crystal growth rate; molar gas constant
r	Radius of a sphere
r^*	Critical radius for nucleus formation
$S(\psi)$	Shape factor
s	As a subscript refers to a nucleating solid
T	Temperature
T^*	Interfacial temperature
$T_{L(x)}$	Liquidus temperature at composition x
T_m	Equilibrium melting temperature
$T_{S(x)}$	Solidus temperature at composition x
ΔT_n	Undercooling during solidification
t_b	Base current time in arc modulation
t_p	Peak current time in arc modulation
$[uvw]_m$	Low index direction in $(hkl)_m$
$[uvw]_s$	Low index direction in $(hkl)_s$
V_S	Volume of a spherical cap
V_w	Volume of weld metal
v	Terminal velocity of a spherical particle moving through a liquid

v_p	Volume of inoculant flux per unit area of plate covered
$\overline{v}_p$	Mean value of v_p
w	Width of weld deposit
X	Interstitial atom
x_M	Concentration of M
x_{MX}	Concentration of MX
x_X	Concentration of X
Z_M	Relative atomic mass of M
Z_{MX}	Relative molecular mass of MX
Z_X	Relative atomic mass of X
α	Ferrite
δ	δ-ferrite; disregistry
ϵ	Strain
η	Coefficient of viscosity
γ	Austenite
γ_{el}	Electrostatic contribution to γ_{SM}
γ_M	Activity coefficient of M
γ_{ML}	Substrate/liquid interfacial free energy
γ_{SL}	Solid/liquid interfacial free energy
γ_{SM}	Solid/substrate interfacial free energy
γ_{st}	Structural contribution to γ_{SM}
γ_X	Activity coefficient of X
Φ	Angle between incident ultrasonic beam and receiver probe
ψ	Wetting angle
$\rho_{298\mathrm{K}}$	Room temperature density
ρ_p	Particle density
ρ_s	Steel density
σ_i	Friction stress opposing dislocation glide
σ_{v_p}	Standard deviation in v_p
σ_y	Lower yield stress
Θ	Incident angle between columnar grain axis and applied ultrasonic beam
θ	Angle between $[uvw]_m$ and $[uvw]_s$
AISI	American Iron and Steel Institute

A-TIG	TIG welding with activating flux
bcc	Body centred cubic
BNFL	British Nuclear Fuels Ltd.
CET	Columnar-to-equiaxed transition
CSR	Consumable socket ring
d.c.	Direct current
EDX	Energy dispersive X-ray analysis
EMS	Electromagnetic stirring
fcc	Face centred cubic
HAZ	Heat affected zone
ICPS	Inductively coupled plasma spectroscopy
MTDATA	Metallurgical and Thermochemical Databank
NAG	Nitric acid grade
PISC	Programme for the Inspection of Steel Components
SEM	Scanning electron microscopy
TEM	Transmission electron microscopy
TIG	Tungsten-inert-gas

Chapter 1 - Introduction

1.1 - Overview

Nuclear power stations use the heat produced by controlled nuclear fission to generate electricity. Numerous types of fuel element are used in reactors, but all contain some form of enriched uranium ore sealed within metallic cans made from either magnesium alloys, zirconium alloys or stainless steels. Whilst in service, waste products from the various fission reactions build up within the fuel rods lowering their efficiency. Waste products also increase the net volume of the fuel, hence can cause the cladding to swell and rupture. Consequently the average life-span of a nuclear fuel rod is about four years.

However, after this time the fuel element still contains 97% reusable nuclear material (96% uranium and 1% plutonium) which can be recovered by reprocessing. There are two reasons why such recycling is advantageous (Addinall, 1982). Firstly, on a like for like basis, reprocessing reduces the total volume of nuclear waste by 25% when compared with the direct disposal of spent fuel after a single cycle and its replacement with fresh material. Secondly, although the world's remaining uranium resources are considerably greater than for any other non-renewable energy source based on current and projected usage, the supply is still estimated to last only 175 years. This can be significantly prolonged if all nuclear fuel is reprocessed.

Nuclear fuel reprocessing in the U.K. has been carried out since 1964 at British Nuclear Fuels Ltd.'s (BNFL) Sellafield plant. The reprocessing facility of BNFL's operation is now a world leader, with current secured orders worth over £12 billion, half of the business coming from overseas customers.

The recycling of nuclear fuel is thus now a well established industrial process (Addinall, 1982). Spent fuel rods are first stored under water to allow them to cool. After a number of months they are transferred to the reprocessing plant, where computer-controlled machines strip off the metal casings, and chop the fuel inside into small pieces. The fuel is then dissolved in concentrated nitric acid, and solvent processes are used to extract waste products. The remaining uranium and plutonium are then separated. The recovered material is sent to fuel manufacturing plants for use in new rods.

The nitric acid used in the process is highly concentrated, typically over 60%, and hence the materials used for pipework, condensers, reaction vessels and so on, must have extremely good corrosion resistance. The predominant material currently employed for these purposes is austenitic stainless steel (Chapter 2), and special grades have been developed over the past 40 years to meet the increasingly exacting standards demanded by safety regulations.

However, welded joints of austenitic stainless steels have presented a problem. Whilst the steel is easily weldable and completed joints have satisfactory corrosion resistance and mechanical properties, ultrasonic inspection of these welds is extremely difficult, particularly to the levels required by such a safety critical application (Whiting *et al.* 1978).

Austenitic stainless steel welds develop extensive coarse, columnar grain structures during their fabrication. When subject to ultrasonic inspection, the microstructure causes unpredictable skewing of the applied sound beam, making it virtually impossible to determine the size and position of any defects present. Consequently, welds can only be tested by the less favourable means of radiography. Safety margins are thus reduced and strict, time consuming welding procedures have to be followed to ensure as few defects as possible.

Therefore, the aim of this project was to investigate methods of grain refining austenitic stainless steel welds to produce microstructures that facilitate ultrasonic inspection. The origin of the problem is considered in detail by reviewing fusion welding processes, weld pool solidification and hence microstructural development, and the effects of microstructure on ultrasonic wave propagation.

1.2 - Review of fusion welding processes

1.2.1 - Introduction to fusion welding

The advent of reliable fusion welding processes in the 1930s has made them the most common method of joining metals in large scale industrial applications such as ship building, chemical and petroleum plant and structural frameworks (Lancaster, 1987). Fusion welding involves the application of a heat source sufficient to melt the edges of two components to be joined whilst further molten material is added in between to fill any gap. When the joint is completed, the components are so well bonded that they can be regarded as a single structural unit.

The fusion welds of concern to this study are formed by arc welding (Svensson, 1994). Although there are numerous arc welding systems, their general configuration remains the same. A power source generates an arc between an electrode and the workpiece, creating a plasma of ionized atoms and free electrons. The heat from the arc, which has a core temperature

in excess of 10,000 °C, is carried by the plasma to the workpiece causing parts of it to melt. The electrode is heated by resistance heating from the current passing through it, and by the arc. If the electrode is a consumable, then it is melted itself to provide the filler material. If non-consumable electrodes are used, the heat produced melts an extra rod of filler material placed close to the tip of the electrode (*n.b.* in the absence of filler material, non-consumable electrodes simply melt the workpiece and produce autogenous welds). In both cases drops of molten material are transported to the workpiece by forces in the plasma. The mixing of molten material from the workpiece and molten drops of filler material creates a weld pool, which when solidified forms the join between the two components.

All arc welding processes use a shielding system to protect the molten weld metal from the air. This shielding is usually provided by one of two methods. The electrode may be coated with minerals which melt and cover the solidifying weld metal with a protective layer of slag. Alternatively, an inert gas may be used to shield the surface of the weld pool.

The structure of an arc weld is shown in Fig. 1.1. The two components to be joined constitute the base material, and these are bonded together by the weld metal. The heat from the fusion process is sufficient to cause transformations in a region of base material adjacent to the weld metal, commonly known as the heat affected zone (HAZ). These transformations are frequently of great importance to the metallurgical, mechanical and corrosion properties of the joint.

1.2.2 - Welding in the nuclear fuel reprocessing industry

By far the most practised welding method in the construction of reprocessing plant is the tungsten-inert-gas (TIG) process. All of the welds in this study have been made using this method. TIG electrodes are non-consumable, and are made from tungsten or thoriated-tungsten alloys because of their extremely high melting points. Even so the electrode tip is still usually cooled to ensure it remains solid. Filler material is supplied by a rod or wire which melts as it is fed close to the electrode tip. The weld pool is shielded by an inert gas, typically argon or helium, piped in around the electrode. The TIG welding method is versatile and can be applied either manually or mechanically. A schematic diagram of the arc area and components of the TIG process is shown in Fig. 1.2.

The TIG process usually generates very clean welds with high standards of weld metal quality, hence is well suited to the welding of components in safety critical applications such as the reprocessing industry. However, there have in the past been complications with welding pipework. Pipes are butt-welded end-to-end using a mechanical TIG unit which orbits the

Fig. 1.1 - Structure of an arc welded joint (Svensson, 1994).

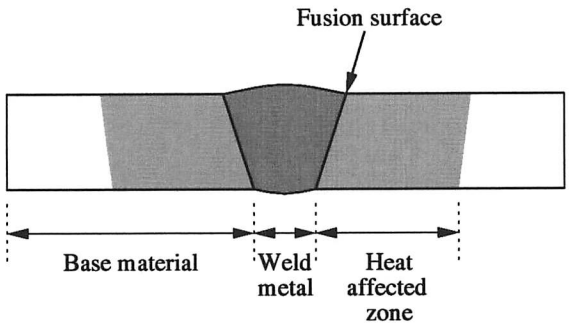

Fig. 1.2 - The TIG welding process (Svensson, 1994).

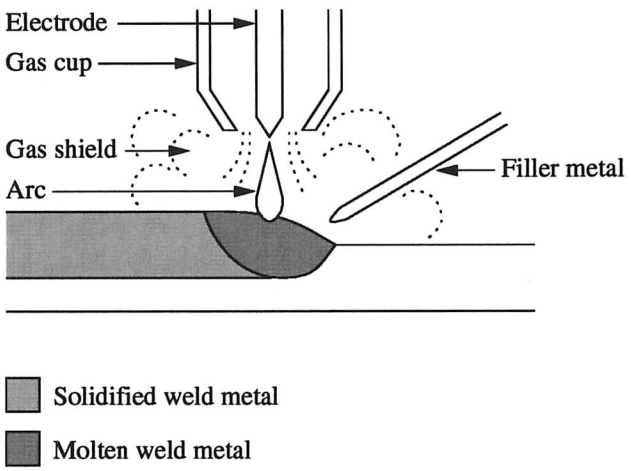

Fig. 1.3 - The consumable socket ring (CSR) (Carrick *et al.* 1985).

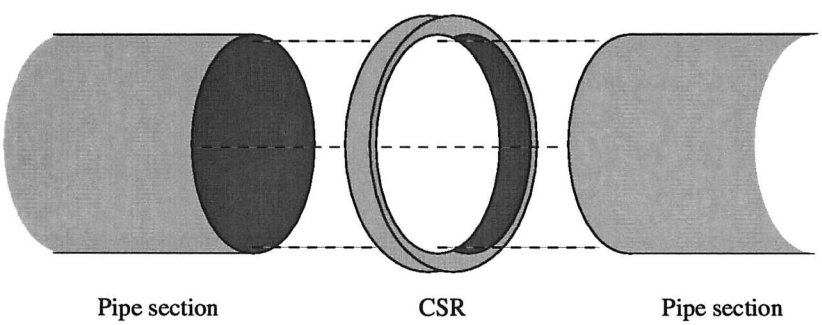

circumference of the joint. The supply of filler material evenly around the joint is often difficult, leading to problems such as variable weld penetration, misalignment and distortion from necessitated multiple weld passes.

In the mid-1980s, BNFL developed a new method of providing filler material for circumferential welds to replace the traditional rods and wires (Carrick *et al.* 1985; Mothersill, 1993). The consumable socket ring is an accurately machined insert which has the dual function of aligning the pipes and providing a measured amount of filler material which can be fused in a single pass (Fig. 1.3). The weld preparation time is thus reduced as the pipe ends can simply be square cut and are instantly aligned by the ring. Uniform deposition of filler material leads to fewer weld defects and better surface finish. The joints do not therefore require "dressing" before inspection and testing. Consumable socket rings permit the rapid production of consistently high quality TIG welds.

1.3 - Weld pool solidification

1.3.1 - Initial solidification of the weld metal

In all fusion welding processes initial solidification of the weld metal occurs by the same mechanism (Easterling, 1992). During welding the heat supplied melts back a part of the base material causing it to mix with some of the molten filler material. This *dilution* is important as it ensures that the base material in contact with the liquid weld metal is clean and free of oxide films. It also means that solidification of the weld pool initiates from grains in the base material along the *fusion surface*, which is the boundary between melted and unmelted metal. There is no nucleation barrier to solidification, thus crystals of weld metal simply grow with an orientation determined by the grains in the base material, *i.e. epitaxially.*

1.3.2 - Competitive growth mechanisms

Whilst epitaxial growth leads to the crystals of weld metal solidifying as an extension of the base material, most of these initial grains do not grow very far. This is because of a competitive growth mechanism.

Crystal growth tends to occur along certain preferred crystallographic directions (Easterling, 1992). In the case of body-centred cubic (bcc) and face-centred cubic (fcc) metals, growth is most rapid along the <100> direction. This is thought to be because the <100> direction in these materials is the least close-packed, hence offers the easiest way for the random atomic arrangement of the liquid to align during crystallization. Unfavourably oriented grains thus

grow slowly and their development is quickly stifled as the solidifying interface moves forward (Fig. 1.4).

An additional constraint is provided by growth being favoured parallel to the maximum thermal gradients. Because of the geometry of a typical weld pool, the direction of the maximum thermal gradient varies as a function of position along the fusion line (Baikie *et al.* 1976). The effect of this is to further restrict grain growth, and the predominant orientation which results consists of grains possessing a <100> direction perpendicular to the average fusion line (Fig. 1.5).

1.3.3 - Generation of multipass weld microstructure

The growth mechanisms which have been discussed lead to a columnar grain structure evolving within a single deposited weld pass. Where completion of a joint requires several such passes, each subsequent run partially remelts the underlying deposit. Epitaxial solidification again ensues, with new columnar grains adopting an orientation identical to those within the previous columnar zone. Consequently, the microstructure of multipass welds consists of continuous coarse columnar grains, sometimes several centimetres in length (Fig. 1.6). It is the interaction between sound waves and such microstructures that impedes ultrasonic inspection.

1.4 - Ultrasonic inspection of austenitic stainless steel welds

1.4.1 - Introduction to ultrasonic inspection

Internal flaw detection is almost exclusively carried out by radiography and ultrasonic inspection. Other non-destructive evaluation methods, for example magnetic particle and liquid dye penetrant tests, are useful only for the identification of surface defects.

In radiography X-rays or γ-rays are passed through components onto radiation sensitive film (Fig. 1.7). On encountering a flaw, radiation is affected differently from that passing through the defect-free bulk material. The film is thus exposed to a different level of radiation and once developed displays an image of the fault.

However, there are significant drawbacks inherent to the technique (Mix, 1987). The shadow formation principles that apply to visible light transmission are also applicable to X-ray and γ-ray transmission; hence images are not sharp. Geometric distortions occur as some parts of the object are always further away from the film than others. This effect is heightened if the plane of the film is not parallel to that of the sample, which is often the case for complex components. A single radiograph gives no information about a defects size and position normal

Fig. 1.4 - Diagram of region close to weld fusion surface (David and Vitek, 1993).

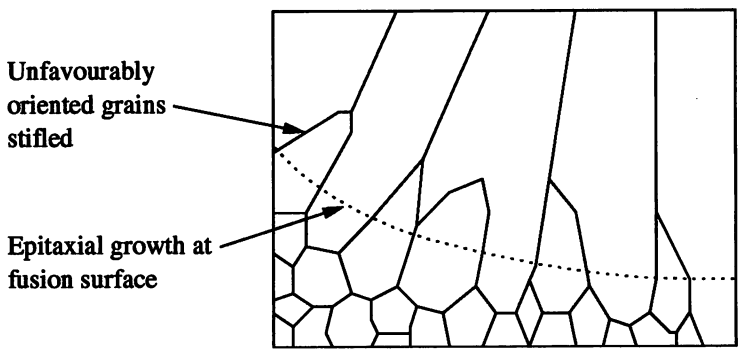

Fig. 1.5 - Diagram of single-pass weld. Favourably oriented grains grow along maximum thermal gradients (Baikie *et al.* 1976).

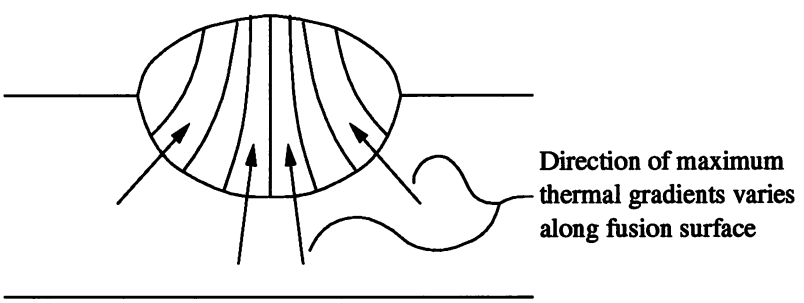

Fig. 1.6 - (a) Schematic diagram of a multipass weld showing columnar grains growing continuously between successive passes. (b) Micrograph of an austenitic stainless steel multipass weld.

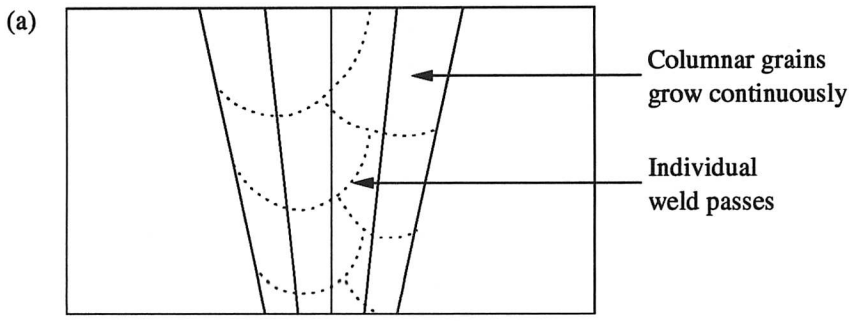

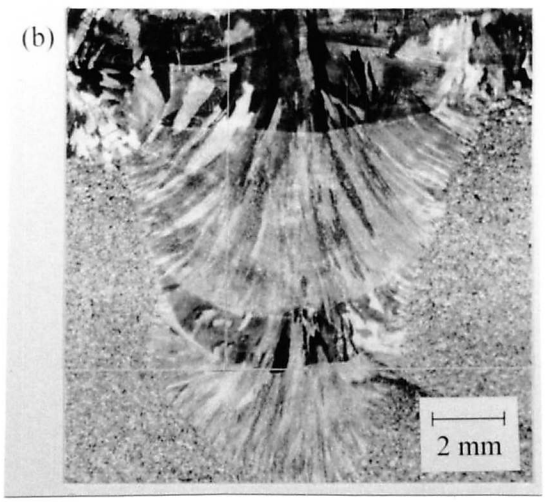

Fig. 1.7 - X-ray radiography of a component (Mix, 1987).

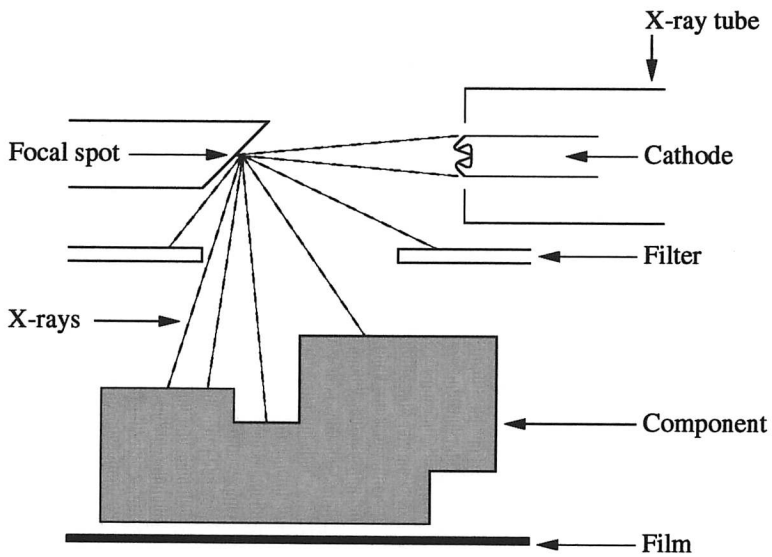

to the film. Several radiographs are often required to properly "triangulate" the size, shape and location of the flaw.

Ultrasonic inspection eliminates these problems and is thus generally preferred to radiography when accurate investigation is required (Halmshaw, 1987). A high frequency sound beam (typically 1–10 MHz) is passed through the component under examination. Defects in the path of the beam reflect back some of the sound. The location of each flaw can then be determined by measuring the time of travel of the ultrasonic beam to and from the defect, and the size and shape assessed by observing the amplitude of the reflected beam as the transducer is moved.

Ultrasonic testing also has another application, of particular importance to the nuclear reprocessing industry, which cannot be achieved by radiography. The concentrated nitric acid used in the separation process causes uniform corrosion of the pipework which contains it. It is therefore desirable to monitor the effect by regularly measuring the wall thickness of vessels. The echo from the backwall of components during ultrasonic inspection facilitates such examination.

1.4.2 - Effect of austenitic weld structure on ultrasonic propagation

When subject to ultrasonic inspection all materials cause some interference with the sound beam (Krautkramer and Krautkramer, 1969). For example, grain boundaries in the material can act as acoustic discontinuities scattering the beam. The amplitude of signals from defects is thus reduced by this *attenuation*, and the sound reflected by the grain boundaries appears on the oscilloscope screen as *grass*, lowering the signal-to-noise ratio. Because of this the resolution of defect detection is limited.

In most metals, including fine grained austenitic stainless steel plate and pipe, the extent of attenuation and grass is sufficiently low to present few problems; clear signals are usually received from *e.g.* backwall and defect echoes (Fig. 1.8a). The coarse columnar microstructure of austenitic stainless steel welds, however, induces considerable, unpredictable scatter of the ultrasonic beam. The intensity of received signals is greatly reduced with the consequence that important peaks become indistinguishable from grass (Fig. 1.8b). Satisfactory inspection is thus difficult to achieve.

In materials composed of large grains, the negligible random scatter of sound waves is replaced by geometrical division, which can cause a total loss of reflected sound (Krautkramer and Krautkramer, 1969). This effect occurs once the grain size becomes greater than a tenth of the sound beam wavelength. In steel the velocity of sound is about $6000\,\mathrm{m\,s^{-1}}$, so with a

Fig. 1.8 - Comparative ultrasonic traces from (a) equiaxed austenitic plate and (b) columnar austenitic weld metal.

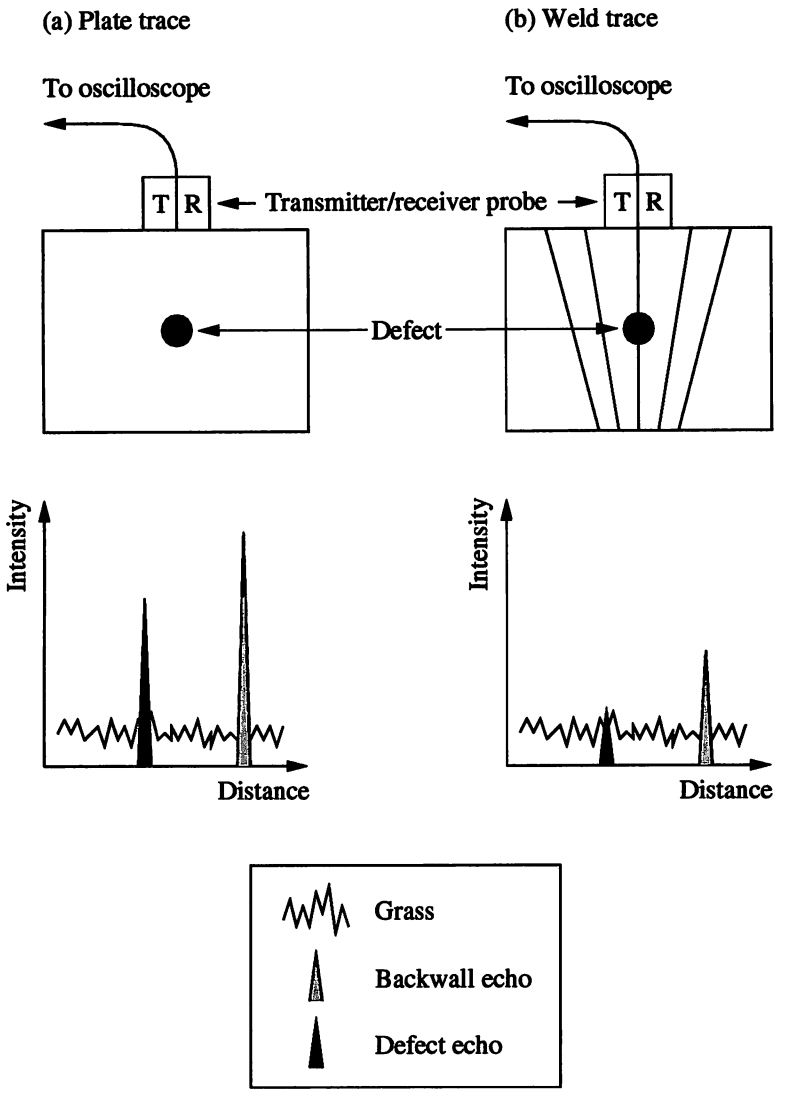

typical frequency of 6 MHz, the wavelength is 1 mm. The grains in austenitic stainless steel welds can be considered as hexagonal prisms, with diameters often in excess of 100 μm and lengths of several millimetres, thus are clearly of a size to generate problems in ultrasonic propagation.

Work has also been performed to describe another phenomenon that occurs when sound waves interact with a coarse columnar microstructure (Baikie *et al.* 1975; Baikie *et al.* 1976; Tomlinson *et al.* 1980). A cylinder of austenitic stainless steel weld metal, machined with the columnar grains aligned along a diameter, was mounted with its axis vertical, and ultrasonic transmitter and receiver probes were positioned so that a sound beam could be passed horizontally through the cylinder. Both the cylinder itself and the receiver probe could be rotated about the axis of the cylinder (Fig. 1.9).

With the probes in line and the cylinder being rotated, the transmitted signal was found to vary as a function of the incident angle Θ between the columnar grain axis and the ultrasonic beam (Fig. 1.10a). Similar experiments were performed by traversing the receiver probe around the cylinder whilst the incident angle Θ remained fixed. For several values of Θ, the maximum transmitted signal was not recorded when the transmitter and receiver probes were in line, indicating that the sound beam was skewed off the intended path (Fig. 1.10b).

Negligible skewing effects and variations in signal with orientation were observed with cylinders of equiaxed austenitic stainless steel plate demonstrating that these phenomena are not related to the composition of the alloy.

With a single crystal of a fcc nickel alloy, machined with a <100> direction along the cylinder axis, almost identical results to those from the austenitic weld metal were recorded (Fig. 1.10c).

These observations can be explained because the highly textured assembly of columnar grains in the weld metal can be considered as a homogeneous anisotropic medium akin to the nickel alloy single crystal. An important feature of the propagation of waves in anisotropic materials is that, in general, the beam direction—the direction of energy travel—is not perpendicular to the wave front. This arises because the variation in elastic constants with direction in an anisotropic material affects components of the beam velocity differently with respect to an arbitrary initial direction of travel (Musgrave, 1954). Consequently an ultrasonic beam passing through such a material will be skewed off the straight through direction.

Fig. 1.9 - Experimental arrangement to study the effect of weld microstructure on ultrasonic propagation (Baikie *et al.* 1975).

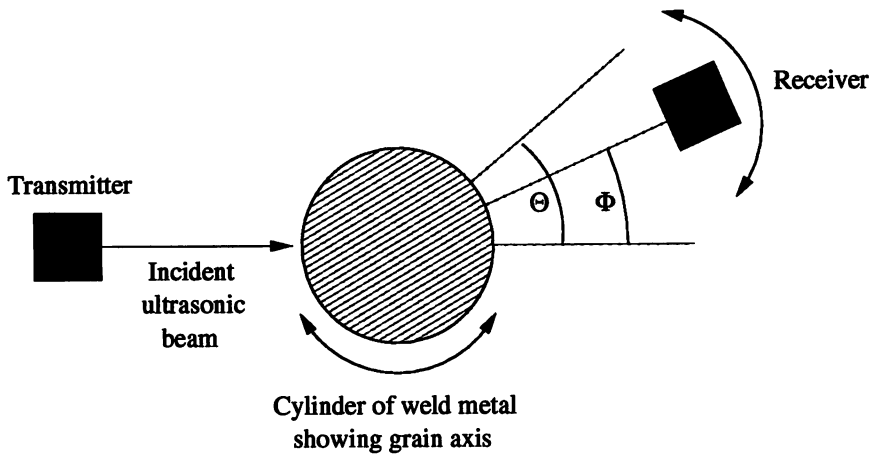

Fig. 1.10 - Intensity of transmitted signal as a function of (a) the incident angle Θ between the columnar grain axis and the ultrasonic beam for austenitic weld metal, (b) the angle Φ between the ultrasonic beam and the receiver probe for austenitic weld metal and (c) the angle Θ as the nickel alloy single crystal is rotated (Tomlinson *et al.* 1980).

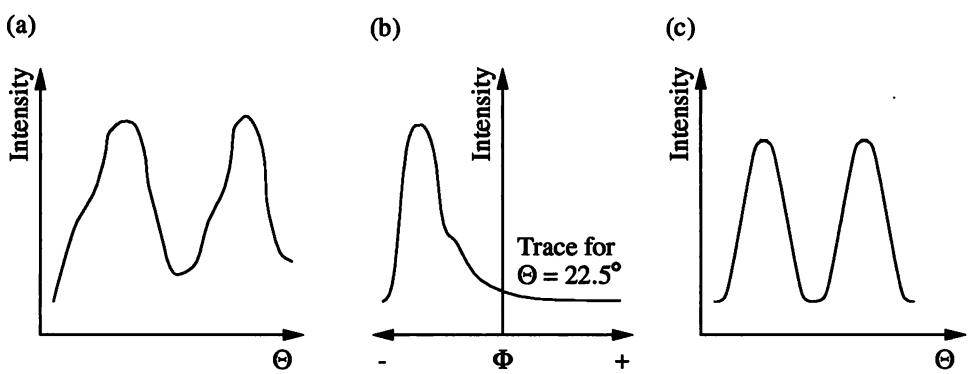

1.4.3 - Ultrasonic inspection procedures for austenitic stainless steel welds

The skew angle varies as a function of the angle Θ between the <100> columnar grain axis and the incident ultrasonic beam so that theoretically, for an inspection in which the orientation of the columnar grains is known, the receiver probe can be positioned to pick up the maximum transmitted signal and thus give useful information about any defects present.

The orientation of the columnar grain assembly differs for every welding procedure, and for complex industrial procedures, is virtually impossible to predict. Therefore ultrasonic inspection routines for austenitic stainless steel welds have to be devised for specific welding geometries, each of which requires extensive, time consuming laboratory investigation.

However, laboratory successes are not mirrored when applied to real industrial situations. Procedures are developed using defects of known size and position, whereas inspectors on-site have no knowledge of the internal state of components to be examined. The procedures also assume a certain level of proficiency on the inspectors part, which may be outside the scope of existing qualification schemes. A recent survey found no national training or certification available for personnel testing austenitic weldments (Edwards, 1996), and the Programme for the Inspection of Steel Components (PISC) highlighted the variation in inspector competence (Lemaitre *et al.* 1994). PISC conducted round-robin trials involving over 20 teams from different countries, each asked to perform ultrasonic inspection of austenitic stainless steel welds using a given procedure. The reports produced by each team differed dramatically.

Physical problems can also arise when applying laboratory techniques to in-service welds. Inspection routines for specific weld geometries are often coupled with changes to the welding procedure itself, which sometimes cannot be accommodated during the final installation of components. It is also possible for the columnar grain orientation to vary from the laboratory determined value because of cast-to-cast variations and differing heat flow conditions during final installation affecting weld pool solidification.

All of these shortcomings mean that the reliability of test procedures is highly questionable when they are employed in industrial environments, a point succinctly made by Silk (1987) whilst reviewing ultrasonic techniques and routines for austenitic welds; "Each can work spectacularly well on some specimens, but may then fail on others."

1.5 - Summary

Safety regulations demand rigourous inspection of components throughout nuclear fuel reprocessing plant, the majority of which—pipework, condensers, reaction vessels *etc.*—are constructed from austenitic stainless steel. The preferred method for non-destructive evaluation of such material is ultrasonic inspection.

Welded joints of austenitic stainless steel possess coarse columnar microstructures, which arise because of epitaxial grain growth. The interaction between sound waves and such a highly textured grain assembly leads to an applied ultrasonic beam being unpredictably skewed off its intended path. Consequently it is extremely difficult to satisfactorily inspect austenitic stainless steel welds using ultrasonics, and although testing procedures have been devised for numerous specific weld geometries, it is generally held that their industrial application is not practicable. Austenitic weldments thus have to be tested by the less favourable means of radiography, hence safety margins are reduced and strict, time consuming welding procedures are required to ensure minimal defect levels.

In collaboration with BNFL, the current project was thus established to investigate methods of grain refining austenitic stainless steel welds to produce equiaxed microstructures that facilitate ultrasonic inspection.

Chapter 2 - Austenitic stainless steels

2.1 - Introduction

The aim of the present study was to refine the grain structure of austenitic weldments as a means of improving ultrasonic wave propagation through such material. Thus to select a suitable approach to the problem, the behaviour of austenitic stainless steels, particularly in the context of welding, must be well understood.

Pure iron under equilibrium conditions undergoes a phase transformation from ferrite (α) to austenite (γ) at 910 °C. Additions of other elements when steel-making though, can strongly affect the formation of either phase. For example, chromium additions alone favour the formation of ferrite, whereas nickel promotes austenite stability (Honeycombe and Bhadeshia, 1995).

Chromium additions of appreciable quantity greatly improve the corrosion resistance of steels, giving rise to the term "stainless" (Section 2.2.1). The high levels of chromium cause these materials to be wholly ferritic at room temperature. However, if such steels are also alloyed with sufficient nickel, then austenite can be retained at room temperature and below, leading to the class of austenitic stainless steels (Pickering, 1976; Rivlin and Raynor, 1980; Marshall, 1984). If the stability of the austenite is inadequate then martensite may form. A stable austenitic steel is thus defined as one in which the martensite-start temperature, M_s, is lower than room temperature. A phase diagram for Fe-Cr-Ni alloys is shown in Fig. 2.1. Many other common alloying elements are also important in determining austenite/ferrite stability, hence the phase equilibria of austenitic steels is usually more complex (Section 2.3).

Austenitic stainless steels are readily available, easy to fabricate and weld, and exhibit several properties which make them ideal for use in nuclear fuel reprocessing plant (Roberts, 1994). They are corrosion resistant both at room and elevated temperatures even in powerful oxidising media such as nitric acid, do not undergo a ductile-to-brittle transition which causes so many problems in ferritic steels and have excellent impact resistance even at low temperatures.

Many of these properties, most notably corrosion resistance, need to be optimised for the steels to be of use in the nuclear reprocessing industry because of the stringent safety requirements which must be satisfied. For example, the maximum permitted uniform corrosion rate for pipework containing nitric acid is $0.3\,\mathrm{mm\,year^{-1}}$ (Gladman, 1988). This can be achieved by careful control of the alloying elements present in the steels.

Fig. 2.1 - Vertical section of phase diagram for very low carbon Fe-Cr-Ni alloys at 18 wt% chromium (Castro and de Cadenet, 1974).

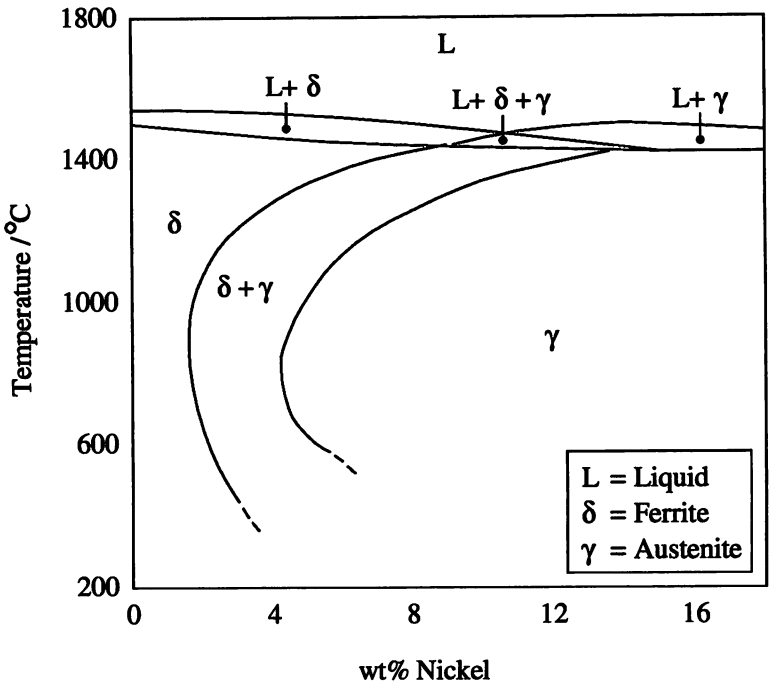

A collaboration between BNFL and the steel companies led to the development of a nitric acid grade (NAG) austenitic stainless steel specifically for use in the reprocessing facilities at Sellafield. The following two sections discuss the effect of various alloying additions on corrosion resistance and weldability, which governs their composition limits within the NAG steel used throughout the present study.

2.2 - NAG austenitic stainless steel

2.2.1 - Effect of alloying additions on corrosion resistance

The corrosion resistance of austenitic stainless steels is primarily due to their high chromium content (Dillon, 1960; Shreir *et al.* 1994). If a steel contains above ~12 wt% Cr in solid solution, then a thin, adherent, continuous oxide film will form on its surface. The exact composition of such oxide films is difficult to determine, but they all contain chromium in (III), (IV) and (VI) oxidation states in varying proportions. Paradoxically, the oxide film itself is formed by rapid corrosion of the steel surface. However, once established it dramatically stifles the rate of further oxidation by acting as a barrier between the metal and the corrosive environment. The steel is thus said to be in a state of *passivity*.

In this respect the carbon content of the steel is critical (Cowan and Tedmon, 1973). Carbon binds chromium in the form of Cr-rich grain boundary carbides, usually $Cr_{23}C_6$. During the precipitation of such carbides, which contain 70–80 wt% Cr, the austenite matrix adjacent to the grain boundaries is depleted of chromium. Moreover, the chromium level in these regions drops below the necessary ~12 wt% required to maintain passivity. Consequently the steel undergoes localised intergranular corrosion (Fig. 2.2). The problem is minimised in NAG steel as it has an extremely low carbon content—typically 0.01 wt% maximum, well below that of other austenitic grades—which prevents all carbide precipitation (Berglund, 1981).

Dissolved nitrogen is widely believed to have a beneficial impact on the general corrosion resistance of austenitic stainless steels, although the mechanism by which it contributes is unclear (Stein and Menzel, 1995; Murata and Sakamoto, 1997). However, increased nitrogen concentrations facilitate precipitation of the Cr-rich nitrides Cr_2N and π-phase (typically $Cr_{12.8}Ni_4Fe_{3.2}N_4$). In accordance with the chromium depletion theory presented above, intergranular corrosion resistance is thus reduced. The nitrogen content of NAG steel is kept below 0.02 wt% to prevent nitride precipitation.

Fig.2.2 - (a) Intergranular precipitation of $Cr_{23}C_6$ particles leading to chromium-depleted zones adjacent to grain boundaries, (b) variation in chromium content across a grain boundary and (c) resultant intergranular corrosion.

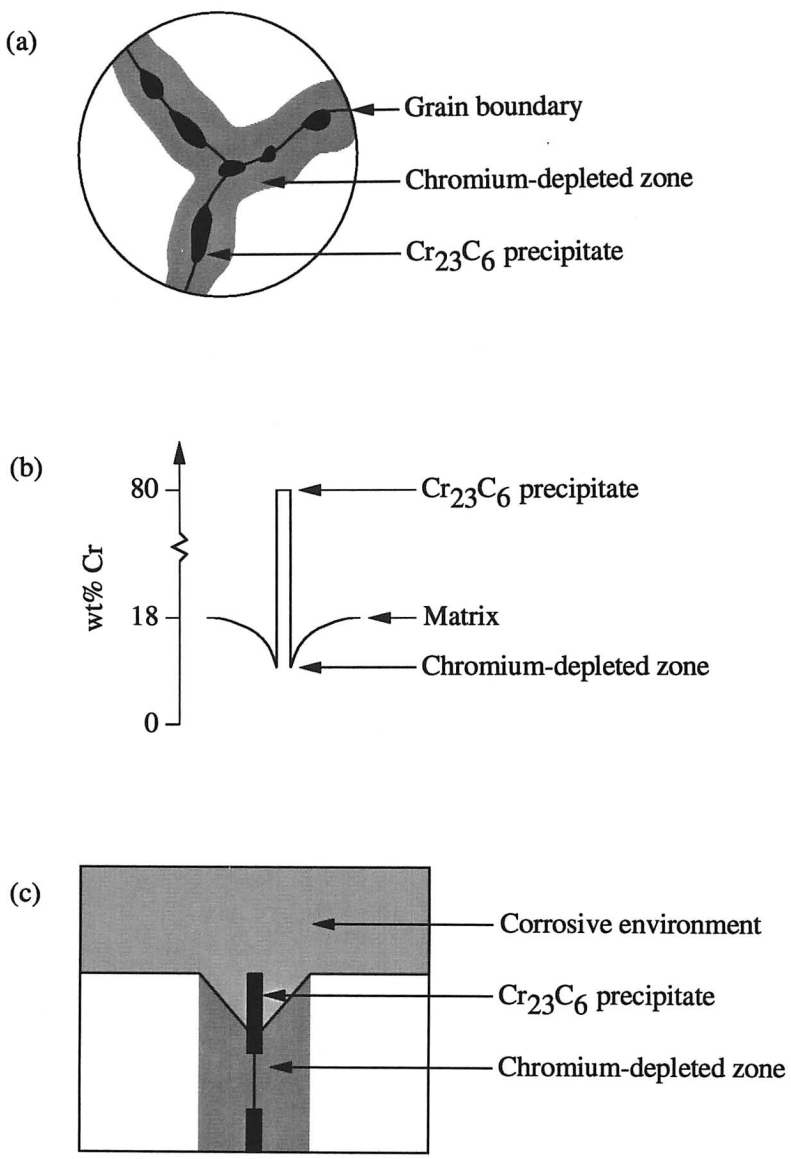

Boron is often added to commercial austenitic grades to enhance hot workability. However, such levels of boron can result in intergranular precipitation of Cr_2B which has a detrimental effect on corrosion resistance via localised chromium depletion. Excessive boron can also contribute to solidification cracking during welding. Because of these factors, deliberate boron additions are precluded from NAG steel (Gladman, 1988).

Minor alloying additions such as silicon, sulphur and phosphorus tend to segregate to grain boundaries, thereby altering their composition and destabilising the protective oxide film over such regions (Blom and Kvarnback, 1975). Intergranular corrosion is thus encouraged. Therefore, these elements are present in NAG steel in minimal quantities. However, if the sulphur content is reduced by too much the weldability of the steel can be impaired (Section 2.2.2).

Titanium and niobium are added to steels as *stabilisers* and can have contradictive effects on corrosion resistance. The carbides of these elements—TiC and NbC—are more stable than $Cr_{23}C_6$ and so form preferentially. Localised chromium depletion is thus prevented and intergranular corrosion resistance is improved (Gladman, 1988). On the other hand, in titanium stabilised steels, the inevitable increase in dissolved titanium renders the steel more vulnerable to general corrosion. Problems also arise in niobium stabilised steels. In rolled sections, the deformation causes grains to elongate parallel to the rolling direction. Surfaces perpendicular to the rolling direction thus display *end-grain* (Fig. 2.3a). NbC tends to arrange in *stringers* also parallel to the rolling direction. Impurity elements segregate to the boundaries between NbC and the steel matrix, reducing corrosion resistance in these regions. Where end-grain is exposed, the distribution of NbC thus provides paths for heavy corrosive attack into the steel (Fig. 2.3b) (Quayle, 1997). In the past this effect was wrongly attributed to the dissolution of NbC itself because of its absence in corroded samples (Berglund, 1981). However, the carbides simply fall out once the surrounding steel matrix has been dissolved.

Molybdenum has a small negative effect on intergranular corrosion resistance. This is thought to arise from reduced homogeneity of the steel through increased microsegregation (Berglund, 1981). However, the pitting resistance of steels can be greatly improved by molybdenum additions. Pitting occurs in environments which contain particularly aggressive species such as chloride ions, which substitute into the protective oxide film coating the steel causing localised breakdown of passivity and the formation of pits (Champion, 1964). Pitting is especially insidious as the propagation of corrosive attack is predominantly into the metal, which in thin vessels can easily result in perforation and subsequent fluid leakage. In steels, molybdenum additions become incorporated into the protective oxide film giving it improved

Fig. 2.3 - (a) Schematic diagram of end-grain occurring in rolled steel and (b) distribution of NbC resulting in heavy corrosive attack.

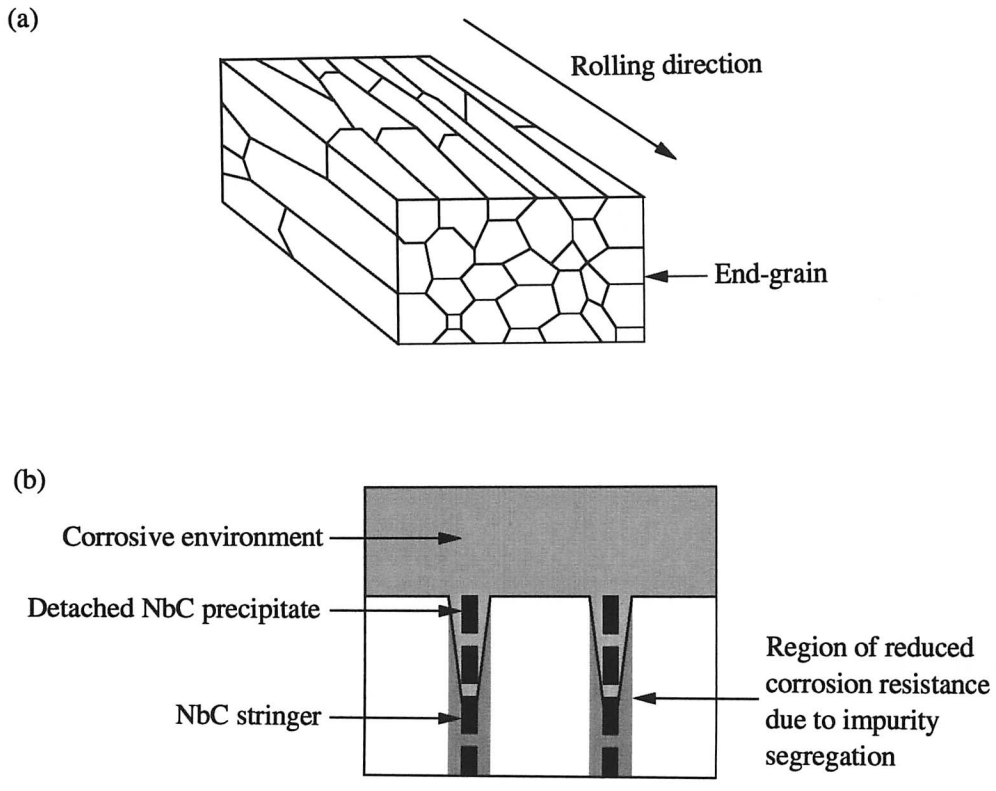

stability, although the reasons why such changes in film composition should improve resistance to breakdown remain speculative (Mitrovic-Scepanovic *et al.* 1987; Landolt *et al.* 1990; Mischler *et al.* 1991).

2.2.2 - Effect of alloying additions on weldability

The levels of certain alloying additions can present problems in the weldability of austenitic stainless steels. Other elements produce damaging effects in the parent material during welding because of reactions which occur due to elevated temperatures in the HAZ. Three of the most significant effects are described here.

i) δ-ferrite content

Fully austenitic stainless steel weldments are susceptible to hot-cracking during solidification. Severe cracks occur at grain boundaries, particularly along the weld centreline (Crook and Shaw, 1979). However, hot-cracking can be minimised if the steel contains a small amount of δ-ferrite.

The prime cause of hot-cracking is the segregation of sulphur and phosphorus during solidification (Castro and de Cadenet, 1974). These elements form low melting point interdendritic liquid films which result in a lack of cohesion between grains at the same time as shrinkage stresses become felt during cooling of the solidified weld metal.

The presence of δ-ferrite alleviates the problem in three ways (Porter and Easterling, 1992). The fine duplex $\delta + \gamma$ structure increases the total grain boundary area, thus the severity of sulphur and phosphorus segregation is lessened. Phosphorus also dissolves in δ-ferrite, reducing its impact. If solidification is entirely to austenite, all manganese present remains in solution. The existence of δ-ferrite, however, allows manganese to combine with sulphur to form discrete MnS inclusions. MnS is desirable as it does not extensively wet dendrite boundaries, unlike FeS which would otherwise form.

The δ-ferrite content can be manipulated by adjusting the alloy composition. For welding, the effect of this on the resultant phase formation can be conveniently represented by the Schaeffler diagram (Fig. 2.4) (Castro and de Cadenet, 1974). The room temperature phase boundaries of austenite, δ-ferrite and martensite are plotted in terms of the chromium and nickel equivalents. The chromium equivalent has been empirically determined to take into account the effect of the common ferrite forming elements. Similarly, the nickel equivalent does the same for the austenite formers. The ratio between the two thus describes the proportions of each phase present in an alloy.

Fig. 2.4 - The Schaeffler diagram (Castro and de Cadenet, 1974).

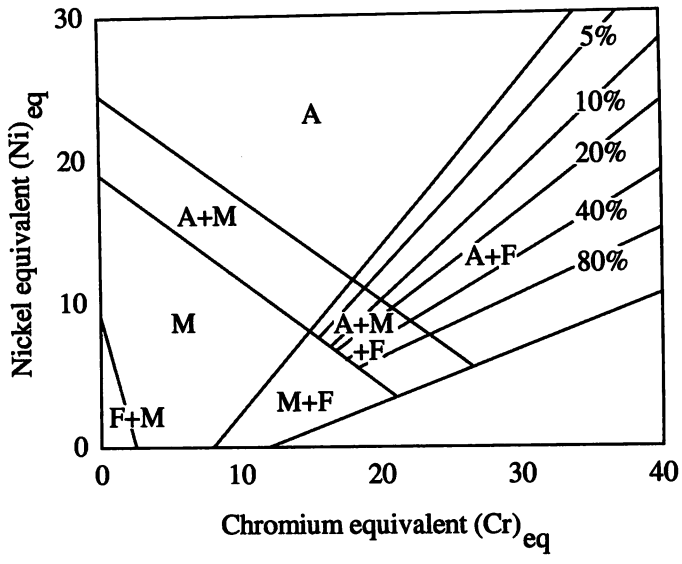

$(Cr)_{eq}$ = %Ni + (30 x %C) + (0.5 x %Mn) (in wt%)

$(Ni)_{eq}$ = %Cr + %Mo + (1.5 x %Si) + %Nb (in wt%)

A = Austenite
F = Ferrite
M = Martensite

Fig. 2.5 - Temperature-time growth curves for $Cr_{23}C_6$ and TiC/NbC in austenitic steels (Honeycombe and Bhadeshia, 1995).

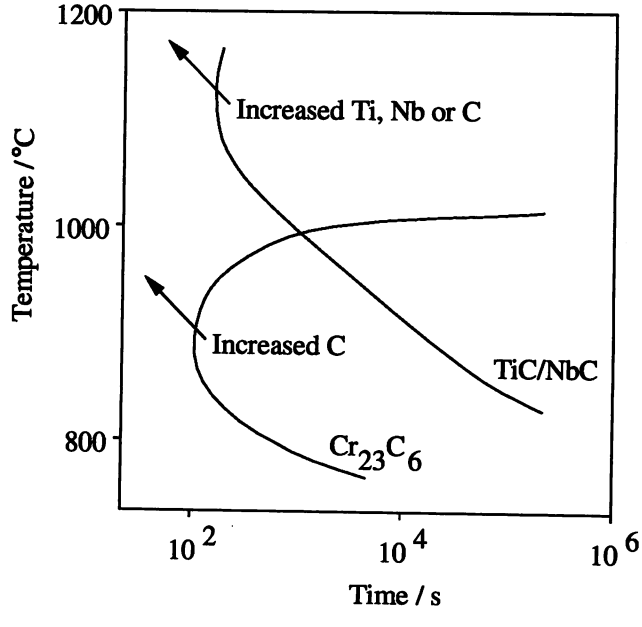

Unfortunately, δ-ferrite has a detrimental effect on the corrosion resistance of austenitic stainless steels, and in NAG weld metal the volume fraction is typically less than 0.05.

ii) Weld decay and knife-line attack

Weld decay is a phenomenon whereby a region of the HAZ is subjected to increased intergranular corrosion (Crook and Shaw, 1979; Shreir *et al.* 1994). Between 550 and 850 °C the nucleation and growth of $Cr_{23}C_6$ is favoured (Fig. 2.5). Any process which allows the steel to pass slowly through this temperature range will thus lead to $Cr_{23}C_6$ formation with subsequent grain boundary chromium depletion and increased susceptibility to intergranular corrosion. During welding, a band of material in the HAZ parallel to the deposit is held within the critical temperature range, hence is subject to this problem (Fig. 2.6). Closer to the fusion surface the critical temperature range is exceeded, whilst further away the temperature does not reach the lower limit.

Knife-line attack is a closely related phenomenon which occurs in titanium and niobium stabilised steels (Crook and Shaw, 1979; Shreir *et al.* 1994). During welding, the parent material immediately adjacent to the fusion surface is heated to just below the melting point. All $Cr_{23}C_6$ and TiC/NbC present dissolves completely, and on cooling neither precipitates. However, if the joint is reheated to within the critical temperature range, *e.g.* during multipass welding or to relieve residual stresses, $Cr_{23}C_6$ formation occurs in the region where the stabilising carbides dissolved. This is because at such temperatures precipitation of the thermodynamically more stable TiC/NbC is sluggish (Fig. 2.5). Consequently a sharply defined zone becomes depleted in chromium and suffers from increased intergranular corrosion, as the name of the phenomenon implies.

NAG steel, however, appears immune to both of these forms of corrosive attack as their low carbon content prevents significant carbide formation.

iii) Effect of sulphur

The weldability of steels is affected by surface tension driven flow, known as Marangoni convection (Velarde and Normand, 1980). The temperature dependence of the surface tension of liquid steel can be altered by additions of sulphur (Halden and Kingery, 1955). At low concentrations the melt has a negative temperature coefficient of surface tension producing upward flow at the weld pool centre. This leads to poor penetration and unsatisfactory welds (Fig. 2.7a). With higher levels of sulphur, the temperature coefficient of surface tension becomes positive and downward flow occurs at the weld pool centre. The desired degree of penetration

Fig. 2.6 - (a) Curves showing the variation of temperature with time at various points adjacent to a weld in austenitic stainless steel and (b) the resultant weld decay (Shreir *et al.* 1994).

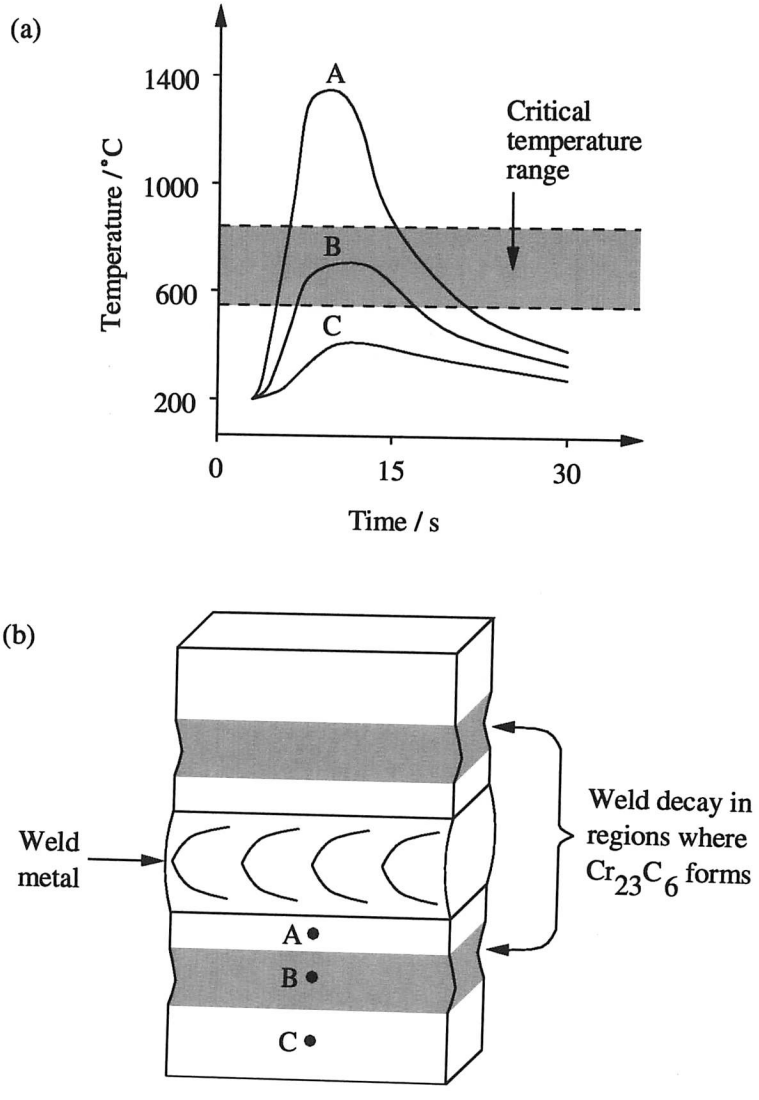

Fig. 2.7 - Effect of sulphur on weld pool flow and penetration.
(a) Low sulphur and (b) high sulphur (David and Vitek, 1989).

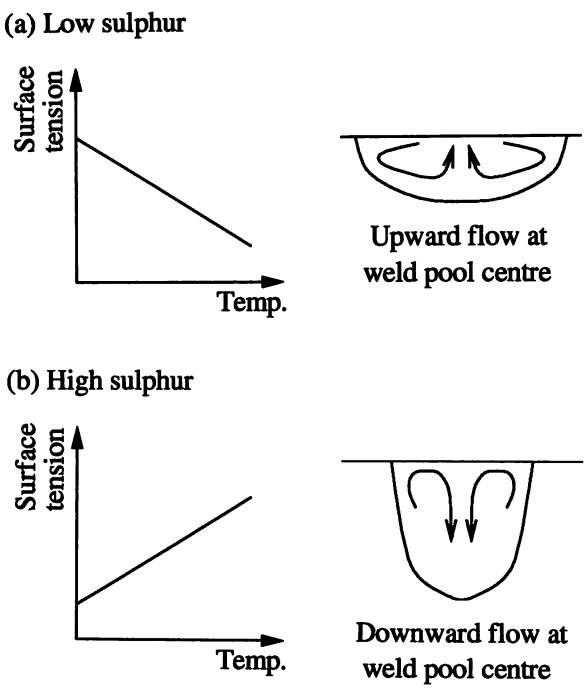

can thus be achieved (Fig. 2.7b). However, whilst a higher sulphur content is beneficial to weldability, it can have an adverse effect on the corrosion resistance of the steel (Section 2.2.1).

2.2.3 - Summary of NAG steel composition

The deleterious effects of many trace elements on corrosion resistance and weldability are reduced in NAG steel compared with most other austenitic grades. The principal reductions are in carbon, nitrogen and boron content, which prevents chromium carbide, nitride and boride precipitation. Localised chromium depletion is thus eliminated and intergranular corrosion resistance greatly improved. Molybdenum and sulphur can provide some beneficial effects hence are added in optimal quantities. The compositions of AISI (American Iron and Steel Institute) NAG304L plate and 308S92 welding wire, which are used throughout this study, are given in Table 2.1. The composition ranges of some other important austenitic grades, which will be referred to in later sections, are also shown for comparison. These include Mo-rich AISI 316, used in environments where chloride ions are prevalent, and titanium and niobium stabilised AISI 321 and 347 respectively.

Table 2.1 - Compositions of austenitic stainless steels (all in wt%, Fe to balance).

AISI grade	NAG304L (Plate)	308S92 (Wire)	304	310	316	321	347
Cr	18.5	19.5	18–20	24–26	16–18	17–19	17–19
Ni	10.2	9.9	8–12	19–22	10–14	9–12	9–13
C(max)	0.01	0.01	0.08	0.25	0.08	0.08	0.08
Mn	1.33	1.61	1–2	1–2	1.5–2	1–2	1–2
Si(max)	0.4	0.4	0.8	0.8	0.8	0.8	0.8
P(max)	0.02	0.02	0.04	0.04	0.04	0.04	0.04
S(max)	0.004	0.009	0.012	0.012	0.012	0.012	0.012
N	0.02	0.02	0.01–0.07	0.01–0.07	0.01–0.07	0.01–0.07	0.01–0.07
B	0.0012	0.0009	0.005	0.005	0.005	0.005	0.005
Mo	0.25	0.18	0.2	0.2	2–4	0.2	0.2
Ti	—	—	—	—	—	5×%C	—
Nb	—	—	—	—	—	—	10×%C

2.3 - Phase transformations in austenitic stainless steel during welding

2.3.1 - Introduction

The aim of the present study was to grain refine austenitic weld metal. To do this it is useful to understand the phase transformations that may occur in such material. However, the phase equilibria of austenitic stainless steels are dependent on a number of their components (Section 2.1). Fortunately, the study of phase equilibria has been made simpler by the recent advent of computer programs capable of estimating the equilibrium state for multi-component, multi-phase systems. The National Physical Laboratory's Metallurgical and Thermochemical Data Bank (MTDATA) works by combining experimentally determined data for unary, binary and ternary sub-systems using thermodynamic solution theory to estimate the overall result for larger systems (Hodson, 1989). For any given system MTDATA calculates the compositions and volume fractions of the phases present by minimising the Gibbs free energy whilst conserving mass. However, the reliability of calculations is dependent on the availability of data for all of the sub-systems.

2.3.2 - Phase equilibria during solidification of AISI 308S92 weld metal

Throughout the present study, AISI 308S92 filler wire was used during welding. The phase equilibria for this material were thus investigated. The composition of AISI 308S92 entered into MTDATA is given in Table 2.1. The phases included in the calculations are listed in Table 2.2. Phase equilibria were determined within the temperature range 300–2000 K.

Table 2.2 - Phases included in MTDATA calculations on AISI 308S92.

Liquid	Laves-phase	π-phase
Austenite	M_2C	Cr_2N
Ferrite	M_6C	Cr_2B
Cementite	M_2C_3	Fe_3P
Graphite	M_7C_3	FeS
σ-phase	$M_{23}C_6$	MnS

Fig. 2.8 - MTDATA calculated equilibrium phase fractions during solidification of AISI 308S92. Below ~1300 °C the steel is fully austenitic.

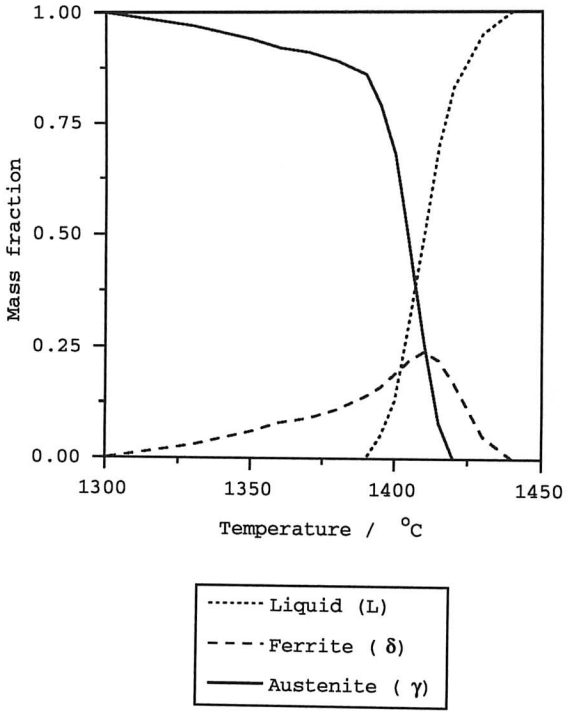

Fig. 2.9 - Solidification front in AISI 308S92.

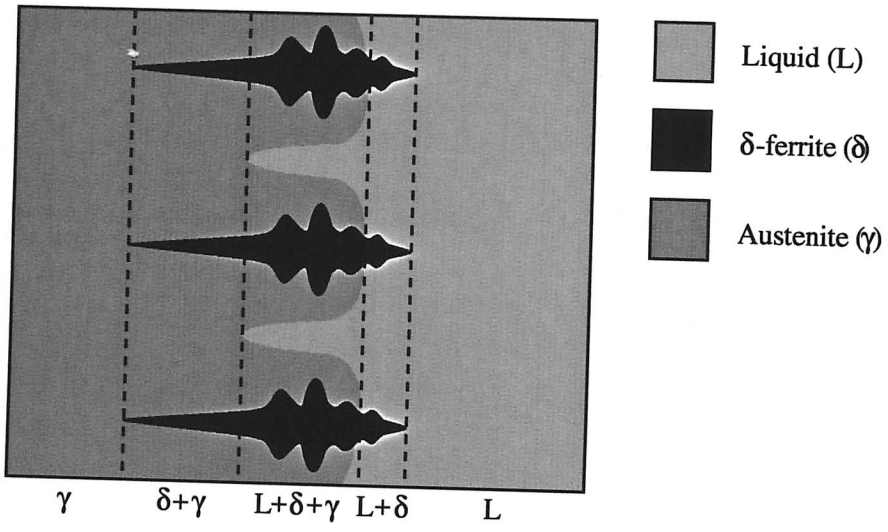

Fig 2.10 - MnS fraction as a function of temperature in AISI 308S92. The dashed line indicates the steel melting point.

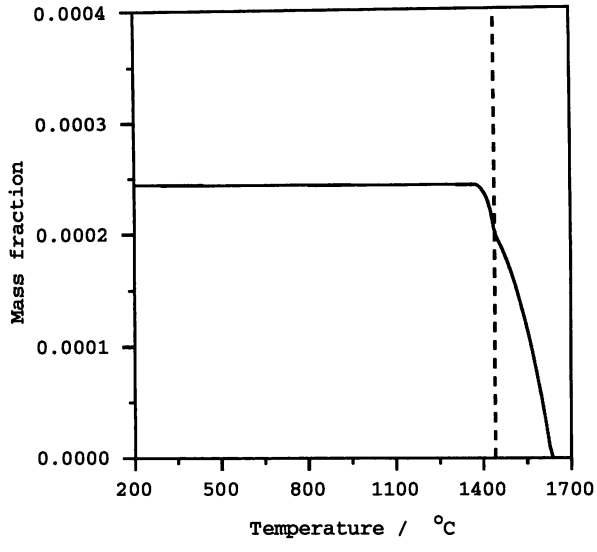

It was found that initial solidification is to δ-ferrite. However, a larger proportion of austenite also forms directly from the liquid. On cooling, all of the δ-ferrite transforms to austenite. Thus the overall equilibrium solidification sequence was found to be $L \rightarrow L + \delta \rightarrow L + \delta + \gamma \rightarrow \delta + \gamma \rightarrow \gamma$. A plot of the phase fractions as a function of temperature is shown in Fig. 2.8. A schematic diagram of the solidication front based on these results is shown in Fig. 2.9. The only other phase present was a small quantity of MnS, which forms in the liquid and is stable down to room temperature. The MnS fraction as a function of temperature is shown on an expanded scale in Fig. 2.10. As expected from the low carbon, nitrogen and boron contents of the steel, no carbides, nitrides or borides were calculated to exist at any temperature.

It must be remembered, however, that MTDATA only predicts what is possible thermodynamically. The kinetics during solidification strongly influence phase formation and thus can affect the solidification sequence and allow retention of phases outside of their equilibrium boundaries.

During welding cooling rates are relatively high, hence weld pool solidification is considered a non-equilibrium process. Fredriksson (1972) investigated the effects of cooling rate on δ/γ formation by directional solidification of an Fe-18Cr-8Ni wt% austenitic stainless steel. At higher cooling rates the kinetics allowed less time for the $\delta \rightarrow \gamma$ transformation to occur, hence δ-ferrite could be retained at room temperature.

Therefore, despite the thermodynamic calculations, we might expect the microstructure of AISI 308S92 austenitic weld metal to contain a certain amount of residual δ-ferrite, which is beneficial in preventing hot-cracking (Section 2.2.2).

2.3.3 - Microstructure of AISI 308S92 weld metal

Austenite and residual δ-ferrite within the weld microstructure can be revealed by using different etching techniques (Vander-Voort, 1984). The sample used to illustrate these methods was a single-pass bead-on-plate TIG weld (Section 5.2.2). Sections of the weld were hot-mounted in conductive bakelite, ground flat on abrasive SiC papers and polished with 1 μm diamond paste.

i) Electrolytic oxalic acid etch

A polished weld section mounted in conductive bakelite, and another piece of NAG stainless steel were used as electrodes. The two were immersed in a saturated solution of oxalic acid ($C_2H_2O_4$), prepared by dissolving 10 g of crystals in 100 ml of distilled water. The electrodes

were connected to a constant voltage power source, with the sample to be etched being made the anode. A strip of nickel was held against the weld section as a contact so that the circuit could be broken (and thus etching stopped) at any time. A 6 V d.c. potential was applied with the electrodes placed approximately 25 mm apart, which drew a current of about 1 A. After etching for 30 s the δ-ferrite structure within the weld metal was clearly revealed whereas the fully austenitic parent material was unaffected (Fig. 2.11).

ii) Mixed acids etch

10 ml acetic acid
10 ml HNO_3
15 ml HCl
5 drops of glycerol

Samples were etched by swabbing the solution over the polished surface for 20–30 s, after which both the δ-ferrite weld structure and austenite grains in the parent material could be seen. The greater corrosion of δ-ferrite within the weld, however, masked the columnar austenite grain boundaries with the exception of a few which underwent enhanced delineation near to the fusion line (Fig. 2.12).

iii) Ferric chloride based etch

30 g $FeCl_3$
20 ml H_2O
10 ml HCl
3 ml HNO_3

Samples were etched by swabbing the solution over the polished surface for about 15 s. The columnar austenite grains could be clearly seen even at very low magnifications, indicating the coarseness of the microstructure (Fig. 2.13a). Higher magnifications revealed the skeletal residual δ-ferrite structure present within each austenite grain (Fig. 2.13b).

The MnS predicted to exist by MTDATA was present in the form of isolated, globular, sub-micron inclusions. The morphology and distribution corresponded to that frequently reported for MnS, which forms as a liquid phase within the molten steel (Salter, 1979; Hale and Nutting, 1984). Fig. 2.14 shows a bright field TEM (transmission electron microscopy) image of a MnS inclusion from AISI 308S92 weld metal.

Fig. 2.11 - AISI 308S92 weld metal etched in oxalic acid.

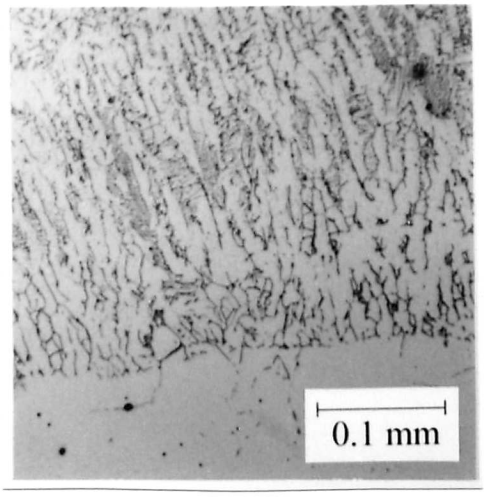

Fig. 2.12 - AISI 308S92 weld metal etched in mixed acids.

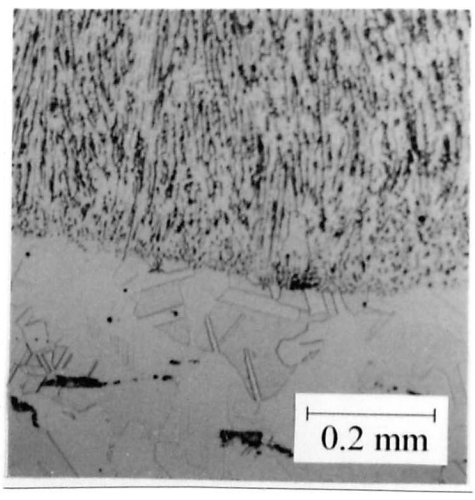

Fig. 2.13 - AISI 308S92 weld metal etched in ferric chloride based solution. (a) Low magnification and (b) high magnification.

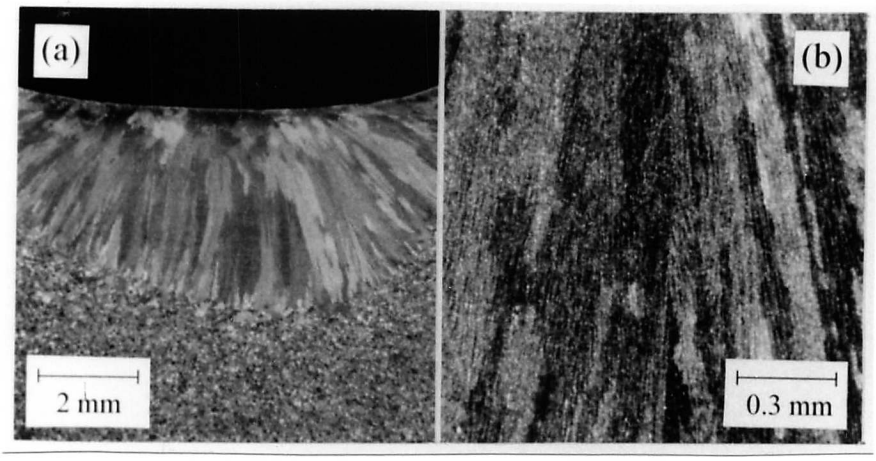

Fig. 2.14 - Bright field TEM image of MnS inclusion in AISI 308S92 weld metal (courtesy D. Tricker).

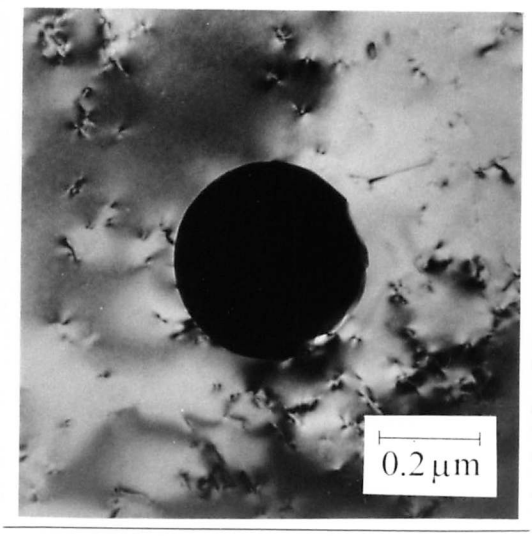

2.4 - Summary

Numerous alloying additions influence the corrosion resistance and weldability of austenitic stainless steels. NAG material used in nuclear fuel reprocessing plant has a composition designed to optimise these properties. Therefore, proposed methods of grain refinement should aim to have as low an impact on steel composition as possible.

Phase equilibria calculations have shown that AISI 308S92 filler wire solidifies to a mixture of δ-ferrite and austenite. Under equilibrium conditions the steel is fully austenitic at room temperature. However, during welding, kinetic conditions permit the retention of a small volume fraction of δ-ferrite.

Chapter 3 - Grain refinement

3.1 - Introduction

Grain refinement is a key metallurgical process which provides important benefits in a number of materials and applications, and has thus been investigated extensively. A reduction in grain size is a fundamental strengthening mechanism in polycrystalline materials where yielding is propagated between grains by dislocation pile-ups at boundaries, producing stress concentrations large enough to initiate slip in adjacent grains. When the grain size is small, fewer dislocations can participate in the pile-up within each grain, so a higher applied stress is required before the material will yield. The relationship between the lower yield stress of a material, σ_y, and the grain size, d, is given by

$$\sigma_y = \sigma_i + k_y d^{-1/2} \tag{3.1}$$

where σ_i is a friction stress which opposes the glide of dislocations and k_y is a constant associated with the propagation of deformation across boundaries (Hall, 1951; Petch, 1953). For example, the yield stress of mild steel increases by 400 MPa as the grain size is reduced from 0.25 to 0.0025 mm. It is also possible to alter microstructural morphology via grain refinement, *e.g.* promote the columnar-to-equiaxed transition (CET) in castings and welds. This is essential to achieve the aim of the present study.

In any instance the most effective method of grain refinement is dependent on the material and processing route (Fig. 3.1) (Burke *et al.* 1949; Honeycombe, 1984; Honeycombe and Bhadeshia, 1995; Polmear, 1995). The aim of the present study was to refine the austenite grain structure of AISI 308S92 stainless steel weld metal. Investigations have shown that such material undergoes an allotropic transformation after solidification (Section 2.3.2). However, only a small volume fraction is subject to the $\delta \rightarrow \gamma$ transformation; the majority of the steel solidifes directly from the liquid as austenite which is retained down to room temperature. Thus, for grain refinement purposes, it is more useful to consider AISI 308S92 weld metal as a single phase material.

One practical way to grain refine such material would be to increase the number density of new crystals growing in the liquid ahead of the solidification front. Columnar grain growth can thus be stifled and an equiaxed structure will result (Fig. 3.2) (Hunt, 1984). This can be achieved by using dynamic stimuli to fragment the solid at the solid/liquid interface, or by introducing solid second phase particles into the melt to provide nucleation sites.

Fig. 3.1 - Examples of grain refinement methods.

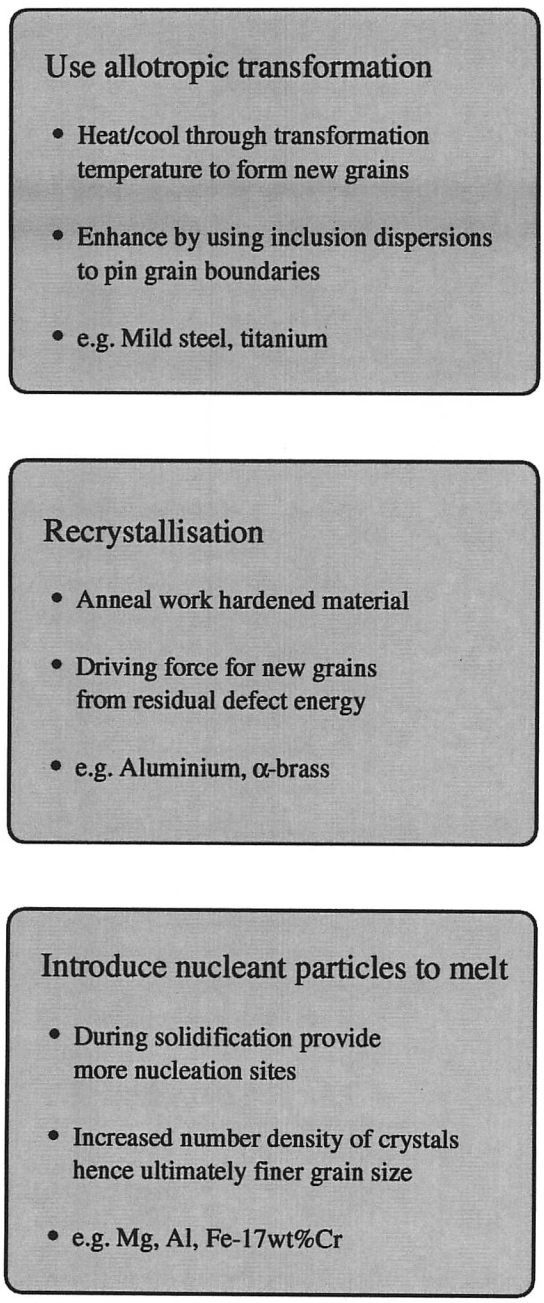

Fig. 3.2 - Promotion of CET by crystal growth ahead of the solidification front (Hunt, 1984).

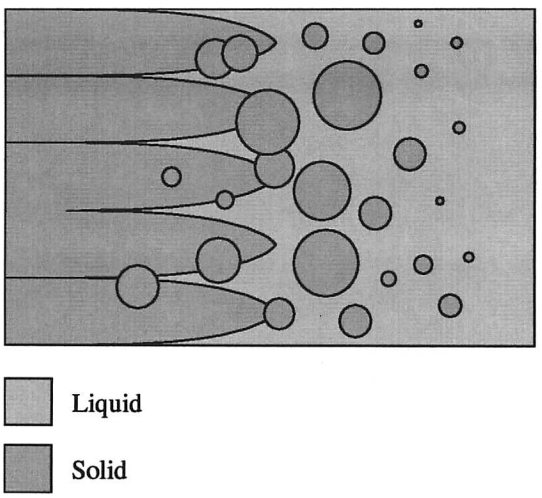

3.2 - Grain refinement by dynamic stimulation

3.2.1 - Introduction

Fragments of growing dendrites can be broken off if a solidifying columnar interface is physically disturbed. If enough fragments survive and grow then columnar development can be stifled, leading to a refined equiaxed microstructure (Davies and Garland, 1975). However, for this to occur, fragments must remain in the constitutionally undercooled region ahead of the solidification front (Section 3.2.2).

Several methods of inducing the necessary disturbances have been attempted in order to refine the grain structures of welds. Vibrations can be induced into the weld pool; pulsed currents and the associated variation in arc force can disturb normal pool solidification; electromagnetic fields can be used to stir the weld pool. Sections 3.2.3–3.2.6 review these attempts, their merits and shortcomings.

3.2.2 - Constitutional undercooling

Constitutional undercooling arises during the solidification of alloys (Tiller *et al.* 1953; Tiller and Rutter, 1956). The phenomenon does not occur in pure metals. However, commercially pure grades still contain sufficient impurities to induce alloy solidification characteristics.

Alloys do not have a single freezing temperature. Instead, solidification occurs between the liquidus and solidus temperatures. These temperatures vary as a function of composition, and at any given temperature the solid and liquid in equilibrium with one another are of different compositions.

Consider the solidification of an alloy of nominal composition C_0, assuming no diffusion in the solid and only diffusional mixing in the liquid. At the onset of plane front solidification the liquid composition at the interface is C_0. The first solid to form is in equilibrium with this liquid, and therefore has a composition kC_0, where k is the equilibrium partition coefficient, taken here to be < 1. $k = C_S^*/C_L^*$, where C_S^* and C_L^* respectively are the equilibrium compositions of the solid and liquid co-existing at the interface at a given temperature. The temperature at the interface, T^*, is the liquidus temperature corresponding to C_L^*, thus initially $T^* = T_{L(C_0)}$.

As solidification continues, solute is rejected at the interface and a boundary layer enriched in solute builds up in the liquid immediately ahead of the solidification front (Fig. 3.3a). A concurrent enrichment of the solid at the interface also occurs since equilibrium is maintained and $C_S^* = kC_L^*$. The interface temperature falls correspondingly. After a short time, steady state solidification conditions are attained (Fig. 3.3b).

Fig. 3.3 - Phase diagrams and composition profiles during solidification; (a) initial stages and (b) steady state. (c) Condition for constitutional undercooling.

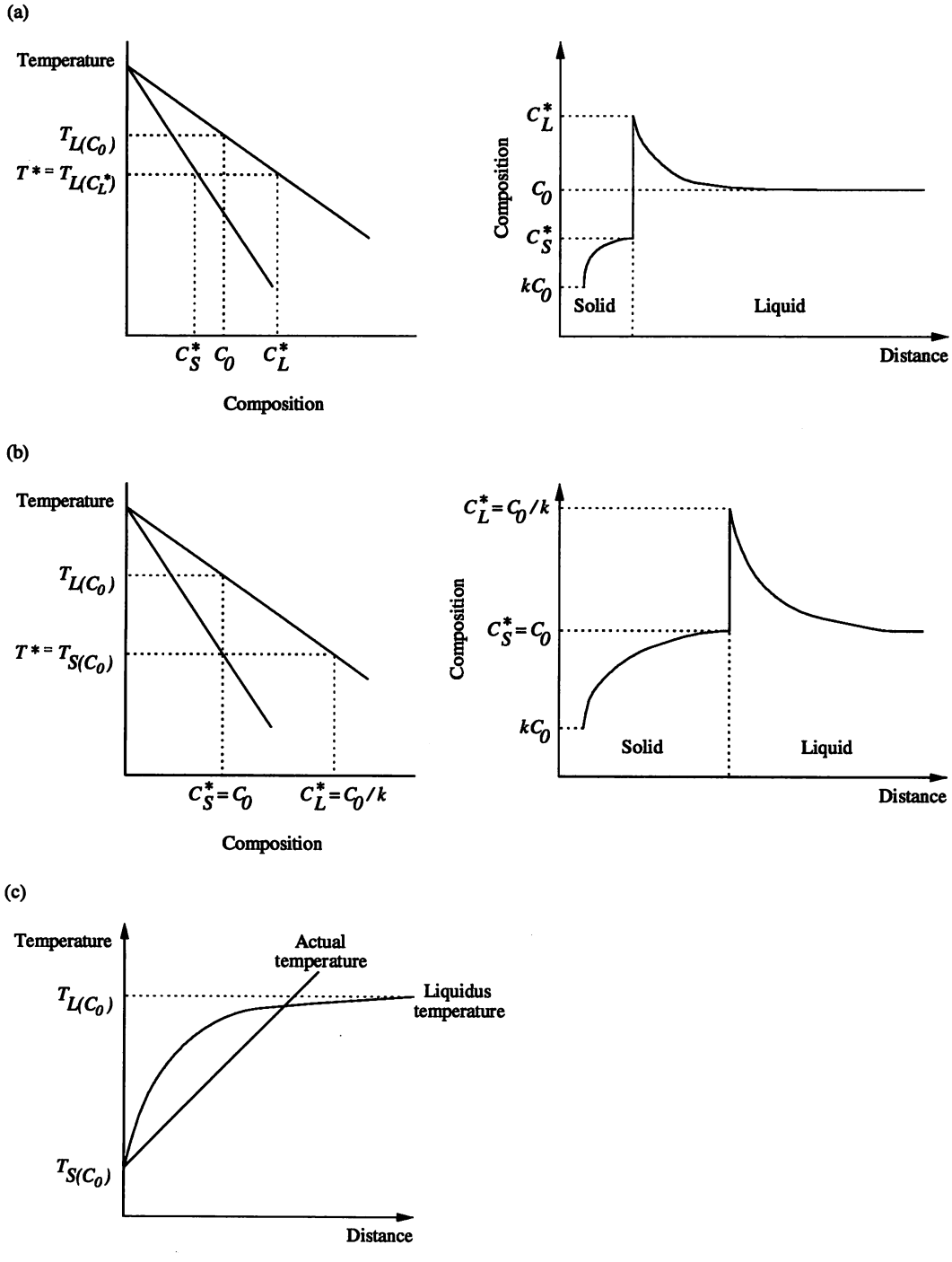

The resultant compositional gradient means that the liquidus temperature of the melt varies as a function of distance ahead of the solidification front. Because a thermal gradient also exists across the interface, it is thus possible for the actual temperature of the liquid within a region ahead of the solidification front to be lower than the liquidus temperature (Fig. 3.3c). Within this zone of *constitutional undercooling*, solid perturbations, *e.g.* detached crystal fragments, can survive and grow.

3.2.3 - Grain refinement by induced vibration

Weld pool vibration has been demonstrated to grain refine welds of aluminium and mild steel. Vibrating the electrode parallel to the welding direction, with an amplitude of 1.2 mm at frequencies in the range 10–30 Hz, produced extensive grain refinement in TIG welds on Al-2 wt% Mg alloy sheet up to 3.2 mm thick (Garland, 1974). The motion of the arc caused backwashing of liquid over the solidifying interface, which periodically fragmented, providing the crystal multiplication necessary to form an equiaxed structure. However, refinement was only achieved within a narrow range of conditions, determined by the welding speed, current and plate thickness (Fig. 3.4). With identical conditions, no grain refinement occurred in welds across AISI 321 stainless steel sheet. It was only by increasing the vibration amplitude to 1.8 mm on very thin (2 mm) plate that refinement was attained.

Experiments have also been performed by welding across a mild steel plate clamped to a vibrating table (Tewari, 1993; Tewari, 1999). Grain refinement occurred at much higher frequencies (up to 300 Hz) and much smaller amplitudes (up to 30 μm) of vibration compared with Garland's work, but although optimum parameter values were found, the results could not be explained.

The widely differring degrees of disturbance required to initiate a CET demonstrate that the conditions for grain refinement by vibration are dependent on the material and weld geometry.

3.2.4 - Grain refinement by current pulsing

Grain refinement can be induced by welding with a modulated arc, in which the current is applied in a series of short pulses. The pulse profile has several variables, such as peak, base and average current, and the base current time to peak current time ratio (t_b/t_p) (Fig. 3.5). All of these can affect the nature of the resulting disturbance and hence the degree of refinement that occurs.

Fig. 3.4 - Range of operating parameters yielding grain refinement during welding with a vibrating electrode (25 Hz, 1 mm vibration amplitude) across Al-2 wt% Mg plate 2.5 mm thick (Garland, 1974).

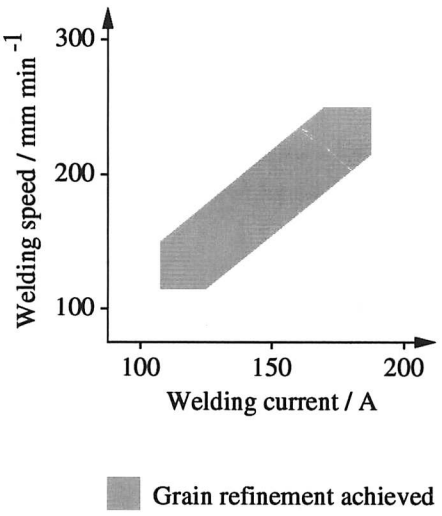

Fig. 3.5 - A typical arc modulation program.

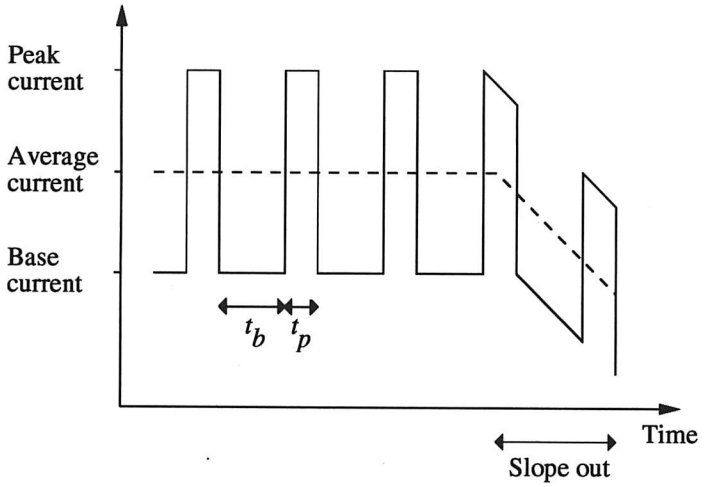

Use of this method successfully generated refinement in AISI 321 stainless steel welds, with distinctive growth bands indicating the effect of the arc modulation in disrupting solidification (Garland, 1974). The fluctuations were assumed to cause the crystal fragmentation necessary for refinement.

Further work revealed flaws in this explanation (Scott-Lawson, 1975). Whilst samples etched with mixed acids displayed an equiaxed austenitic weld microstructure, a subsequent electrolytic re-etch in oxalic acid showed the δ-ferrite structure to be columnar. The welds solidified entirely to δ-ferrite, with austenite forming on cooling via a randomly nucleated solid state transformation. The lack of refinement within the primary phase proved that crystal fragmentation did not occur, and that the equiaxed austenite structure arose from a repeated cycling through the $\delta \rightarrow \gamma$ transformation temperature as a result of the pulsed heat source. These conclusions were substantiated by the failure to achieve any grain refinement in non-transformable AISI 316 steels welded under similar conditions.

More recent experiments by Watanabe *et al.* (1987) have established conditions for producing refinement in fully austenitic AISI 310 stainless steel welds. Their investigation covered much wider parameter ranges than the work of Scott-Lawson; for example pulse frequencies of 0–100 Hz and t_b/t_p ratios from 0–20. Grain refinement by crystal fragmentation was indeed achieved, with optimum results at 2.5 Hz and a t_b/t_p ratio of 10. A refined, albeit unsound, weld was also generated at a frequency of 33 Hz. The low frequency optimum was ascribed to the degree of undercooling and the time period of the melting/freezing cycle caused by each pulse and their subsequent effects on the growth of crystal fragments. Refinement at 33 Hz coincided with the resonant frequency of the weld pool, with the resultant severe agitation providing sufficient fragmentation to stifle columnar growth, but also generating voids and variable penetration.

As with vibration induced refinement, the examples discussed here demonstrate that arc modulation can lead to the formation of equiaxed weld structures. However, the required conditions vary between materials and weld geometries and the refinement mechanism is not always crystal fragmentation.

3.2.5 - Grain refinement by electromagnetic stirring

Grain refinement of a wide range of alloys has been reported as a result of using external magnetic fields to stir the weld pool. The field is applied parallel to the axis of the electrode whereby Lorentz forces cause the arc to rotate. The rotary motion of the arc is transferred to the weld pool generating a strong stirring effect (Fig. 3.6). The use of an alternating magnetic field periodically changes the direction of flow and thus cancels out any asymmetries. Centrifugal forces acting on the arc cause it to spread out into a conical shape, creating a broader and less penetrating weld. These factors allow consistent welds of predictable shape to be produced by electromagnetic stirring (EMS).

Many early welds using EMS were concerned with aluminium alloys (Pearce and Kerr, 1981). Most of the refinement resulted from heterogeneous nucleation occurring on Ti-rich inclusions (Section 3.3.5). However, equiaxed zones were also observed in stirred welds devoid of titanium. At certain magnetic field strengths and oscillation frequencies, the stirring motion detached crystal fragments from the solid/liquid interface to block columnar grain development. A further effect of the stirring was to reduce thermal gradients and thus widen the undercooled region ahead of the solidification front. This allowed more fragments to survive, aiding the refinement process.

Similar conclusions were drawn from a study into the effects of EMS on welds of AISI 310 stainless steel, although the field strengths and frequencies required for refinement differred from those for aluminium, emphasising material dependence (Malinowski-Brodnicka *et al.* 1990).

Less successful EMS experiments have been conducted with AISI 304 and 321 stainless steels in which the austenite structures of welds performed under a wide range of conditions remained columnar (Villafuerte and Kerr, 1990a). However, the primary δ-ferrite structure, whilst columnar in AISI 304 welds, was equiaxed in AISI 321 samples. The latter class of steels contain high levels of titanium, and refinement of the δ-ferrite structure was attributed to heterogeneous nucleation on Ti-rich inclusions (Section 3.3.6).

3.2.6 - Summary

The grain refinement techniques reviewed all aimed to encourage the formation of an equiaxed structure by crystal fragmentation. However, in each case this only occurred over narrow ranges of operating parameters, which differred between materials and weld geometries. This is because the dynamic stimulation of weld pools produces two interacting effects.

Grain refinement requires a sufficient number density of crystal fragments within the undercooled region to stifle columnar growth. The degree of fragmentation is governed by the strength and nature of the applied disturbance.

Dynamic stimuli also affect weld pool solidification conditions. The ease with which a CET can occur is frequently described by the G_L/R ratio, where G_L is the thermal gradient within the liquid and R is the crystal growth rate (David and Vitek, 1989). Decreasing G_L and increasing R extends the region of constitutional undercooling (Fig. 3.7). High growth rates contribute by reducing the time available for solute diffusion away from the solidification front, hence compositional gradients become steeper. Low G_L/R ratios thus promote columnar-to-equiaxed transitions as the survival and growth of more crystal fragments is favoured.

For example, the change in solidification conditions brought about by arc modulation contribute to the observed optimum conditions for grain refinement in pulsed current welds. Watanabe *et al.* (1987) calculated the G_L/R ratio as a function of heat input into the weld, which varies strongly with pulse frequency. At very low frequencies (0.5 Hz), the value of G_L/R is large and crystal fragments do not grow extensively enough to block columnar growth. At a frequency of 2.5 Hz, the G_L/R value is sufficiently low to allow fragments to grow into an equiaxed structure. Remelting by the succeeding pulse causes some epitaxial growth and thus a few small areas of columnar character are present in the microstructure. Higher frequencies (10 Hz) generate G_L/R ratios so small that an equiaxed structure develops immediately on solidification. However, in this case, because the pulse time interval is short, the solidified distance is also short, and therefore remelting causes the granular crystals to be linked by epitaxial growth producing long columnar grains and hence no refinement. These effects are displayed schematically in Fig. 3.8.

To achieve grain refinement by dynamic stimulation, a balance must be struck whereby the disturbance produces sufficient crystal fragments and generates solidification conditions which favour growth into an equiaxed microstructure. The need for this compromise hinders the effectiveness of such refining methods. The material and weld geometry dependence means that operating parameters have to be established for each individual case, thus development of these methods is on a par with development of the specific ultrasonic test procedures they are designed to avoid. The cost and complications associated with welding equipment capable of performing these operations also reduces the significance of the benefits they may provide.

Fig. 3.6 - Generation of weld pool stirring by an applied magnetic field (Malinowski-Brodnicka *et al.* 1990).

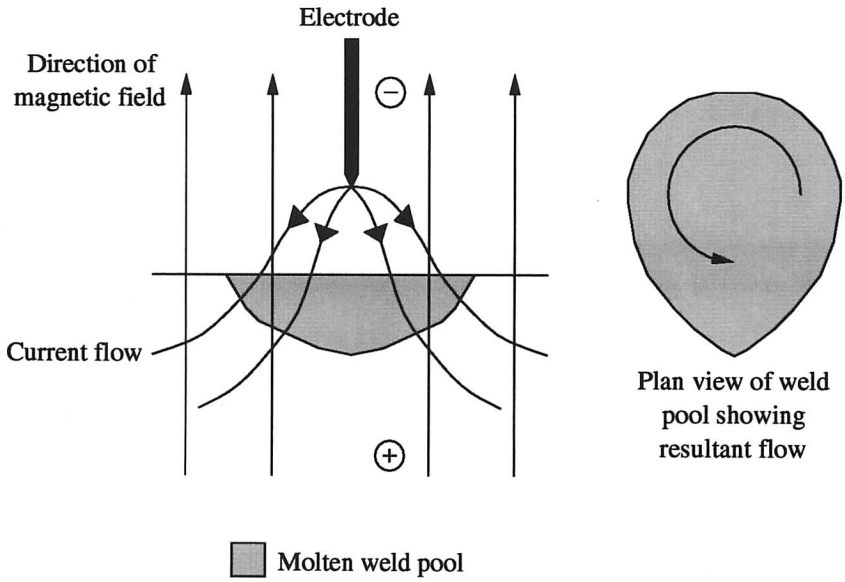

Fig.3.7 - Effect of decreasing G_L and increasing R on the extent of constitutional undercooling.

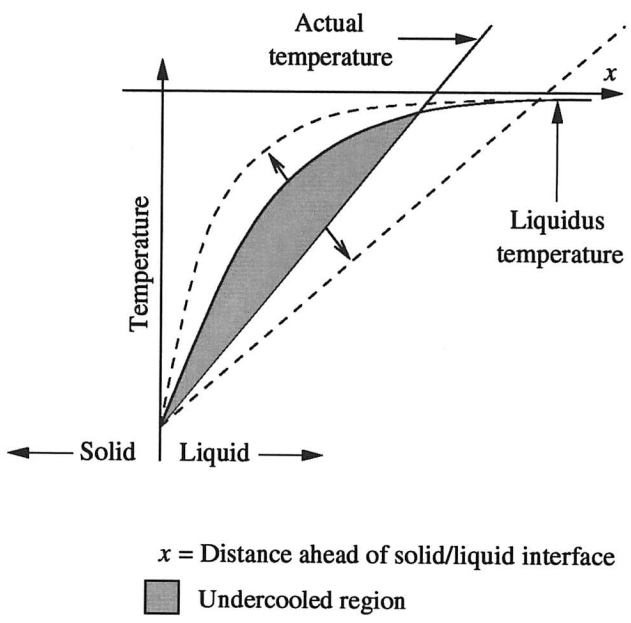

Fig. 3.8 - Variation in weld structure with arc modulation frequency (Watanabe *et al.* 1987). Dashed lines indicate successive pulses.

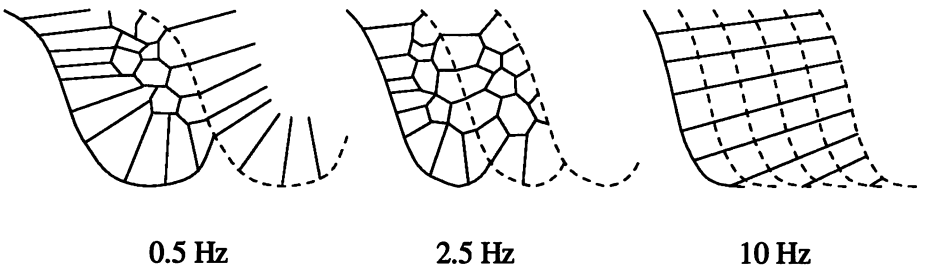

Fig. 3.9 - Effect of the number density of crystals, N, on the columnar-to-equiaxed transition (Hunt, 1984).

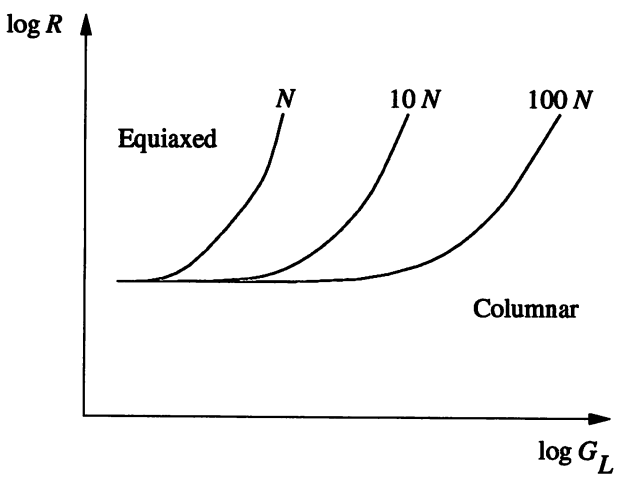

3.3 - Grain refinement by heterogeneous nucleation

3.3.1 - Introduction

For a given set of weld pool solidification conditions, the onset of a CET depends on the number density of crystals in the liquid ahead of the solidification front (Fig. 3.9) (Hunt, 1984). With dynamic stimulation, sufficient numbers of crystal fragments are obtained over rather narrow ranges of operating conditions. However, an increased number density of crystals can be generated if solid second phase particles are introduced to the melt to provide heterogeneous nucleation sites. Deliberate additions of nucleants can be made in whatever quantity is necessary.

For a given phase, some particles are more effective heterogeneous nucleants than others. There is no established nucleant for austenite. To rectify this situation it is therefore useful to examine heterogeneous nucleation theory and its application to the grain refinement of other phases.

3.3.2 - Theory of heterogeneous nucleation

Homogeneous nucleation is defined as nucleation without the aid of a foreign body (Christian, 1975; Porter and Easterling, 1992). Below the equilibrium melting point of a material, T_m, the free energy of the solid becomes lower than that of the liquid, thus formation of solid particles produces a negative volume free energy change. However, the energy required to form a solid/liquid interface opposes this. The change in free energy on formation of a solid sphere of radius r is given by

$$\Delta G_{hom} = \frac{-4\pi r^3 \Delta G_V}{3} + 4\pi r^2 \gamma_{SL} \tag{3.2}$$

where ΔG_V is the magnitude of the difference in free energy per unit volume of solid and liquid, and γ_{SL} is the solid/liquid interfacial free energy per unit area.

For small values of r, the surface energy term dominates, hence the free energy increases on formation of a solid embryo. However, with increasing r, the free energy reaches a maximum and thereafter falls. Thus there is an energy barrier to homogeneous nucleation

$$G^*_{hom} = \frac{16\pi\gamma^3_{SL}}{3\Delta G^2_V} \tag{3.3}$$

which occurs at a critical particle size

$$r^* = \frac{2\gamma_{SL}}{\Delta G_V} \tag{3.4}$$

obtained by differentiation of Equation 3.2 (Fig. 3.10). Beyond r^* particle growth reduces the free energy. Particles in this condition are called nuclei.

The activation energy means that solidification by homogeneous nucleation usually occurs at large undercoolings. For example, nickel can be undercooled by 250 K below T_m before it begins to solidify (Turnbull and Cech, 1950). In practise, however, undercoolings of more than a few kelvin seldom occur. This is because the walls of the liquid container and solid impurity particles catalyse solidification. This phenomenon is called *heterogeneous nucleation* (Christian, 1975; Porter and Easterling, 1992).

For isotropic systems, interfacial energy is minimised if an embryo forms as a spherical cap on a flat substrate (Fig. 3.11), with a characteristic *wetting angle*, ψ, determined by the balance of the various surface energies involved, such that

$$\gamma_{ML} = \gamma_{SM} + \gamma_{SL}\cos\psi \tag{3.5}$$

where γ_{ML}, γ_{SM} and γ_{SL} are the free energies per unit area of the substrate/liquid, solid/substrate and solid/liquid interfaces respectively. The formation of such an embryo is associated with an excess free energy given by

$$\Delta G_{het} = -V_S\Delta G_V + A_{SL}\gamma_{SL} + A_{SM}\gamma_{SM} - A_{SM}\gamma_{ML} \tag{3.6}$$

where V_S is the volume of the spherical cap, A_{SL} is the area of the solid/liquid interface and A_{SM} is the area of the solid/substrate interface (Equations 3.7–3.9). Of the three interfacial energy terms, the first two concern interfaces created during the nucleation process, hence are positive, whilst the third arises from the destruction of the substrate/liquid interface under the embryo and thus gives a negative energy contribution.

$$A_{SL} = 2\pi r^2(1-\cos\psi) \tag{3.7}$$

$$A_{SM} = \pi r^2 \sin^2\psi \tag{3.8}$$

$$V_S = \pi r^3(2+\cos\psi)(1-\cos\psi)^2/3 \tag{3.9}$$

It follows that

$$\Delta G_{het} = \left\{\frac{-4\pi r^3\Delta G_V}{3} + 4\pi r^2\gamma_{SL}\right\}S(\psi) \tag{3.10}$$

where

$$S(\psi) = (2+\cos\psi)(1-\cos\psi)^2/4 \tag{3.11}$$

Except for factor $S(\psi)$, this expression is the same as that obtained for homogeneous nucleation (Equation 3.2). $S(\psi)$ is dependent only on the wetting angle, *i.e.* the shape of the embryo,

Fig. 3.10 - Comparison of the free energy of formation as a function of particle radius for homogeneous and heterogeneous nucleation (Porter and Easterling, 1992).

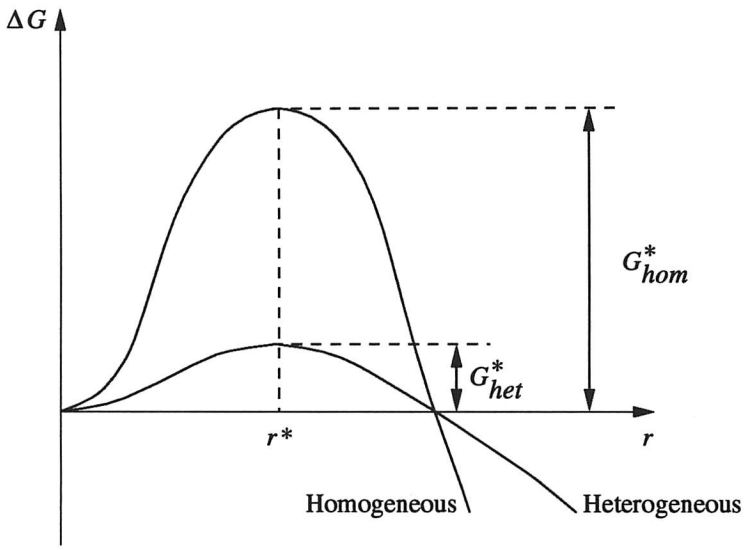

Fig. 3.11 - Heterogeneous nucleation of a spherical cap of radius r on a flat substrate (Porter and Easterling, 1992).

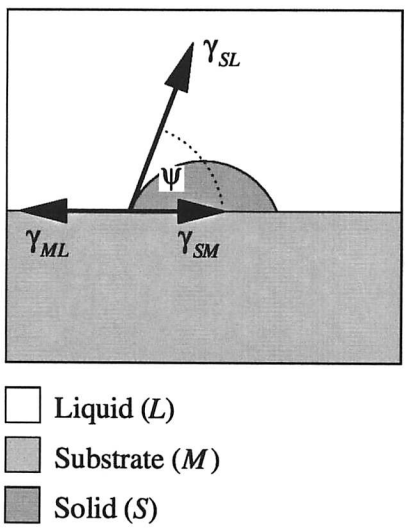

and has a value of ≤ 1. Differentiation of Equation 3.10 shows that the energy barrier to heterogeneous nucleation G^*_{het} is thus smaller than G^*_{hom} by the shape factor $S(\psi)$:

$$G^*_{het} = \frac{16\pi\gamma^3_{SL}}{3\Delta G^2_V} \cdot S(\psi) \tag{3.12}$$

although the critical nucleus radius r^* remains the same:

$$r^* = \frac{2\gamma_{SL}}{\Delta G_V} \tag{3.12}$$

Therefore, heterogeneous nucleation always provides an easier route for solidification than homogeneous nucleation, and at low wetting angles the reduction in the energy barrier to nucleation can be dramatic, as shown in Fig. 3.10.

3.3.3 - Nucleant potency

The wetting angle determines the magnitude of the reduction in the energy barrier to nucleation. The wetting angle itself is determined by interactions between the solid, liquid and substrate phases, hence factors such as the chemical nature of the substrate, the electrostatic potential between the phases, and the structure of the solid/substrate interface play an important role.

Turnbull and Vonnegut (1952) proposed that when all chemical parameters are favourable, *i.e.* bond type and strength of the solid and substrate are similar, only structural aspects of the interface contribute to the energy barrier to heterogeneous nucleation. This has been shown to apply to the nucleation of magnesium, aluminium and ferrite from the liquid on specific solid particles. These systems will be reviewed in Sections 3.3.4–3.3.6.

The energy of the interface as a result of its structure is dependent on the similarity between the lattices of the solid and substrate. The closer the lattice matching, the lower the interfacial energy, and hence the lower the barrier to nucleation. The lattice mismatch, also commonly referred to as the disregistry, depends on the lattice parameters of the two crystals, and is defined as

$$\delta = \Delta a/a \tag{3.14}$$

where a is the lattice parameter of the solid and Δa is the magnitude of the difference between the lattice parameters of the solid and substrate.

If the nucleus can be strained by an amount ε in the plane of the interface such as to completely accommodate the mismatch the interface will be in forced coherence with a volume strain energy proportional to ε^2 (Fig. 3.12a). If the level of strain required is very high, *i.e.*

when the lattice mismatch is large, a semi-coherent interface tends to form, in which regions of good fit are interspersed by dislocations (Fig. 3.12b). The interfacial dislocation density is proportional to δ, and the energy associated with the dislocations contributes to the interfacial energy. Fig. 3.13 shows how the energy barrier to heterogeneous nucleation and the type of interface that forms varies with lattice mismatch.

3.3.4 - Grain refinement of magnesium

Grain refinement of magnesium can be achieved by alloying with zirconium (Emley, 1966; Polmear, 1995). The most effective results are obtained by additions of around 0.6 wt%. During solidification, small zirconium particles first separate from the liquid. At 654°C a peritectic reaction occurs in which zirconium reacts with the liquid to form magnesium. This reaction is nucleated on the existing zirconium particles. Evidence for this is provided by the metallic pips which always occur at the centre of grains in refined Mg–Zr alloys. Microprobe analysis of such pips shows them to be zirconium.

Magnesium and zirconium exhibit very close lattice matching (Mg: hexagonal, a=3.20 Å, c=5.20 Å and Zr: hexagonal, a=3.23 Å, c=5.14 Å), with a disregistry of just 0.94% between parallel close-packed planes. The energy barrier to nucleation is thus very low and effective heterogeneous nucleation can easily occur.

However, only relatively pure magnesium alloys can be refined by zirconium (Glasson and Emley, 1968). If elements such as Al, Mn, and Zn are also present then the process is disrupted by the formation of intermetallic compounds with zirconium. Consequently the number of pure zirconium particles available as nucleation sites is reduced. Additions of powdered elemental zirconium to magnesium casts are also ineffective in generating refinement (Roberts, 1960). The high oxidation tendency of zirconium results in powder particles being coated by surface oxide layers. When such particles are added to a solidifying melt, these layers inhibit the formation of the Mg–Zr interface necessary for effective nucleation.

Grain refinement of autogenous TIG welds across magnesium sheet has been observed in alloys containing zirconium (Bailey and Scott-Lawson, 1975). The weld microstructure was finer than that of the parent material, although this was ascribed to the high cooling rates within the weld pool. Consistent with casting practice, minute zirconium pips were found at the centres of weld grains, indicating the role of zirconium in providing heterogeneous nucleation sites.

Fig. 3.12 - Atomic configurations at (a) forced coherent and (b) semi-coherent interfaces (Turnbull and Vonnegut, 1952).

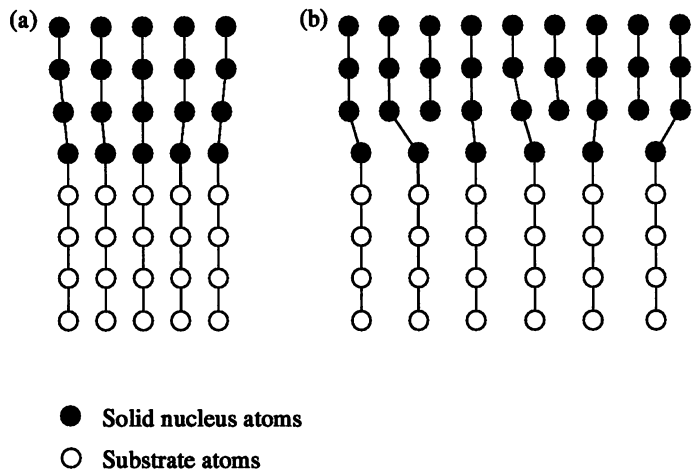

Fig. 3.13 - Variation in heterogeneous nucleation barrier and type of interface as a function of lattice mismatch (Turnbull and Vonnegut, 1952).

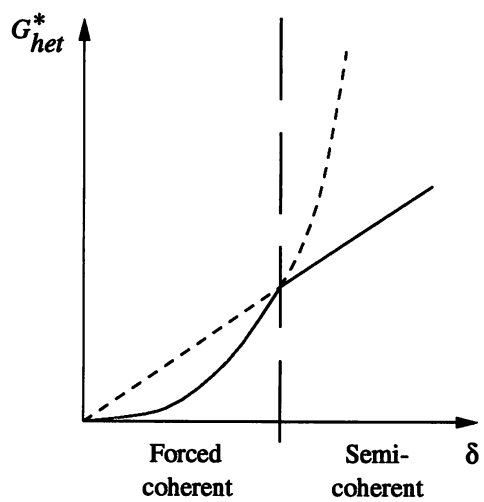

3.3.5 - *Grain refinement of aluminium*

The grain refinement of commercial aluminium alloys is performed by adding rods of master alloy, containing inoculants, to liquid metal (McCartney, 1989). The composition of the master alloy is typically Al-5Ti-1B wt%. The effects of Ti and B additions on aluminium microstructure were first identified by Cibula (1949).

For many years, however, the refinement mechanism was unclear. Cibula (1952) had proposed that aluminium nucleated from the liquid on TiB_2 particles, whereas Crossley and Mondolfo (1951) suggested that a peritectic reaction induced aluminium to nucleate on intermetallic Al_3Ti.

TiB_2 has a low lattice mismatch with aluminium (5.9% for $(111)_{Al} \parallel (0001)_{TiB_2}$, $[1\bar{1}0]_{Al} \parallel [11\bar{2}0]_{TiB_2}$) and is virtually insoluble in the liquid even at low Ti and B concentrations. However, adding TiB_2 powder to a pure aluminium melt does not lead to a greater nucleation rate (Mohanty and Gruzleski, 1995). The TiB_2 inclusions are instead pushed to the grain boundaries during solidification, indicating a lack of wetting. Thus despite the low disregistry other, presumably chemical, parameters prevent the wetting, and hence nucleation, of aluminium on TiB_2.

The addition of an excess of Ti together with the boride, on the other hand, stimulates nucleation on particles, even if the surplus of Ti is minute. Microscopy revealed Al_3Ti growing on TiB_2 inclusions at the centre of grains, indicating a two-stage process. It appears that Al_3Ti first nucleates on the boride, with aluminium then forming on Al_3Ti.

Crystallographic calculations have shown that a low mismatch of 3.8% exists between fcc aluminium and tetragonal Al_3Ti on (111) and (112) planes respectively (Hashimoto *et al.* 1983). This has been confirmed experimentally by embedding boride particles in a glassy aluminium matrix to observe the nucleation process (Schumacher *et al.* 1998). TEM revealed that aluminium nucleates on the basal faces of TiB_2 particles coated with Al_3Ti. Well defined crystallographic orientations were recorded, with $\{0001\}_{TiB_2} \parallel \{112\}_{Al_3Ti} \parallel \{111\}_{Al}$. These results imply that unlike TiB_2, Al_3Ti promotes wetting by aluminium.

Further evidence that Al_3Ti is the nucleating agent for aluminium is provided by the microstructures of master alloy additions themselves, in which TiB_2 particles are usually confined to the grain boundaries, whereas Al_3Ti particles are frequently found in grain centres (Schumacher *et al.* 1998). Thus the intermetallic is more active in catalysing solidification of the master alloy than the boride.

Fig. 3.14 - Results of MTDATA calculations showing Al_3Ti and TiB_2 stabilites in (a) master alloy and (b) commercial cast with master alloy addition.

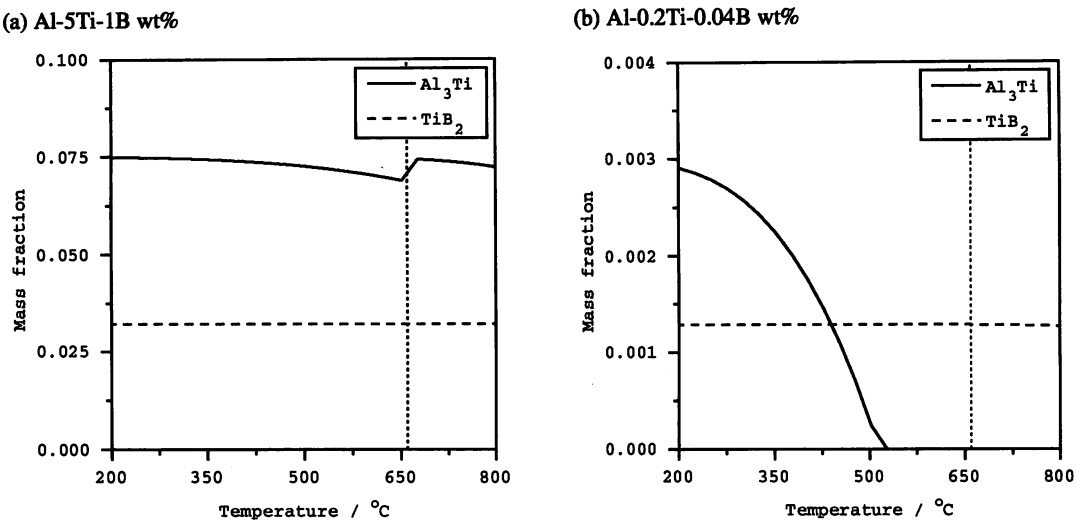

Fig. 3.15 - Effect of ΔT_n on the columnar-to-equiaxed transition (Hunt, 1984).

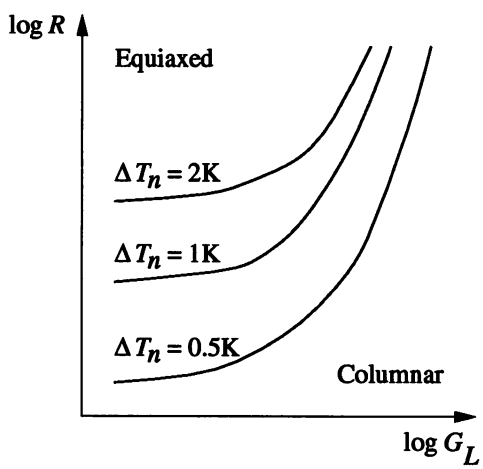

Al_3Ti can only lead to grain refinement, though, if it is present as a solid within the melt. MTDATA calculations—phases and compositions in Tables 3.1 and 3.2—illustrate that for the master alloy composition, Al_3Ti is thermodynamically stable in liquid aluminium, even at high superheats (Fig. 3.14a). A calculation using the composition of a typical cast to which master alloy has been added, shows that Al_3Ti may not survive in the melt (Fig. 3.14b). However, extensive grain refinement is nevertheless achieved. In such cases the presence of the insoluble boride is critical, because Al_3Ti can be preserved on the basal planes of TiB_2 outside its equilibrium range of stability, and hence remain present to nucleate aluminium.

Table 3.1 - Phases included in MTDATA calculations on Al-Ti-B alloys.

Liquid	Al_3Ti
fcc-Al	TiB_2

Table 3.2 - Compositions in wt% of Al-Ti-B alloys for MTDATA calculations.

Material	Al	Ti	B
Master alloy	to bal.	5	1
Commercial cast	to bal.	0.2	0.04

Dramatic grain refinement of aluminium welds via the same mechanism has also been reported when the sheet and welding consumables contained the required levels of Ti and B (Ganaha *et al.* 1980).

3.3.6 - Grain refinement of ferrite

The grain refinement of ferrite by heterogeneous nucleation on particles present in the liquid has been extensively studied. Bramfitt (1970) investigated the nucleating effects of a series of carbide and nitride inoculants on pure iron by measuring the degree of undercooling that occurred during solidification, ΔT_n. By definition, a low activation energy corresponds to a potent nucleant and a small level of undercooling before solidification is initiated. Fig. 3.15 shows the effect of ΔT_n on the ease of achieving a columnar-to-equiaxed transition.

Six compounds were found to stimulate grain refinement, with the extent of the refinement correlating with the undercooling—TiN, TiC, SiC, ZrN, ZrC and WC in decreasing order of effectiveness. If wetting is assumed then only structural aspects of the inoculants contribute to

the nucleation barrier—*i.e.* in accordance with the theory of Turnbull and Vonnegut (1952)—hence Bramfitt plotted ΔT_n as a function of the disregistry.

With the exception of the results for WC, a parabolic trend was observed (Fig. 3.16). However, Bramfitt noted that the basic disregistry equation (Equation 3.14) can only account for interfaces between planes of similar atomic arrangement, in this case $(111)_{\delta-Fe} \parallel (0001)_{WC}$. If the most closely-packed plane of ferrite is considered instead, *i.e.* $(110)_{\delta-Fe} \parallel (0001)_{WC}$, then although the atomic arrangements are dissimilar, a better fit arises.

To take account of this, Bramfitt modified the disregistry calculation such that the mismatches along the three lowest index direction combinations within a 90° quadrant of the two interfacial planes are averaged, with a $\cos\theta$ term included to resolve any angular differences. The *planar* disregistry can thus be written as

$$\delta_{(hkl)_s}^{(hkl)_m} = \sum_{i=1}^{3} \frac{|(d[uvw]_m^i \cos\theta - d[uvw]_s^i)|}{d[uvw]_s^i} \times \frac{100}{3} \tag{3.15}$$

where:- $\delta_{(hkl)_s}^{(hkl)_m}$ = Disregistry between substrate and solid in %

$(hkl)_m$ = A low index plane of the substrate

$(hkl)_s$ = A low index plane of the solid

$[uvw]_m$ = A low index direction in $(hkl)_m$

$[uvw]_s$ = A low index direction in $(hkl)_s$

$d[uvw]_m$ = The interatomic spacing along $[uvw]_m$

$d[uvw]_s$ = The interatomic spacing along $[uvw]_s$

θ = The angle between $[uvw]_m$ and $[uvw]_s$

The planar disregistry between ferrite and WC gives a mismatch of 12.7%, compared with the unmodified value of 29.4%. The modified result fits with the parabolic trend (Fig. 3.16).

Bramfitt's experiments also highlight the need for substrates to remain solid in the melt in order to act as nucleation sites. For example, although disregistry values of <1% imply that V_4C_3 and VN should be very potent nucleation catalysts, additions of these compounds yielded no grain refinement for the simple reason that they both completely dissolved in the liquid iron.

Fig. 3.16 - Variation in ΔT_n as a function of disregistry. When the disregistry calculation is modified to account for dissimilarities in atomic arrangements WC fits the parabolic trend (Bramfitt, 1970).

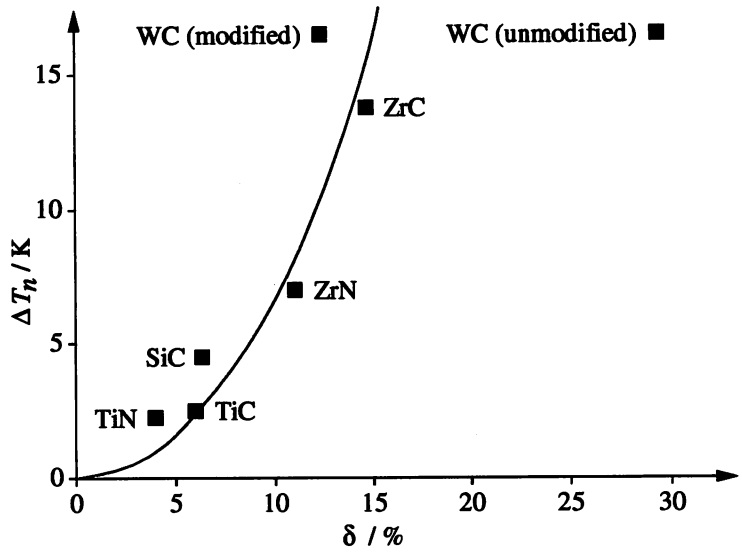

Fig. 3.17 - Phase boundaries at 1800 K for the steels used by Heintze and McPherson (1986) showing that TiN, but not TiC, could survive in the melt. Squares represent the alloy compositions. Solubility data for TiN and TiC from Morita and Kunisada (1978) and Sumito *et al.* (1981) respectively.

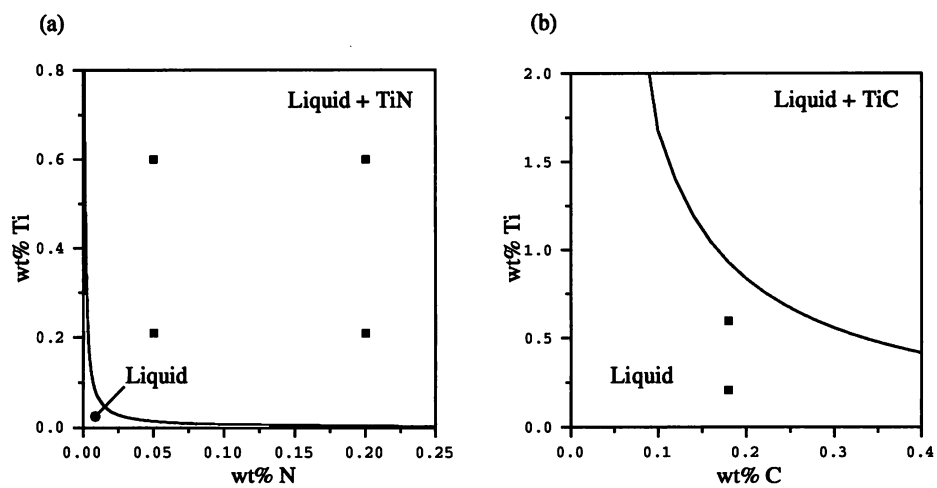

Ostrowski and Langer (1979a) reported the effectiveness of Ti additions in grain refining casts of single phase ferritic stainless steels. Electron microscopy coupled with microanalysis revealed the presence of TiN inclusions at the centres of refined grains. Bramfitt had attributed the nucleating potency of TiN to its low disregistry of 3.9% with ferrite between parallel (100) planes. However, TEM investigations showed a predominant $\{311\}_{\delta-Fe} \parallel \{100\}_{TiN}$, $< 110 >_{\delta-Fe} \parallel < 010 >_{TiN}$ orientation relationship to exist (Ostrowski and Langer, 1979b). The planar disregistry for this arrangement has an even lower value of 3.53% thus explaining its occurrence.

TiN particles have also been found at grain centres in refined ferritic stainless steel welds containing Ti. Identical additions to fully austenitic stainless steel welds did not generate refinement. Ti-alloyed austenitic welds solidifying to a mixture of δ-ferrite and austenite, however, displayed an equiaxed δ-ferrite structure whilst austenite grains remained columnar (Heintze and McPherson, 1986).

Calculation of the planar disregistry between austenite and TiN for numerous orientation relationships shows it to be large in each case. Consequently, whilst the nucleation of ferrite on TiN is facilitated by close lattice matching, nucleation of austenite is precluded for the opposite reason.

Villafuerte and Kerr (1990b) confirmed that only δ-ferrite is refined by TiN in dual phase austenitic welds. In such steels austenite begins to form at the δ-ferrite/liquid interface and grows via a solid state diffusion controlled process (Leone and Kerr, 1982). This suggests that refinement of the primary δ-ferrite phase would lead to refinement of the secondary austenite phase. However, it appears that austenite can bridge the gap between δ-ferrite grains without having to renucleate.

The need for potential nucleants to have low solubilities has been reiterated by the work on stainless steels. For example, Bramfitt's results showed that it is also possible to effectively nucleate ferrite on TiC. However, Heintze and McPherson (1986) found no carbide inclusions in their refined welds. Unlike the case for the nitride, the concentrations of Ti and C in the alloys used were too low for TiC to remain thermodynamically stable in the melt, as demonstrated by the solubility product plots in Fig. 3.17.

3.3.7 - Summary

The provision of solid impurity particles to increase the number of nucleation sites for a solidifying melt has been shown to be an effective way of grain refining a number of alloys. Magnesium, aluminium and ferrite are successfully nucleated from the liquid on Zr, Al_3Ti

and (in particular) TiN respectively. The potency of these nucleants results from close lattice matching with the nucleating phase.

The level of additions must be such that particles are thermodynamically stable and thus remain solid in the melt. For example, TiC can be a potent nucleant for ferrite, but only if the Ti and C contents of the steel are high enough to permit the survival of carbide particles above the melting point. Refinement of commercial aluminium alloys requires a dual addition of Ti and B, so that the necessary Al_3Ti nucleants are preserved outside their equilibrium range of stability on co-existing TiB_2 particles.

However, it must be remembered that the refining potential of an inoculant satisfying the disregistry and solubility criteria can still be complicated by other factors. TiB_2 meets both criteria with respect to aluminium, yet fails to provide grain refinement, and the refining action of Zr on magnesium alloys can be disrupted by the presence of other alloying elements and oxidation reactions.

3.4 - Summary

The grain refinement of austenitic stainless steel welds may be achieved by increasing the number density of crystals in the liquid ahead of the solidification front. This has previously been attempted by using dynamic stimuli to fragment the solidifying interface. Whilst some successful results were achieved, the necessary operating parameters were heavily dependent on material and weld geometry.

In contrast, the grain refinement of magnesium, aluminium and fully ferritic stainless steel welds can easily be achieved by the provision of Zr, Al_3Ti and TiN inclusions respectively to increase the number of heterogeneous nucleation sites within the solidifying melt. The effectiveness of these nucleants is primarily attributed to their close lattice matching with the nucleating phase and their low solubility in the molten alloy.

The aim of this project may thus be achieved if a potent nucleant for austenite during solidification can be established.

Chapter 4 - Inoculant selection

4.1 - Introduction

We have seen that Zr, Al_3Ti and TiN are potent nucleants for magnesium, aluminium and ferrite respectively, as they satisfy the criteria of having low lattice mismatches with the nucleating phase and being thermodynamically stable in the molten alloy. The disregistry and solubility calculations necessary to quantify these criteria are relatively easy to perform. Thus investigation of these properties for an extensive series of compounds with respect to austenitic stainless steels would be a sensible first approach to finding an effective heterogeneous nucleant for austenite.

Whilst it is fully appreciated that other factors can reduce the potency of nucleants meeting the two criteria, a complete prediction of all possible interactions would in practise be extremely difficult to achieve. Consequently, no account of this is made in the selection procedure presented below.

The selection of appropriate grain refining inoculants was conducted in two stages. Firstly, the disregistry of compounds with austenite was calculated. Secondly, the thermodynamic stability in molten steel of those exhibiting a low mismatch was examined.

The compounds investigated were a series of borides, carbides, nitrides and oxides of B, Al, Si and the elements in transition metal groups IV, V and VI, with the exception of Cr, compounds of which are known to be undesirable in austenitic steels (Clark and Brown, 1973; Clark *et al.* 1973; Greenwood, 1973; Rochow, 1973; Rollinson, 1973; Wade and Banister, 1973). The majority of these compounds have not previously been studied within austenitic stainless steels.

Compounds for investigation had to fulfil two initial stipulations. As solid crystal particles are required to act as nucleants, the melting point of had to exceed that of the steel (AISI 308S92 : T_m=1440 °C from Fig. 2.8). The compounds were also required to have cubic or hexagonal crystal structures at the steel melt temperature where nucleation must occur. The limitation on crystal system was imposed as cubic and hexagonal symmetries are closest to that of austenite, and hence more likely to give the required lattice match. The compounds investigated are listed in Table 4.1.

Table 4.1 - Compounds for which disregistry and solubility calculations were performed with respect to austenitic stainless steels.

Element	Boride	Carbide	Nitride	Oxide
B	—	B_4C	BN	B_2O_3
Al	AlB_2	Al_4C	AlN	Al_2O_3 [a]
Si	—	SiC	Si_3N_4 [b]	SiO_2 [c]
Ti	TiB_2	TiC	TiN	—
Zr	ZrB_2	ZrC	ZrN	ZrO_2 [d]
Hf	HfB_2	HfC	HfN	HfO_2 [d]
V	VB_2	VC	VN	—
Nb	NbB_2	NbC	NbN	—
Ta	TaB_2	TaC	TaN	—
Mo	—	Mo_2C	Mo_2N	—
W	—	WC	W_2N	—

a) α-Al_2O_3. Other forms of alumina, e.g. $\gamma, \theta, \eta, \chi$ etc. are hydrated phases which revert to the anhydrous α form upon heating above 1100 °C (Cawley and Lee, 1994).

b) β-Si_3N_4. Commercial Si_3N_4 is supplied as a mixture of α and β. α is a defect structure which transforms irreversibly to β on annealing above 1400 °C (Hampshire, 1994).

c) On heating SiO_2 follows the transformation sequence α-quartz→ β-quartz→ β-tridymite→ β-cristobalite. At the steel melt temperature, SiO_2 exists as β-cristobalite which has a cubic structure (Bragg and Claringbull, 1965).

d) Pure ZrO_2 and HfO_2 both follow the structural transformation sequence monoclinic→tetragonal→cubic when heated (Cawley and Lee, 1994). At the steel melt temperature pure ZrO_2 would have a tetragonal structure and pure HfO_2 would be monoclinic. However, it has long been established that the cubic structure of ZrO_2 can be stabilised throughout the solid state by the addition of Y_2O_3 (Scott, 1975), and the same effect has recently been reported for HfO_2 (Lakhlifi et al. 1995). Cubic forms of both compounds are now commercially available.

4.2 - Disregistry calculations

4.2.1 - Introduction

The disregistry between austenite and each compound in Table 4.1 was calculated for low index orientation relationships. Where planes of similar atomic arrangement were involved, the basic

disregistry equation (3.14) was used. Conversely, if atomic arrangements were dissimilar, the modified planar disregistry equation (3.15) was employed. Throughout the discussion presented below, the terminology is defined as follows: δ=disregistry in %, a=lattice parameter, and the subscripts m and s refer to the substrate and nucleating solid, *i.e.* austenite, respectively. The necessary lattice parameters for austenite and each compound were obtained from the JCPDS Metals and Alloys Data Book (Weissmann *et al.* 1978).

4.2.2 - Matching cubic substrates to fcc austenite

For fcc substrates, disregistries with austenite were calculated for two orientation relationships, both of which only required use of the basic disregistry equation. The second case differs from the first in that a 45° rotation about the parallel [100] axes is made, which is accounted for by the introduction of a $\sqrt{2}$ term. Thus for $(100)_m \parallel (100)_s$, $[001]_m \parallel [001]_s$

$$\delta = \frac{|a_m - a_s|}{a_s} \times 100 \tag{4.1}$$

and for $(100)_m \parallel (100)_s$, $[011]_m \parallel [001]_s$

$$\delta = \frac{|(a_m/\sqrt{2}) - a_s|}{a_s} \times 100 \tag{4.2}$$

For bcc substrates, disregistries were calculated for the two orientation relationships stated above, and a third whereby the close-packed planes and directions of the substrate and solid were parallel, *i.e.* $(110)_m \parallel (111)_s$, $[\bar{1}10]_m \parallel [\bar{1}10]_s$. Fig. 4.1 shows a diagram of this interface illustrating a dissimilarity in atomic arrangements. Consequently the lattice mismatch for this orientation relationship was calculated using the planar disregistry equation (3.15).

The interatomic spacings $d[uvw]$ required by the planar disregistry equation were determined from lattice parameters using formulae derived by inspection of numerous directions on (100) and (110) projections of fcc and bcc lattices. In fcc crystals, if $u+v+w$ is odd then

$$d[uvw] = a\sqrt{u^2 + v^2 + w^2} \tag{4.3}$$

If $u+v+w$ is even then

$$d[uvw] = \frac{a\sqrt{u^2 + v^2 + w^2}}{2} \tag{4.4}$$

In bcc crystals, if u,v and w are all odd or all even, Equation 4.4 applies, whereas if u,v and w are mixed odd and even, Equation 4.3 is valid.

Fig. 4.1 - Lattice matching between bcc (110) and fcc (111) planes.

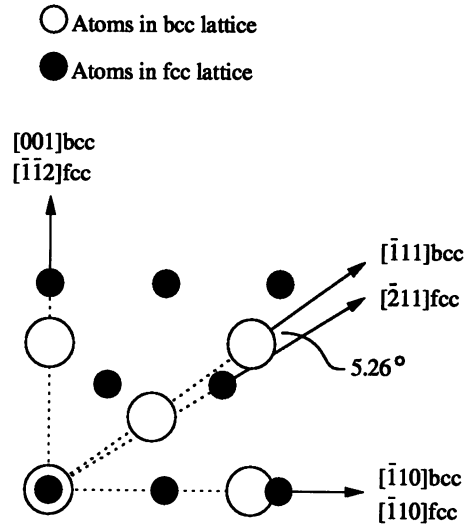

Fig. 4.2 - Lattice matching between hexagonal (0001) plane and (a) fcc (100) plane and (b) fcc (110) plane.

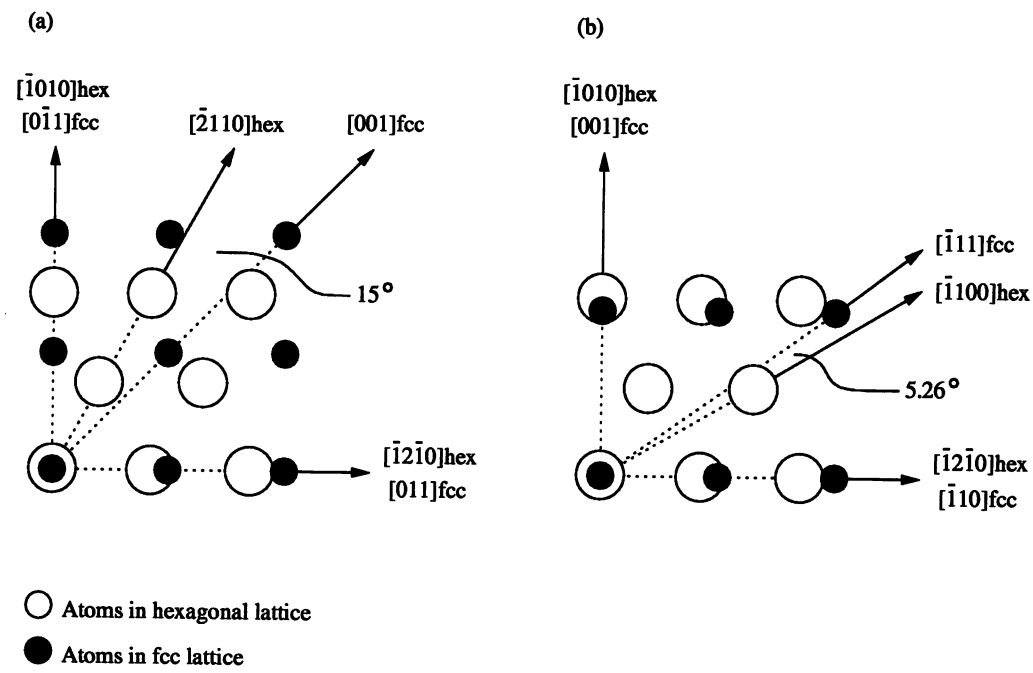

4.2.3 - Matching hexagonal substrates to fcc austenite

For hexagonal substrates, disregistries were calculated for three orientation relationships involving the close-packed (0001) substrate plane. The basic disregistry equation was sufficient for $(0001)_m \parallel (111)_s$, $[\bar{1}2\bar{1}0]_m \parallel [\bar{1}10]_s$ such that

$$\delta = \frac{|a_m - d[\bar{1}10]_s|}{d[\bar{1}10]_s} \times 100 = \frac{|a_m\sqrt{2} - a_s|}{a_s} \times 100 \qquad (4.5)$$

The two remaining orientation relationships shown in Fig. 4.2 involve dissimilar atomic arrangements, hence require use of the planar disregistry equation (3.15). Interatomic spacings within the (0001) hexagonal plane are a along $< 11\bar{2}0 >$ directions and $a\sqrt{3}$ along $< 10\bar{1}0 >$ directions.

4.2.4 - Examples of disregistry calculations

The following cases illustrate calculations using basic and planar disregistry equations. It should be noted from the second example that interatomic spacings were sometimes given as multiples, *i.e.* if only every second nucleus atom in a direction $[uvw]_s$ coincided with a substrate atom, then $2d[uvw]_s$ was used in the calculation (Ostrowski and Langer, 1979b).

i) Substrate and nucleating solid have similar atomic arrangements

Disregistry between NbC and austenite for the orientation relationship $(100)_{NbC} \parallel (100)_\gamma$, $[011]_{NbC} \parallel [001]_\gamma$.

Austenite (γ) : fcc, a=3.60 Å
NbC : fcc, a=4.47 Å

From Equation 4.2, $\delta = (\frac{|(4.47/\sqrt{2}) - 3.60|}{3.60}) \times 100 = 12.2\%$

ii) Substrate and nucleating solid have dissimilar atomic arrangements

Disregistry between HfB_2 and austenite for the orientation relationship $(0001)_{HfB_2} \parallel (100)_\gamma$, $[\bar{1}2\bar{1}0]_{HfB_2} \parallel [011]_\gamma$. The required data are summarised in Table 4.2.

Austenite (γ) : fcc, a=3.600 Å
HfB_2 : hexagonal, a=3.143 Å, c=3.476 Å

From Equation 3.14, $\delta = (\frac{|3.413 - 2.546|}{2.546} + \frac{|3.036 - 3.600|}{3.600} + \frac{|5.444 - 5.092|}{5.092}) \times \frac{100}{3} = 15.3\%$

Table 4.2 - Data for substitution into Equation 3.15.

$[uvw]_{HfB_2}$	$[uvw]_\gamma$	$d[uvw]_{HfB_2}$(Å)	$d[uvw]_\gamma$(Å)	θ(°)	$d[uvw]_{HfB_2}\cos\theta$(Å)
$[\bar{1}2\bar{1}0]$	[011]	3.143	2.546	0	3.143
$[\bar{2}110]$	[001]	3.143	3.600	15	3.036
$[\bar{1}010]$	$[0\bar{1}1]$	5.444	$\frac{2.546\times2}{=5.092}$	0	5.444

4.2.5 - Results of disregistry calculations

Compounds exhibiting disregistries with austenite of less than 10% were deemed to have satisfied the lattice matching criterion necessary for a potent nucleant. This was the case for eight of the compounds from Table 4.1. These compounds, their lowest disregistry with austenite, and the corresponding orientation relationship are given in Table 4.3.

Table 4.3 - Compounds exhibiting low disregistries with austenite.

Compound	Lattice type	Disregistry (%)	Orientation relationship
HfC	fcc	8.84	$(100)_m \parallel (100)_s$, $[011]_m \parallel [001]_s$
BN	hex	1.63	$(0001)_m \parallel (111)_s$, $[\bar{1}2\bar{1}0]_m \parallel [\bar{1}10]_s$
β-Si_3N_4	hex	0.45	$(0001)_m \parallel (111)_s$, $[\bar{1}2\bar{1}0]_m \parallel [\bar{1}10]_s$
TaN	hex	1.96	$(0001)_m \parallel (111)_s$, $[\bar{1}2\bar{1}0]_m \parallel [\bar{1}10]_s$
α-Al_2O_3	hex	6.54	$(0001)_m \parallel (111)_s$, $[\bar{1}2\bar{1}0]_m \parallel [\bar{1}10]_s$
Cubic-HfO_2	fcc	0.37	$(100)_m \parallel (100)_s$, $[011]_m \parallel [001]_s$
SiO_2 (β-cristobalite)	fcc	0.97	$(100)_m \parallel (100)_s$, $[001]_m \parallel [001]_s$
Cubic-ZrO_2	fcc	0.02	$(100)_m \parallel (100)_s$, $[011]_m \parallel [001]_s$

4.3 - Solubility calculations

4.3.1 - The solubility product

The thermodynamic stability of a compound within liquid steel can be described by a temperature dependent equilibrium solubility product (Gladman, 1997). When a compound MX, where M is a metal and X is an interstitial, becomes unstable in liquid steel at a temperature, T, it dissolves and goes into solution such that

$$MX_{\text{solid}} + Fe_{\text{liquid}} \rightleftharpoons (Fe, M, X)_{\text{solution}} \tag{4.6}$$

The compound thus breaks down according to the reaction

$$MX \rightleftharpoons M + X \tag{4.7}$$

x_M and x_X represent the concentrations of M and X dissolved in the liquid steel. The equilibrium constant for the reaction is thus

$$k = \frac{a_M \cdot a_X}{a_{MX}} \tag{4.8}$$

where a_M, a_X and a_{MX} are the activities of the three species. The equilibrium constant, k, is referred to as the solubility product. a_M and a_X can be expressed in terms of the elemental concentrations and activity coefficients, γ, to give

$$a_M = \gamma_M x_M \quad \text{and} \quad a_X = \gamma_X x_X \tag{4.9}$$

If it is assumed that the activity coefficients γ_M and γ_X are equal to unity (Atkins, 1994), and given that the activity of the pure compound MX is also unity, Equation 4.8 becomes

$$k = x_M x_X \tag{4.10}$$

The convention within ferrous metallurgy is to express x_M and x_X as weight percentages. This is acceptable for the majority of situations in which such solubility products are used, namely the field of microalloyed steels, whereby x_M is very low and MX compounds subject to comparison (*e.g.* Ti, V, Nb carbides and nitrides) have similar molecular weights. In this study, however, species with widely differing molecular weights (*e.g.* BN=24.8, HfO_2=210.5) present in higher concentrations had to be compared, thus x_M and x_X were expressed as atomic percentages.

The temperature dependence of the solubility product can be described by an Arrhenius relationship

$$\ln k = -(Q/RT) + c \tag{4.11}$$

$$\text{or} \quad \log_{10} k = -(Q/2.303RT) + c/2.303 \tag{4.12}$$

where Q is the heat of dissolution of MX, R is the gas constant and c is a constant. Equations of this form are usually condensed to

$$\log k = -A/T + B \tag{4.13}$$

where A and B are constants for a given system.

From such equations it is possible to construct the boundary between the liquid single phase region and the liquid+MX two phase region for the ternary system Fe-M-X over a range of temperatures. Fig. 4.3 shows that as the temperature increases within a given system, MX has a higher tendency to dissolve. Two hypothetical compounds are compared in Fig. 4.4, with $MX1$ less soluble in liquid steel than $MX2$.

4.3.2 - Calculation of solubility products

The solubility product in liquid steel was not available for many of the compounds investigated. Solubility products for MX compounds in liquid alloys can be determined from sets of isothermal experiments in which the relative amounts of dissolved M and X and precipitated MX are measured (Morita and Kunisada, 1978; Sumito *et al.* 1981). Such methods are difficult and time consuming to perform.

Alternatively, thermodynamic calculations of the solubility product can be made. The existence of programs such as MTDATA capable of interpreting thermochemical data greatly simplifies this task (Section 2.3.1). MTDATA also offers a further advantage. "By hand" calculations are generally limited to Fe-M-X ternary systems (Inoue *et al.* 1998). The solubility of species in heavily alloyed steels, *e.g.* austenitic stainless, can be significantly different. For example, the solubility limit of nitrogen in pure iron melted under atmospheric pressure is only 0.04 at%. Alloying with 18 wt% Cr and 18 wt% Mn increases this to 0.6 at% N (Stein and Menzel, 1995). MTDATA can account for such effects in multi-component systems.

The temperature dependent equilibrium solubility products in liquid austenitic stainless steel for the eight compounds satisfying the low disregistry criterion (Table 4.3) were thus estimated from MTDATA outputs via the following method, which uses TaN as an example:

Stage 1: The austenitic character of the steel was accounted for by calculating TaN solubility in a (Fe-20 Cr-10 Ni at%)-Ta-N pseudo-ternary system. Liquid and TaN phases were allowed to coexist.

Stage 2: To act as nucleants, the compounds need to be stable within the liquid ahead of the solidifying interface. Solubility was thus determined over the temperature range 1900–1750 K using 1 K intervals.

Fig. 4.3 - Temperature dependence of the liquid/liquid+MX phase boundary for the ternary system Fe-M-X.

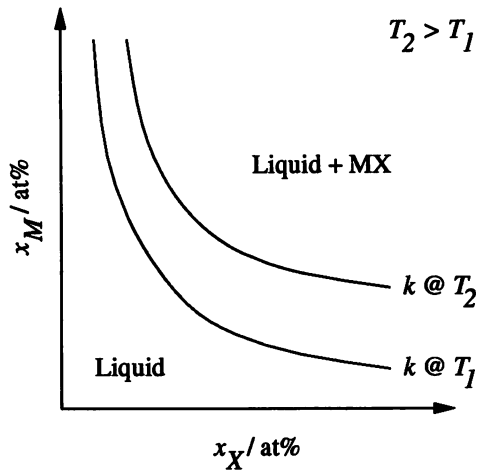

Fig. 4.4 - Relative thermodynamic stabilities of two different compounds at a temperature T. (a) $MX1$ is less soluble than (b) $MX2$.

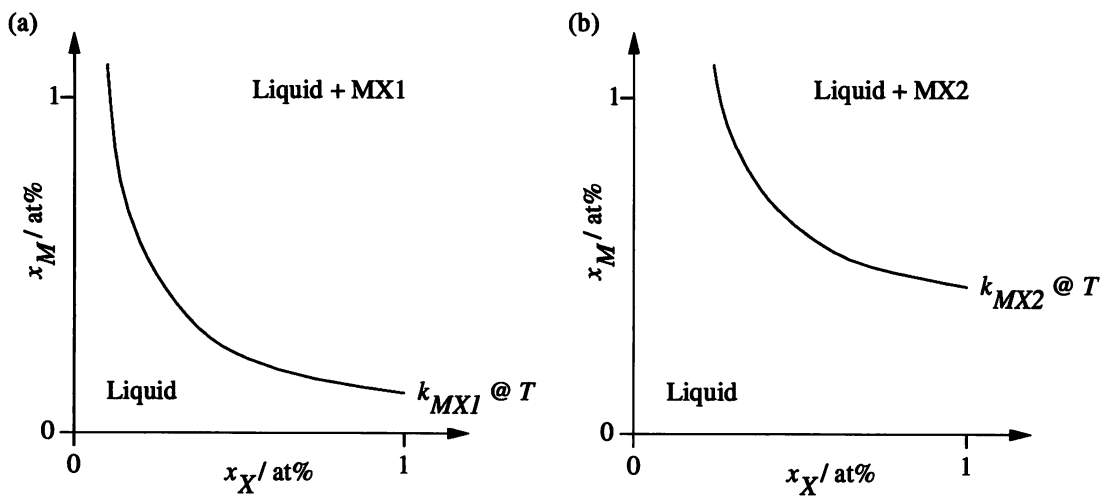

Stage 3: Ta and N concentrations were systematically adjusted such that TaN first formed at some point between 1800–1750 K. The compositional inputs and corresponding MTDATA outputs are shown in Tables 4.4 and 4.5. The liquid/liquid+TaN phase boundary for steel of this composition occurred at 1792 K whereby $k=x_{\mathrm{Ta}}x_{\mathrm{N}}$=[0.3][0.3]=0.09 (Fig. 4.5).

Table 4.4 - Steel compositions from Stages 3 and 4 in at%.

	Fe	Cr	Ni	Ta	N
Stage 3:	to bal.	20	10	0.3	0.3
Stage 4:	to bal.	20	10	0.4	0.4

Stage 4: Ta and N concentrations were increased such that TaN first formed within the higher temperature range 1900–1850 K. The subsequent compositional inputs and MTDATA outputs are given in Tables 4.4 and 4.5. The liquid/liquid+TaN phase boundary for steel of this composition occurred at 1877 K whereby k=0.16 (Fig. 4.5).

Table 4.5 - Segments of MTDATA output from Stages 3 and 4 at the liquid/liquid+TaN phase boundary.

	Temp/K	Liquid/mol%	TaN/mol%
Stage 3:	1794	100	0
	1793	100	0
	1792	99.9998	1.96E-4
	1791	99.9996	3.87E-4
Stage 4:	1879	100	0
	1878	100	0
	1877	99.9999	8.43E-5
	1876	99.9997	3.20E-4

Stage 5: The gradient and intercept from a linear plot of $\log k$ vs. $1/T$ using data from Stages 3 and 4 gave the constants A and B required by Equation 4.13. Thus the temperature dependent equilibrium solubility product in at% of TaN in liquid austenitic stainless steel over the temperature range 1900–1750 K was found to be:

$$\log k = (-9939/T) + 4.5 \tag{4.14}$$

Fig. 4.5 - MTDATA calculated liquid/liquid+TaN phase boundaries for (Fe-20 Cr-10 Ni at%)-Ta-N as a function of temperature.

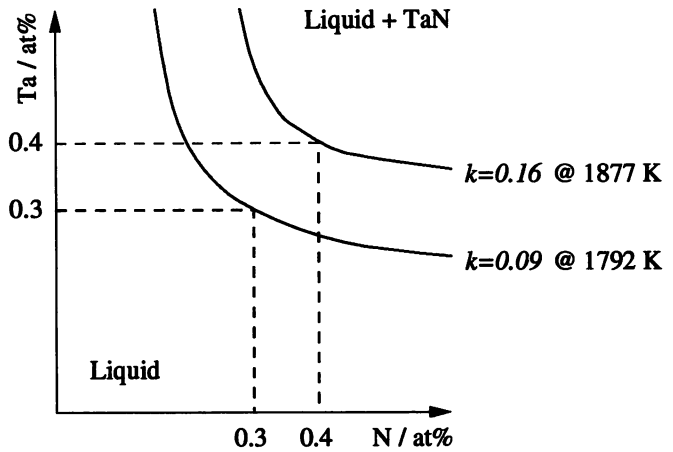

Fig. 4.6 - Solubility products in at% of BN, HfC, Si_3N_4 and TaN in molten austenitic stainless steel as a function of temperature, compared with that of TiN.

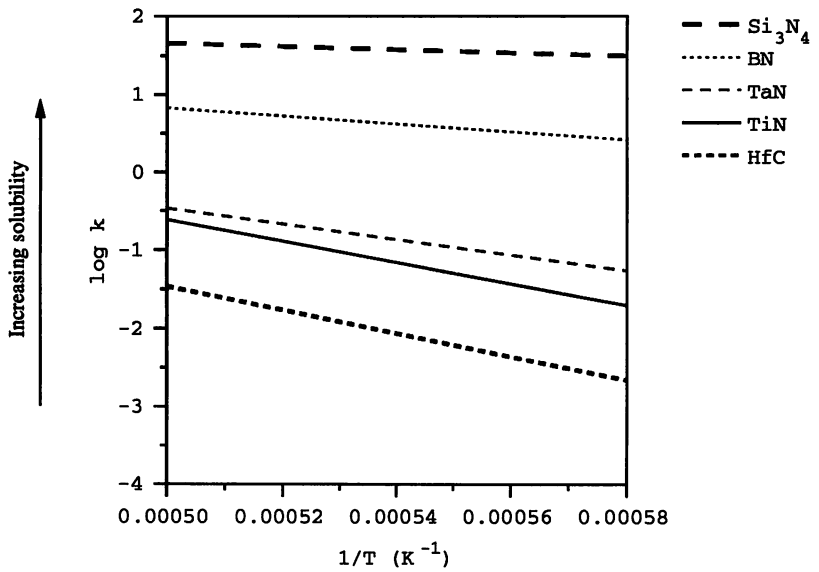

To gauge the relative thermodynamic stabilities of the compounds, solubility products were compared with that of TiN (calculated via the same method), known from the literature (Section 3.3.6) to exhibit low solubility in molten stainless steel.

However, it must be remembered that MTDATA calculations deal only with thermodynamics. For example, whilst particles added to a molten alloy may be thermodynamically unstable, if the liquid solidifies rapidly, *e.g.* weld pool solidification, there may be insufficient time for complete dissolution to occur, in which case they may be able to act as nucleants.

4.3.3 - Results of solubility calculations

The four oxides from Table 4.3 were found to be insoluble over the temperature range 1900–1750 K, hence solubility products were immaterial. The temperature dependent equilibrium solubility products in liquid austenitic stainless steel for the four other compounds are listed in Table 4.6, along with the benchmark value for TiN. A graphical representation illustrates more clearly the relative thermodynamic stabilities of these compounds (Fig. 4.6). BN and Si_3N_4 are thus shown to have high solubilities, whereas HfC and TaN have low solubilities comparable with that of TiN.

Table 4.6 - MTDATA calculated solubility products in at%.

Compound	Solubility
BN	$\log k = (-5142/T) + 3.4$
HfC	$\log k = (-14929/T) + 6.0$
Si_3N_4	$\log k = (-2079/T) + 2.7$
TaN	$\log k = (-9939/T) + 4.5$
TiN	$\log k = (-13630/T) + 6.2$

4.4 - Summary

Of the 34 compounds initially selected for investigation with respect to austenitic stainless steels (Table 4.1), eight satisfied the lattice matching criterion, *i.e.* disregistry with austenite of less than 10% (Table 4.3). Of these, six also fulfilled the low solubility requirement: α-Al_2O_3, cubic-HfO_2, SiO_2 (β-cristobalite), cubic-ZrO_2, HfC and TaN. Hence these compounds were predicted to be potent nucleants for austenite, theoretically capable of producing grain refinement upon addition to austenitic stainless steel welds.

BN and Si_3N_4, whilst exhibiting low disregistries with austenite, are highly soluble. Excessive additions would be required for any chance of successful refinement, which would be likely to have detrimental effects on weld properties. For example, for inoculant BN particles to remain stable in the liquid at 1750K, an addition equivalent to 0.35wt% B is required, the majority of which would be dissolved in the steel. Such levels of B would probably prove disastrous in terms of weld cracking, the usual B content of austenitic welds being ~0.01wt% in order to avoid this (Table 2.1).

Chapter 5 - Single-pass welds : Part 1

5.1 - Introduction

To achieve the aim of this project it has been deemed necessary to establish a grain refining addition for austenitic stainless steel that can eliminate continuous grain growth between successive deposits in multipass welds. A selection procedure to identify compounds exhibiting low disregistries and solubilities with respect to austenitic stainless steels predicted that α-Al_2O_3, cubic-HfO_2, SiO_2 (β-cristobalite), cubic-ZrO_2, HfC and TaN should be effective nucleants for austenite.

However, to make an initial evaluation of their grain refining potential, single pass welds were inoculated with these compounds and compared with a control specimen. The validity of the selection procedure was further examined by studying the effect of BN and Si_3N_4 inoculants. These two compounds fulfilled the low disregistry criterion, but were calculated to be soluble in liquid steel. They should, therefore, not lead to grain refinement; indeed it is possible that their dissolution may have detrimental effects on weld quality.

The welding experiments presented below—and those in subsequent chapters—were carried out at TWI, Abington, Cambridgeshire.

5.2 - Experimental design

5.2.1 - Inoculant addition

Direct additions were made to welds by mixing inoculant powders with acetone to form a flux which was painted over the plate to be welded. The acetone quickly evaporated leaving a thin covering of inoculant.

The grain refining potencies of different inoculants should strictly be compared with the number and size of added particles kept constant. Unfortunately, this was prevented by the commercial availability of the necessary powdered compounds. The particle size and supplier of each compound is given in Table 5.1.

Table 5.1 - The particle size and supplier of inoculant powders.

Compound	Particle size (μm)	Supplier
HfC	2	Sigma-Aldrich Co. Ltd.
BN	1	Sigma-Aldrich Co. Ltd.
Si_3N_4	10	Sigma-Aldrich Co. Ltd.
TaN	5	Sigma-Aldrich Co. Ltd.
Al_2O_3	1	Alfa-Aesar
HfO_2	1	ABCR-Gelest (UK) Ltd.
SiO_2	10	Sigma-Aldrich Co. Ltd.
ZrO_2	1	Zirconia Sales (UK) Ltd.

Flux of suitable consistency was prepared by mixing $1\,cm^3$ powder in 10 ml acetone. The mass of each compound required was obtained from the room temperature density, ρ_{298K} (Table 5.2). To quantify the level of additions, tests were performed in which each flux was painted over a given area of plate. The powder layer was then scraped off into a petri-dish with a razor edge and weighed. This gave the mass of inoculant powder per unit area of plate covered, m_p. The volume of inoculant powder per unit area of plate covered is thus given by

$$v_p = \frac{m_p}{\rho_{298K}} \tag{5.1}$$

Errors arose as the painting technique and occasional particle agglomerations prevented completely uniform coverage. The statistical error in v_p is given by

$$E^2_{v_p} = \frac{1}{N}\left(\frac{\sigma_{v_p}}{\overline{v}_p}\right)^2 \tag{5.2}$$

where N is the number of measurements, σ_{v_p} is the standard deviation in v_p, and $\overline{v}_p$ is the mean value of v_p. The results, from ten measurements for each compound, are shown in Table 5.2. v_p was approximately the same for each case ($\sim 2 \times 10^{-3}\,cm^3$), thus despite differing particle sizes, comparable additions of each inoculant could be made.

Table 5.2 - Data quantifying the amounts of inoculant additions. $v_p \approx 2 \times 10^{-3}\,\mathrm{cm}^3$ for each case showing that comparable additions could be made. $\overline{m}_p$ is the mean value of m_p (Section 5.3.4).

Compound	ρ_{298K} ($\mathrm{g\,cm^{-3}}$)	$\overline{m}_p$ ($\mathrm{g\,cm^{-2}}$)	v_p ($/10^{-3}\,\mathrm{cm}^3$)
HfC	12.65	0.028	2.2 ± 0.1
BN	2.29	0.004	1.8 ± 0.3
Si_3N_4	3.44	0.008	2.3 ± 0.3
TaN	14.40	0.030	2.0 ± 0.1
Al_2O_3	3.97	0.008	2.0 ± 0.2
HfO_2	10.48	0.020	1.9 ± 0.1
SiO_2	2.65	0.006	2.2 ± 0.3
ZrO_2	6.20	0.012	1.9 ± 0.2

5.2.2 - Weld geometry and operating parameters

Coupons of austenitic stainless steel plate (composition in Table 2.1) were cut to 150 × 100 × 12 mm and machined with a 3 mm radius half-round groove along their length. Flux was painted along the groove, which reduced the chance of inoculant being pushed or blown away from the weld pool. Once the flux had been applied, a mechanised TIG unit was used to complete the weld under the conditions given in Table 5.3 (Fig. 5.1).

Table 5.3 - Welding parameters for initial single pass inoculation experiments.

Current	200 A (d.c. negative)
Voltage	10 V
Weld speed	$100\,\mathrm{mm\,min^{-1}}$
Heat input	$0.72\,\mathrm{kJ\,mm^{-1}}$
Filler wire	308S92 (Table 2.1)
Filler size	1.2 mm (diam.)
Wire feed speed	$0.55\,\mathrm{m\,mm^{-1}}$
Electrode	2% thoriated tungsten
Shielding gas	Argon
Gas flow rate	$12\,\mathrm{l\,min^{-1}}$

Fig. 5.1 - Design of single-pass weld inoculation experiment.

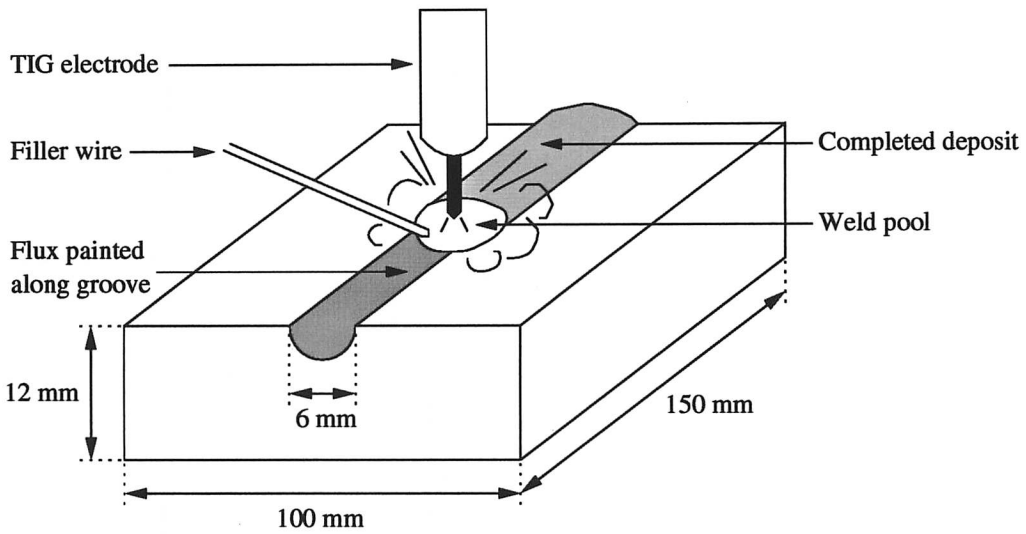

Fig. 5.2 - Sections cut for optical microscopy. (a) Transverse profile, (b) plan view 100 μm below weld surface, (c) plan view 1 mm below weld surface and (d) section along the weld centreline.

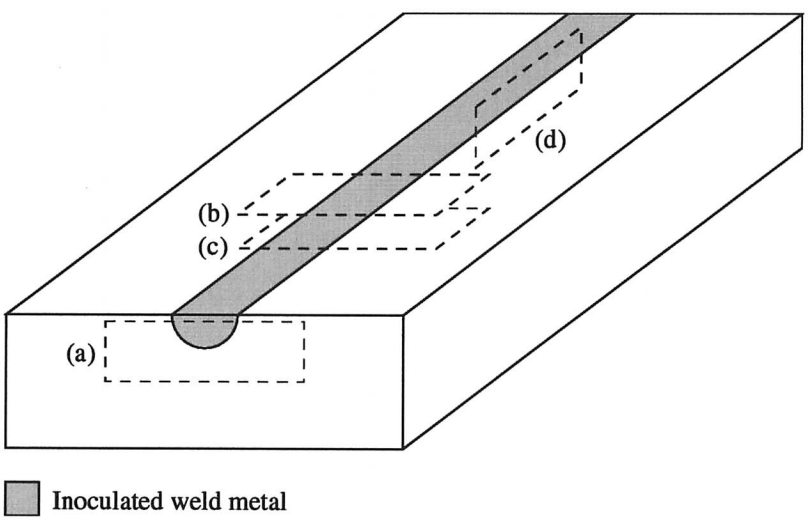

5.3 - Primary analysis techniques

5.3.1 - Optical microscopy

The weld microstructures were characterised by optical microscopy of up to four cross-sections; transverse profile, plan view 100 μm below the weld surface, plan view 1 mm below the weld surface, and section along the weld centreline (Fig. 5.2). Samples were prepared and etched to reveal the austenite grain structure following the methods outlined in Section 2.3.3. The as-welded surface of each weld was also examined.

5.3.2 - Scanning electron microscopy

The presence of inoculant particles and other inclusions within weld deposits was verified by examination of sections in a JEOL 5800LV scanning electron microscope (SEM). Light etching allowed inclusions to be clearly observed in the secondary electron imaging mode. As-welded surfaces were also studied in the SEM. Inclusions and weld surface slag are non-conducting, hence specimens were gold sputtered to prevent charging within the microscope.

5.3.3 - Microanalysis

The chemical compositions of inclusions and weld surface slags, and the concentrations of species dissolved in the steel matrix, were investigated using a NORAN VOYAGER energy dispersive X-ray microanalyser (EDX) attached to the SEM. The system uses a windowless detector which also permits identification of the light elements Be–Ne, which cannot be detected if a beryllium window is present. However, the precise quantification of the concentrations of these elements is prevented by contamination, *e.g.* oxygen and nitrogen from the imperfect vacuum, carbon from organic compounds present as grease or dirt on the specimen, and oxygen from surface oxides on the specimen.

The concentrations of species dissolved within the matrix were determined from measurements at 50 locations, with errors estimated by an expression of the same form as Equation 5.2. The microanalysis equipment, however, was not sensitive enough to detect the very small concentrations of boron, carbon, nitrogen and oxygen. Where this was necessary, specimens were sent to Bodycote Materials Testing Ltd. for analysis by inductively coupled plasma spectroscopy (ICPS). The error quoted for such analyses was $\pm 10\%$ of the measured value.

Fig. 5.3 - Extraction replica preparation. (a) Inclusions in polished specimen, (b) inclusions revealed by light etching and (c) inclusions adhere to carbon film as steel matrix is subjected to further etching.

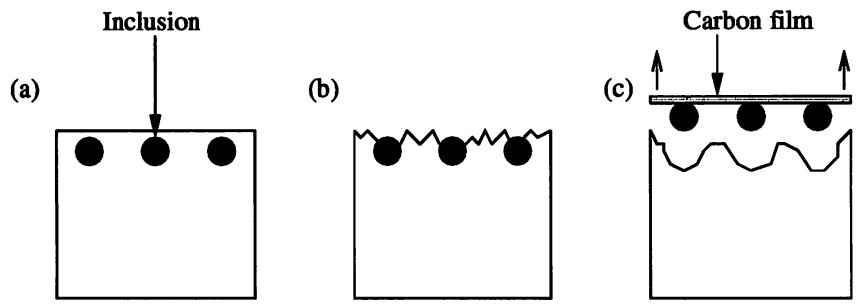

Reliable determination of inclusion compositions was more difficult. The spatial resolution of EDX is about 1 μm. Inclusions are often smaller than this, making overlap of information with the matrix inevitable. Although the resolution can be enhanced by reducing the accelerating voltage and probe spot size, this can lead to insufficient X-ray emissions, particularly from heavier elements.

Instead, inclusions were extracted on carbon replicas. Polished sections of weld metal were lightly etched electrolytically in 10% HCl in methanol at 6 V d.c. This dissolved the steel matrix but not the inclusions. Carbon films were deposited on the specimen surfaces using a vacuum vaporising system. Coated samples were then subjected to further etching. The steel matrix was heavily attacked whilst the inclusions adhered to the carbon film (Fig. 5.3). The replicas were collected on aluminium stubs and gold sputtered prior to viewing in the SEM.

5.3.4 - Estimation of total inoculant addition in wt%

In a number of cases it was necessary to compare the measured concentrations of dissolved species with the total inoculant addition to assess the extent of particle dissolution. For an inoculant MX, the amount added to a weld as a weight percentage is given by

$$x_{MX} = \frac{m_i}{m_w + m_i} \times 100 \tag{5.3}$$

where m_i is the mass of the inoculant, and m_w is the mass of the weld metal. Inoculant flux was painted along the 0.3 cm radius half-round groove of the plate to be welded. The area of plate covered by inoculant in cm^2 is thus

$$A_p = 0.3\pi l \tag{5.4}$$

where l is the length of the plate in cm. Hence

$$m_i = A_p \overline{m}_p = 0.3\pi l \overline{m}_p \tag{5.5}$$

where $\overline{m}_p$ is the average mass of inoculant powder per unit area of plate covered in $g\,cm^{-2}$ (Table 5.2). The mass of the weld metal in grams is given by

$$m_w = 7.8 A_w l \tag{5.6}$$

where 7.8 is the density of the weld metal in $g\,cm^{-3}$, and A_w is the transverse cross-sectional area of the weld metal in cm^2. A_w was measured using a SEESCAN image analyser. Substitution of Equations 5.5 and 5.6 into Equation 5.3 gives

$$x_{MX} = \frac{0.3\pi \overline{m}_p}{7.8 A_w + 0.3\pi \overline{m}_p} \times 100 \tag{5.7}$$

The wt% additions of M and X from the inoculant flux are thus

$$x_M = \frac{x_{MX} Z_M}{Z_{MX}} \quad \text{and} \quad x_X = \frac{x_{MX} Z_X}{Z_{MX}} \tag{5.8}$$

where Z_M, Z_X and Z_{MX} are the relative masses of M, X and MX respectively.

5.4 - Results and discussion

5.4.1 - Control weld

Fig. 5.4 shows four cross-sections of the control weld. The microstructure is wholly columnar, but with the unusual feature of a set of long, almost continuous grains along the weld centreline. These *axial* structures have been previously observed, and their presence attributed to slow welding speeds, whereby the weld pool has an elliptical shape (Ganaha *et al.* 1980; Li and Brooks, 1998). The pool tail thus has a relatively flat surface from which grains can easily grow parallel to the welding direction (Fig. 5.5). The as-welded surface of the control weld was clean and free from slag, allowing the shape of the pool tail to be confirmed (Fig. 5.6).

SEM of the control weld revealed the presence of globular, sub-micron inclusions (Fig. 5.7). EDX investigation of these particles found them to have consistent compositions, rich in Mn and S, with occasional traces of Fe, Cr and O (Table 5.4), indicating that they are most likely to be impure MnS. This result is in agreement with thermodynamic calculations which predict the existence of MnS (Section 2.3.2).

Table 5.4 - Typical measured composition in wt%
of a globular inclusion from the control weld.

Mn	S	Fe	Cr	O
61.4	34.7	1.9	1.4	0.7

5.4.2 - Oxide inoculated welds

The welds inoculated with the oxides α-Al_2O_3, cubic-HfO_2, SiO_2 (β-cristobalite) and cubic-ZrO_2 all exhibited similar characteristics. Transverse profiles and sections along the weld centreline show the microstructure of each weld to be columnar, but with an absence of the axial grains seen in the control weld (Fig. 5.8).

Fig. 5.4 - Microstructure of the control weld. (a) Transverse profile, (b) plan view 100 μm below weld surface, (c) plan view 1 mm below weld surface and (d) section along the weld centreline.

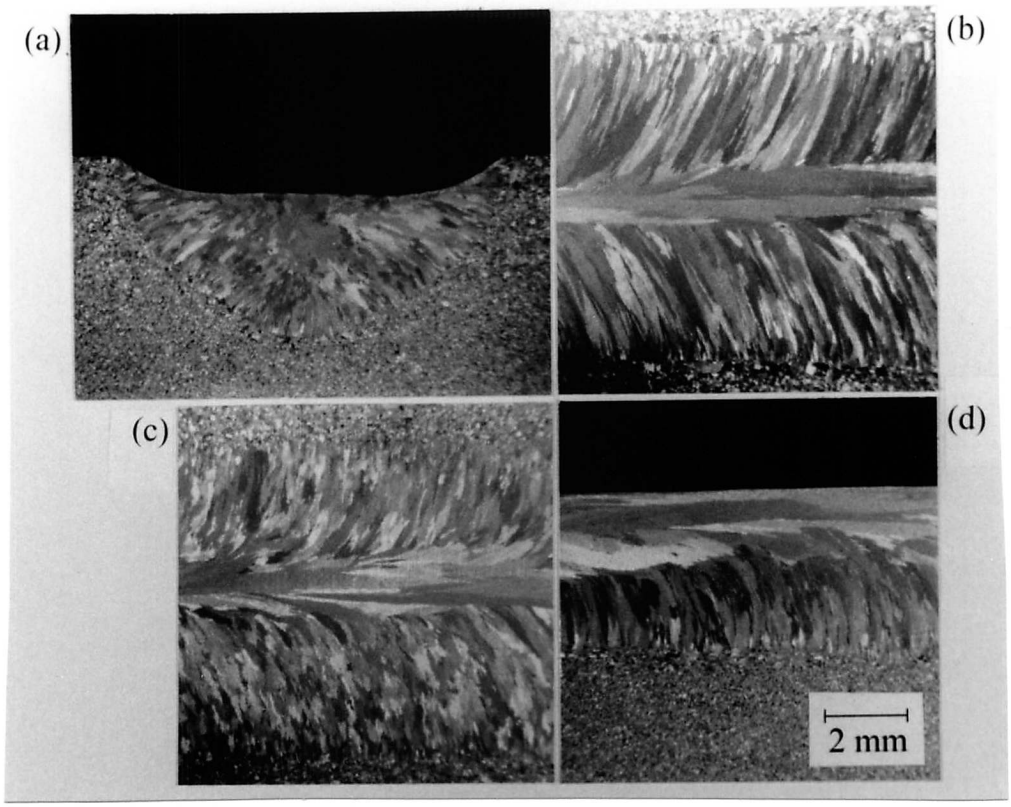

Fig. 5.5 - Comparison of microstructures resulting from high and low welding speeds. (a) At low welding speeds the weld pool is elliptical and axial grains can grow from the pool tail. (b) The teardrop shaped weld pool at high welding speeds prevents axial grain formation.

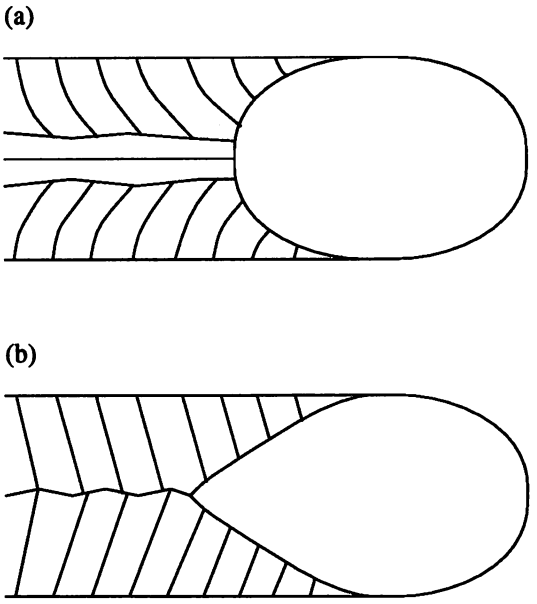

Fig. 5.6 - As-welded surface of the control deposit.

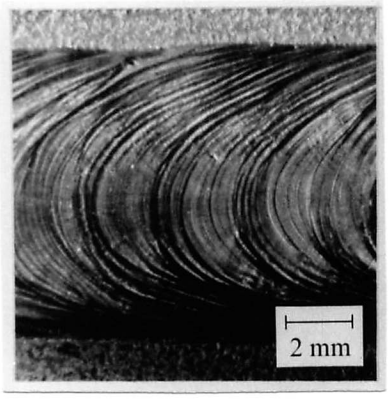

Fig. 5.7 - SEM image of MnS inclusion within the control weld deposit.

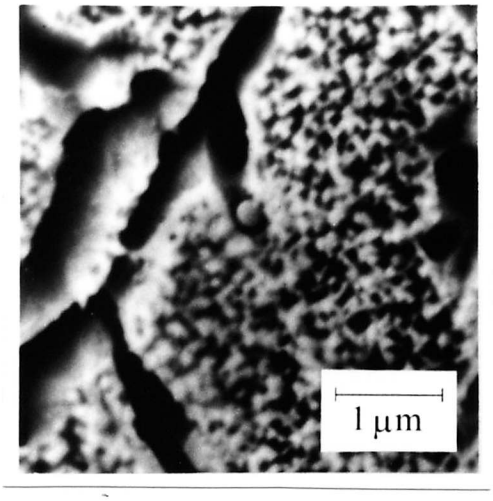

Fig. 5.8 - Microstructures of the oxide inoculated welds. (a–b) α-Al_2O_3, (c–d) cubic-HfO_2, (e–f) SiO_2 (β-cristobalite) and (g–h) cubic-ZrO_2 inoculated. Transverse profiles are on the left and sections along the weld centreline on the right.

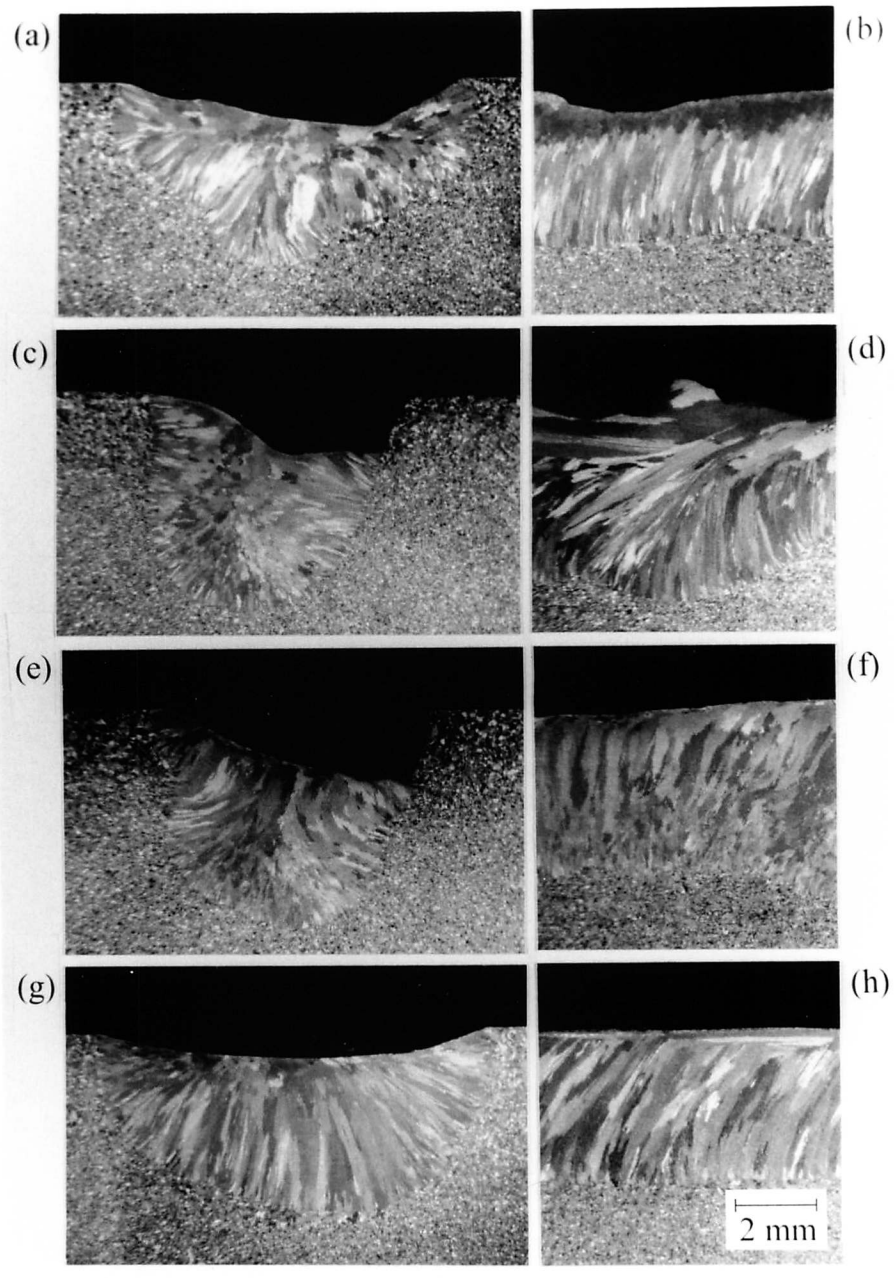

SEM and EDX showed that all of the welds contained globular MnS inclusions identical to those of the control. However, only the cubic-HfO_2 inoculated weld contained inclusions corresponding to the flux addition. Cuboidal particles about $1\,\mu m$ in size composed of Hf, Y, Zr and O (Table 5.5), were observed throughout the weld deposit (Fig. 5.9). Traces of Y within the inclusions arose from the Y_2O_3 additions used to stabilise the cubic allotrope of HfO_2, and unless specially purified, all Hf compounds contain small amounts of Zr (Clark *et al.* 1973).

Table 5.5 - Typical measured composition in wt% of a cuboidal particle within the cubic-HfO_2 inoculated weld.

Hf	Y	Zr	O
81.3	3.5	0.5	14.7

No dissolved Al, Hf or Zr was detected during microanalysis of the steel matrix of α-Al_2O_3, cubic-HfO_2, and cubic-ZrO_2 inoculated welds respectively. The measured Si content of the matrix in the SiO_2 inoculated weld was 0.40 ± 0.03 wt%, which is the standard content of the filler material (Table 2.1). These results verify the insolubility of the four compounds as calculated in Section 4.3.3.

Each oxide inoculated weld was covered with a surface layer of slag (Fig. 5.10). The texture was of a powdery crust for the α-Al_2O_3, cubic-HfO_2, and cubic-ZrO_2 inoculated welds, whereas SiO_2 additions produced a hard, globular slag. The composition of the slag in each case corresponded to the deliberate addition.

The absence of deliberate additions within the oxide inoculated weld deposits, either as inclusions (except cubic-HfO_2) or dissolved species, and the presence of slags correlating to inoculants on deposit surfaces, show that the steel did not wet these oxides.

The lack of wetting suggests that the austenite/oxide interfacial free energies are high. Thus the structural aspect of the interface, *i.e.* the lattice mismatch which was low in each case, is not the controlling factor in defining the energy barrier to nucleation (Section 3.3.3).

Theory proposed by Tiller and Takahashi (1969) suggests an additional contribution to interfacial free energy which explains the inability of steel to wet the oxides in question. If two different materials are brought together to form an interface, the initial electrochemical potential of each is different. Therefore charge must flow into the regions either side of the interface to balance this, creating charged electrostatic layers.

Fig. 5.9 - SEM image of a cuboidal inclusion within the cubic-HfO_2 inoculated weld. Microanalysis showed it to correspond to the deliberate addition.

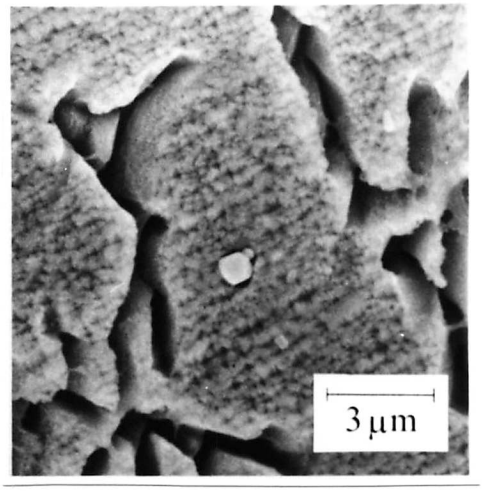

Fig. 5.10 - As-welded surfaces of (a) α-Al_2O_3, (b) cubic-HfO_2, (c) SiO_2 (β-cristobalite) and (d) cubic-ZrO_2 inoculated deposits.

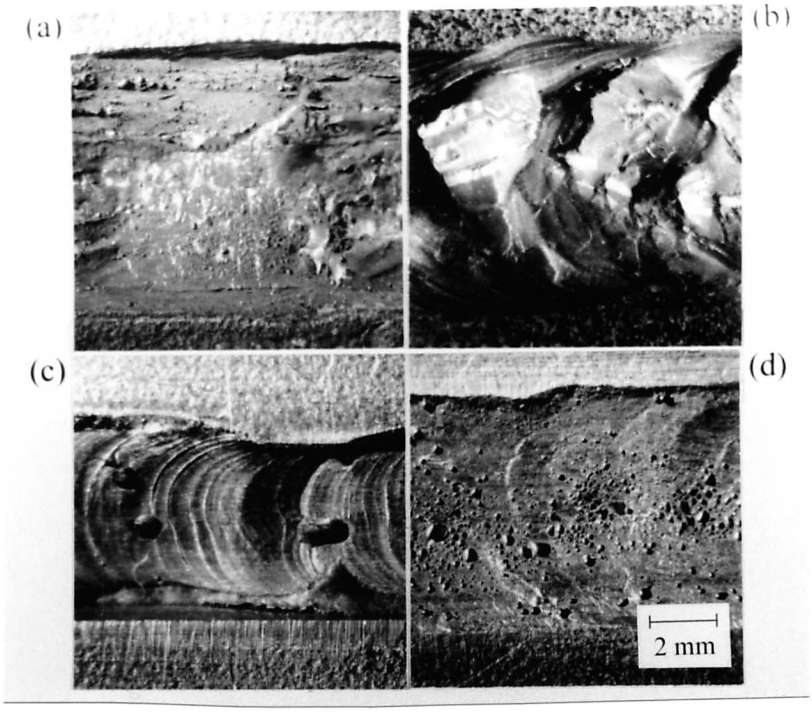

The solid/substrate interfacial free energy, γ_{SM}, can thus be partitioned into structural, γ_{st}, and electrostatic, γ_{el}, components:

$$\gamma_{SM} = \gamma_{st} + \gamma_{el} \tag{5.9}$$

γ_{st} is always positive and refers to the increase in free energy from strain/dislocations at the interface as a result of lattice mismatch. γ_{el} is always negative and refers to the reduction in free energy due to the redistribution of charge at the interface.

The oxides Al_2O_3, HfO_2, SiO_2 and ZrO_2 are all excellent insulators, with electrical resistivities in the order of 10^7–10^8 ohm cm at the steel solidification temperature (Ryshkewitch, 1960; Brook, 1991). Because of this, charge cannot easily flow across the austenite/oxide interface. The magnitude of γ_{el} is thus very small, hence γ_{SM} is not favourably reduced. Therefore despite the oxides' close lattice matching with austenite, the energy barrier to nucleation remains high. Consequently the oxide inoculants could not act as nucleation sites and the weld microstructures remained columnar and unrefined.

However, the use of oxide flux did alter the solidification structure by eliminating axial grains. Therefore the flux must have affected the shape or stability of the weld pool tail from which axial grains would otherwise grow.

The cubic-HfO_2 inoculated weld was anomalous in that it contained inclusions pertaining to the deliberate addition. The cross-section along the weld centreline (Fig. 5.8d) and the as-welded surface (Fig. 5.10b) show the deposit to be very uneven. This indicated that cubic-HfO_2 flux destabilised the welding arc and thus severely disturbed the weld pool. The ensuing agitation most likely led to the entrapment of some cubic-HfO_2 particles within the deposit. However, no explanation for the exclusiveness of this effect to cubic-HfO_2 flux can be made from these experiments.

The anomalous appearance of the slag on the SiO_2 inoculated weld can be explained by a more detailed consideration of silica chemistry (Rochow, 1973). At the steel melt temperature, the equilibrium form of SiO_2 is β-cristobalite. This allotrope is fcc and exhibits a low disregistry with austenite of 0.97%, hence its selection as a potentially effective nucleant. However, the phase transformation to β-cristobalite is sluggish, and if SiO_2 is heated rapidly, it melts as β-quartz at around 1550°C. On rapid cooling liquid SiO_2 solidifies to a vitreous mass. The thermal conditions during welding were conducive to this, hence glassy SiO_2 weld slag was formed (Fig. 5.10c).

5.4.3 - BN inoculated weld

Fig. 5.11 shows four cross-sections of the BN inoculated weld. The microstructure is columnar and unrefined, although the extent of the axial character is greatly reduced compared with the control weld. The most significant feature, though, is the cracking along the weld centreline, which can be seen from the as-welded surface, which was clean and free from slag (Fig. 5.12). Higher magnification microscopy of an etched specimen shows the cracks to be inter-dendritic (Fig. 5.13).

The only inclusions detected by SEM and EDX were globular MnS, as common to all the welds examined thus far. The measured concentrations of dissolved B and N were 0.09 ± 0.01 wt% and 0.11 ± 0.01 wt% respectively.

Using the method from Section 5.3.4, the additions from the inoculant flux were estimated to be 0.08 wt% B and 0.11 wt% N. The weld metal also inherently contains 0.0009 wt% B and 0.02 wt% N (Table 2.1), giving a theoretical total composition of 0.0809 wt% B and 0.13 wt% N if all B and N is in solution.

Allowing for errors in flux coverage and the ICPS technique, the measured concentrations of B and N are thus consistent with complete dissolution of the BN inoculant within the steel. Substitution of the measured concentrations (equivalent to 0.45 at% B and 0.44 at% N) into the temperature dependent solubility product equation for BN in liquid steel (Table 4.6) confirms that with this level of addition, BN particles should not be stable in the melt. The B content of the weld pool was thus $\sim$ 90 times higher than that of the control weld. Such concentrations inevitably lead to solidification cracking, as was observed.

The experiment thus verifies the predictions made in Chapter 4; complete dissolution of BN, the consequent absence of nucleation sites and hence lack of grain refinement, and detrimental effects on weld quality as a result of dissolved species.

Fig. 5.11 - Microstructure of the BN inoculated weld. (a) Transverse profile, (b) plan view 100 μm below weld surface, (c) plan view 1 mm below weld surface and (d) section along the weld centreline.

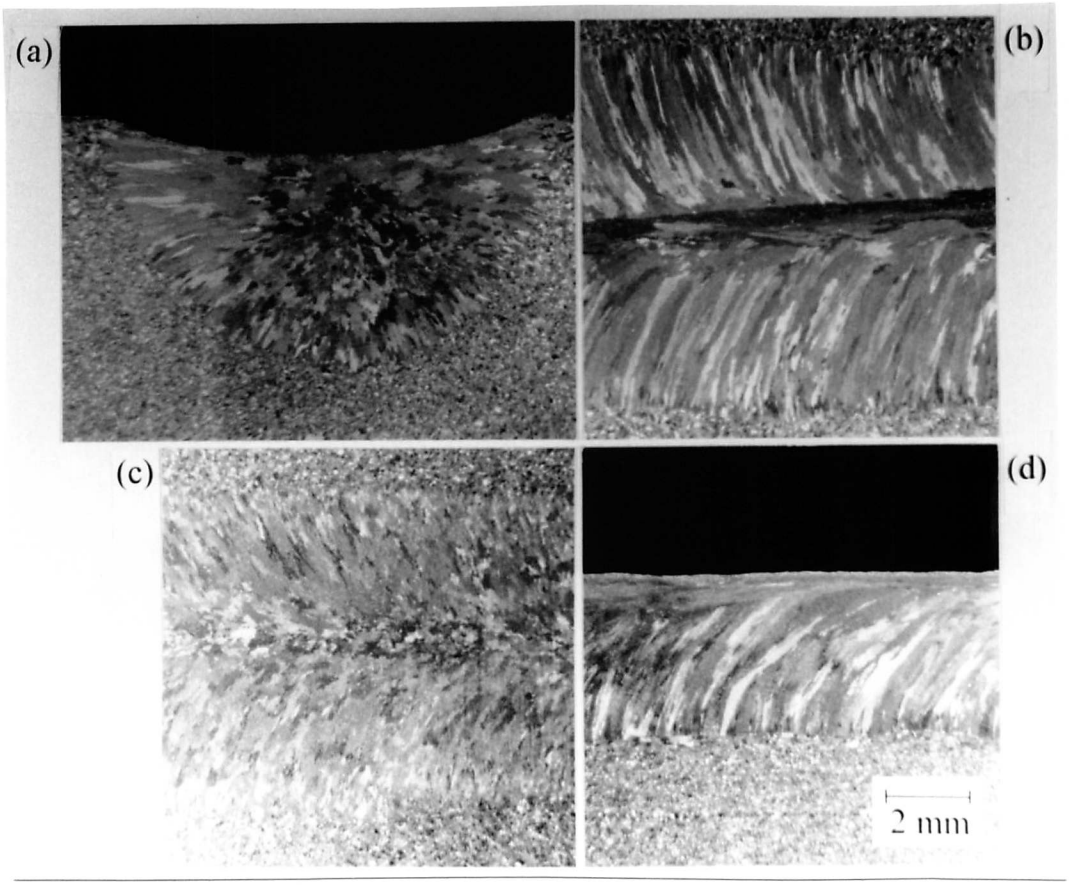

Fig. 5.12 - As-welded surface of the BN inoculated deposit.

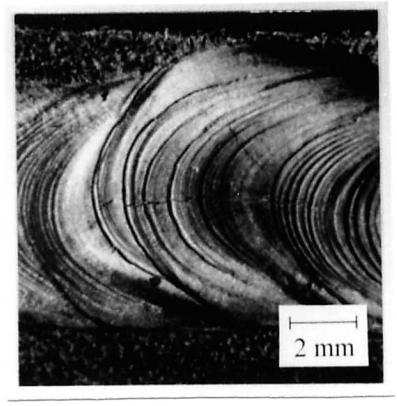

Fig. 5.13 - Magnified view of crack in the BN inoculated weld.

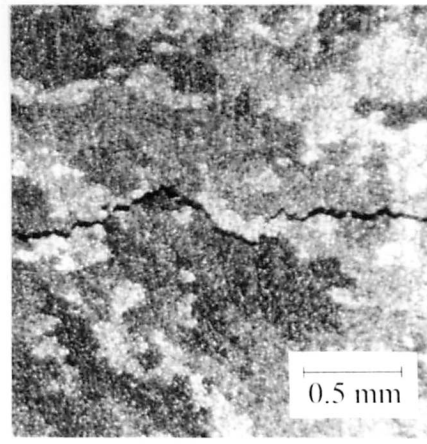

5.4.4 - Si_3N_4 inoculated weld

The four cross-sections of the Si_3N_4 inoculated weld show an equiaxed microstructure indicative of extensive grain refinement (Fig. 5.14). The as-welded surface was clean, even, free from slag and displayed an elliptical pool tail shape (Fig. 5.15). Therefore the absence of a columnar axial structure was not a result of Si_3N_4 flux disrupting the shape or stability of the weld pool tail.

However, comparison of the transverse profiles of the control and Si_3N_4 inoculated welds show an increase in the depth-to-width ratio as a result of the flux addition (Figs. 5.4a and 5.14a). Whilst it is generally assumed that extreme changes in weld pool shape are required to promote spontaneous columnar-to-equiaxed transitions (Davies and Garland, 1975), nevertheless an experiment was performed to verify that this was not occurring here.

A further weld was made using identical conditions (Table 5.3), but with an activating flux applied (Table 5.6), a method better known as A-TIG welding (Lucas and Howse, 1996; Paskell *et al.* 1997). Activating fluxes increase weld penetration, but are not incorporated into the deposit (Section 6.2).

Table 5.6 - Composition of the activating flux.

Compound	Proportion
Titania (TiO_2)	70%
Titanium powder (Ti)	15%
Chromium (III) oxide (Cr_2O_3)	10%
Sodium fluoride (NaF)	5%

The transverse profile of the A-TIG weld shows enhanced penetration, and hence a similar shape to the Si_3N_4 inoculated deposit (Fig. 5.16a). Further cross-sections confirm that the A-TIG weld microstructure remained entirely columnar with an axial character akin to the control (Fig. 5.16b–d). Thus a change in weld pool shape could not have caused the observed refinement.

It was therefore postulated that Si_3N_4 inoculant particles must have acted as nucleants, despite thermodynamic calculations which predict the compound to be extremely soluble (Section 4.3.3). SEM and EDX analyses were performed to search for such inclusions. However, extensive study of lightly etched cross-sections revealed only MnS inclusions.

Fig. 5.14 - Microstructure of the Si_3N_4 inoculated weld. (a) Transverse profile, (b) plan view 100 μm below weld surface, (c) plan view 1 mm below weld surface and (d) section along the weld centreline.

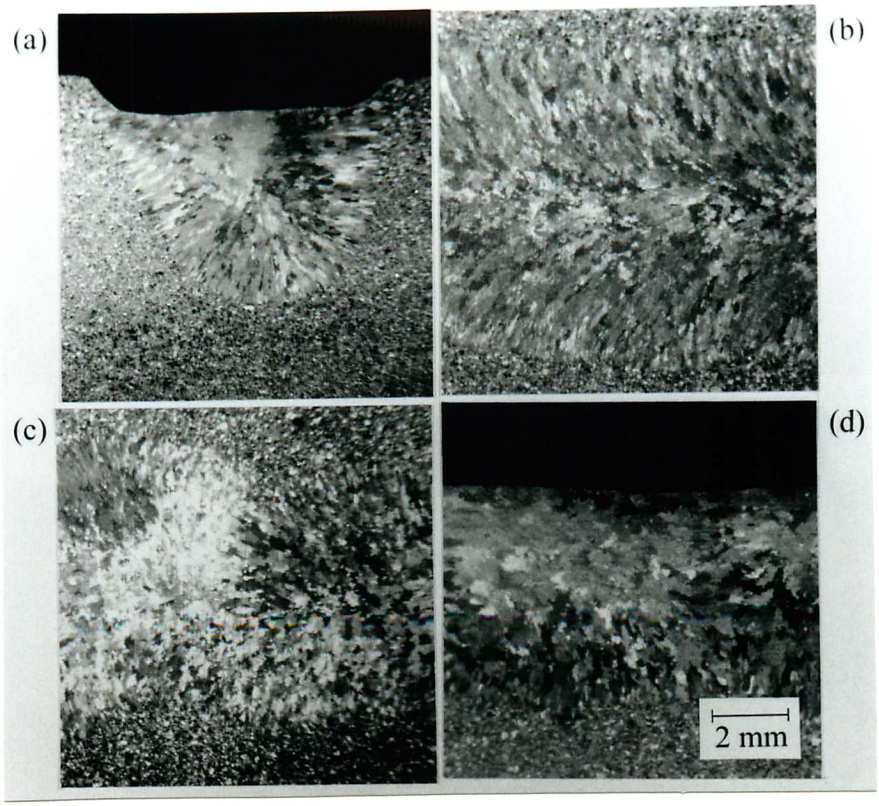

Fig. 5.15 - As-welded surface of the Si_3N_4 inoculated deposit.

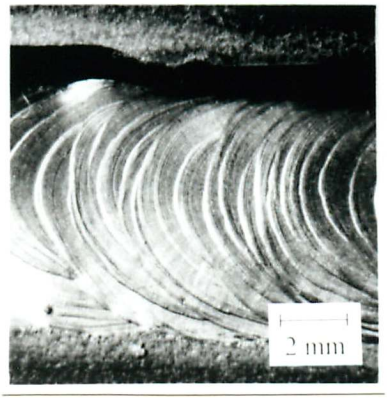

Fig. 5.16 - Microstructure of the A-TIG weld. (a) Transverse profile, (b) plan view 100 μm below weld surface, (c) plan view 1 mm below weld surface and (d) section along the weld centreline.

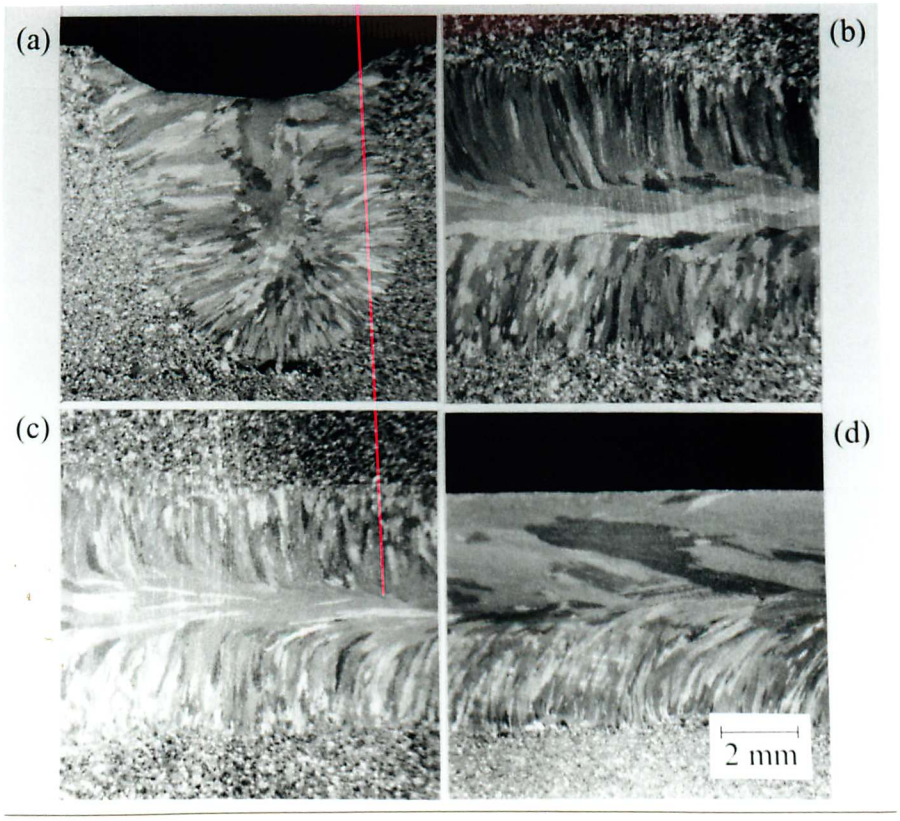

Fig. 5.17 - SEM image of fractured section of the Si_3N_4 inoculated weld. MnS inclusions only are located in cusps.

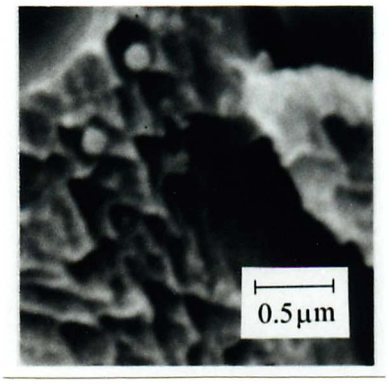

The measured concentrations of dissolved Si and N were 0.59 ± 0.03 wt% and 0.14 ± 0.02 wt%. The theoretical Si and N contents of the steel assuming complete dissolution of Si_3N_4 inoculant were estimated using the method from Section 5.3.4 and the filler material composition (Table 2.1), and found to be 0.64 wt% and 0.17 wt% respectively.

These results suggest that some Si and N remained bound as Si_3N_4 particles. However, if the nucleation efficiency was very high, few particles would be required to produce significant refinement. Consequently, the chance of finding nucleant particles in a random two-dimensional section would be low. This is in accordance with initial SEM observations.

Samples of Si_3N_4 inoculated weld metal were thus fractured in tension. Failure tends to initiate at inclusions, revealing a greater number of particles for examination. However, again only MnS inclusions were found (Fig. 5.17).

A method was then attempted whereby the steel matrix was electrolytically dissolved in 10% HCl in methanol at +1.5 V potential with respect to a platinum cathode (Gill and Gnanamoorthy, 1982). Filtration of the solution through a fine glass fibre mesh was used to collect any insoluble inclusions. However, no particles were apparent from SEM examination of the filters. The mesh size was 0.7 μm, whereas nucleant particles may have been smaller. The absence of extracted MnS inclusions could certainly be accounted for by this, as they were typically $<0.5\,\mu$m in diameter. Future tests involving centrifuging the solution would be required to check for the presence of the smallest particles. Another possibility is that the electrochemical conditions used may have also led to inclusion dissolution, in which case alternatives need to be sought.

The lack of success in finding nucleants prompted an experiment which provided indirect evidence that grain refinement occurred by nucleation on Si_3N_4 inoculant particles. If nucleants were present within the refined weld, successive remelting would facilitate their dissolution thereby eliminating the equiaxed structure and raising the concentrations of dissolved species (Kou and Le, 1986). This was achieved by making autogenous weld passes over the Si_3N_4 inoculated deposit.

After one pass, although some columnar grains appeared, the microstructure was still largely equiaxed (Fig. 5.18a–b). After two passes, the structure had reverted to that of the control, *i.e.* fully columnar with axial character (Fig. 5.18c–d). Chemical analyses of the steel matrix showed a slight increase in dissolved Si and N contents after the autogenous passes (Table 5.7). These results thus support the proposed existence of Si_3N_4 nucleant particles in the inoculated weld.

Fig. 5.18 - Microstructure of the Si_3N_4 inoculated weld after (a–b) one autogenous pass and (c–d) two autogenous passes. Plan views at 100 μm and 1 mm below weld surface are shown on the left and right respectively.

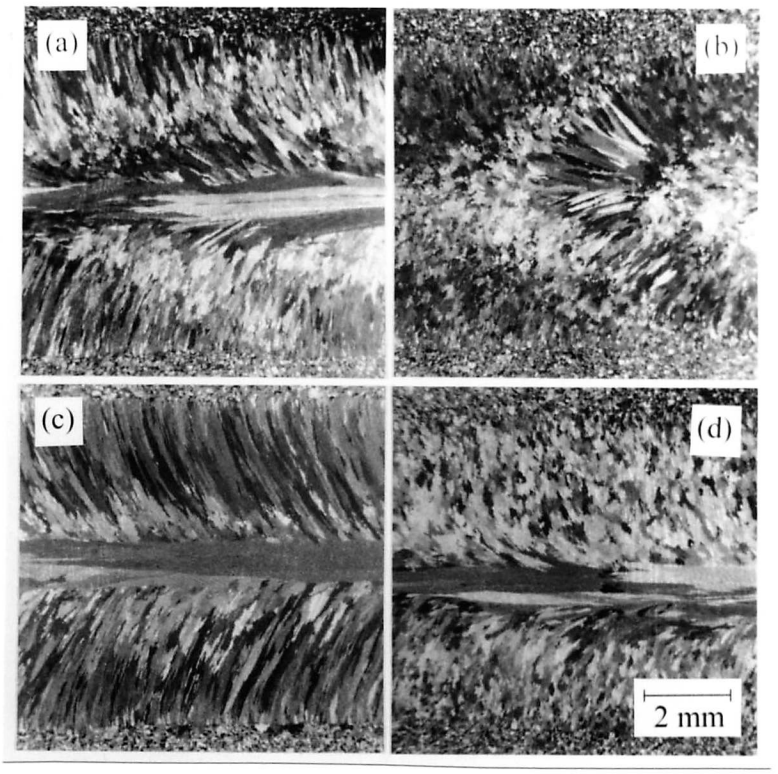

Fig. 5.19 - Proposed nucleation mechanism by Si_3N_4 inoculant.

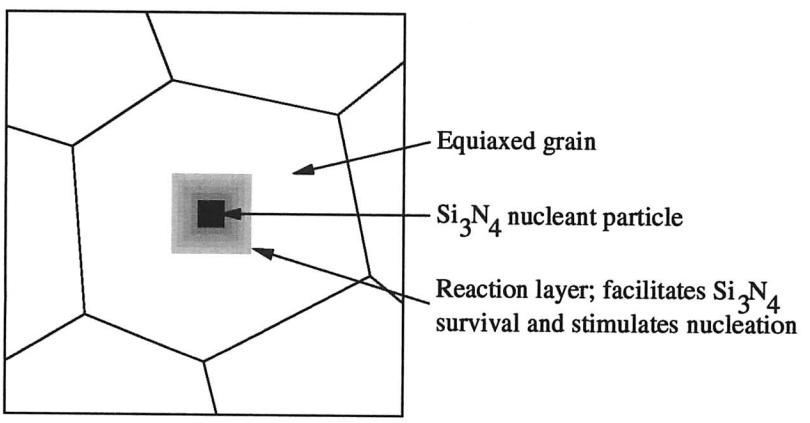

Table 5.7 - Dissolved Si and N contents of the Si_3N_4 inoculated weld before and after autogenous passes.

Weld	wt% Si	wt% N
Si_3N_4 inoculated	0.59 ± 0.03	0.14 ± 0.02
+ autogenous passes	0.65 ± 0.03	0.18 ± 0.02

It was predicted in Chapter 4 that Si_3N_4 inoculated welds would be unrefined due to total dissolution of the addition. However, the results were contrary to this. Further study of the literature revealed a possible contributory factor. It has been reported that Si_3N_4 undergoes a chemical reaction with steel above $\sim 700°C$ to give various binary iron silicides and nitrogen gas (Weitzer and Schuster, 1987). Whilst chemical analyses indicated that the majority of such products dissolved, some may have facilitated the survival of a few Si_3N_4 particles and led to efficient nucleation (Fig. 5.19). As a result of a reaction layer, the bond between Si_3N_4 inclusions and the steel may be stronger than the steel matrix itself. Hence in accordance with experimental observations, failure in the tensile fractured specimens would not initiate at nucleant particles, which remained undetected.

Consideration of the electrostatic contribution to nucleation (Section 5.4.2) also supports the existence of a reaction layer. Like the oxides, Si_3N_4 is a good insulator, with an electrical resistivity of $\sim 10^8$ ohm cm at the steel solidification temperature (Brook, 1991). Thus wetting by the steel would be unlikely if a distinct austenite/Si_3N_4 boundary had to be formed.

5.4.5 - HfC and TaN inoculated welds

The welds inoculated with HfC and TaN both exhibited similar characteristics. Fig. 5.20 shows that the HfC inoculated weld was partly refined, the coarse axial structure of the control replaced by finer columnar grains with interruptions along the weld centreline. The TaN inoculated weld (Fig. 5.21) displays extensive grain refinement; the axial structure has been eliminated and replaced by coarse equiaxed grains, although some columnar character persists closer to the fusion surface.

Examination of the as-welded surfaces shows the pool tail shape remained elliptical in both cases (Fig. 5.22), hence as with Si_3N_4 additions, the absence of columnar axial structures was not a result of flux interference with the weld pool tail. It should also be noted that the TaN inoculated weld surface was particularly clean and even, virtually indistinguishable from the control.

Fig. 5.20 - Microstructure of the HfC inoculated weld. (a) Transverse profile, (b) plan view 100 μm below weld surface, (c) plan view 1 mm below weld surface and (d) section along the weld centreline.

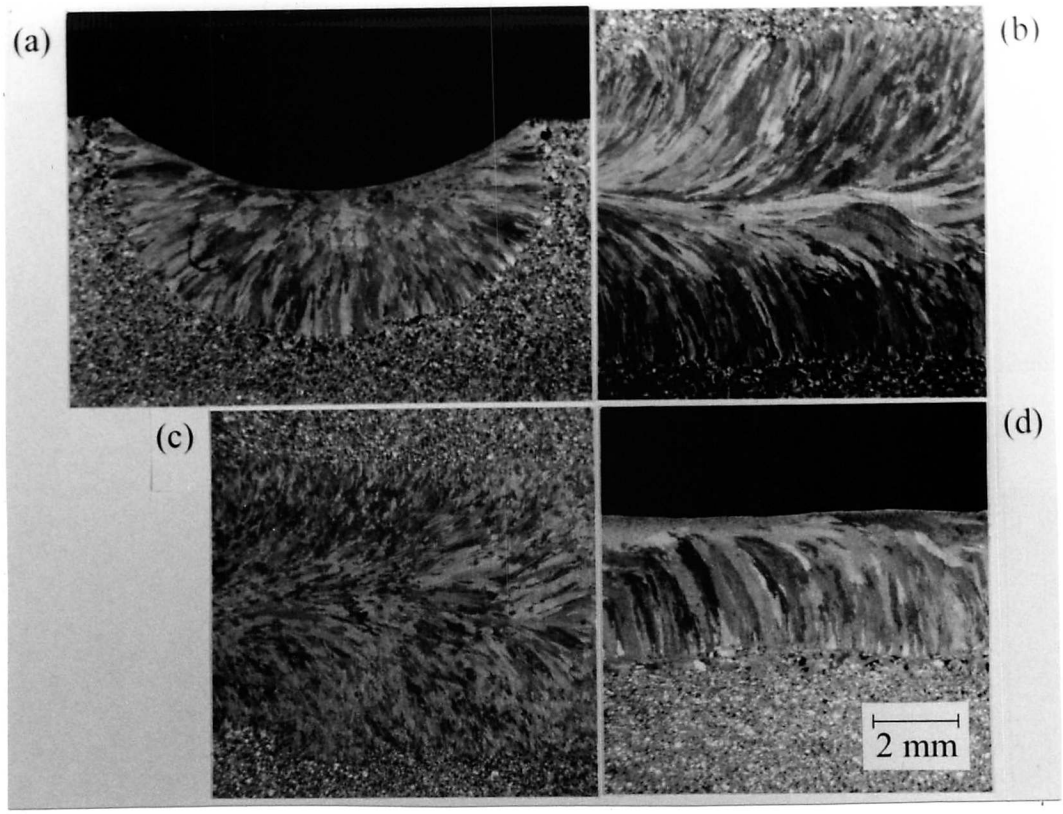

Fig. 5.21 - Microstructure of the TaN inoculated weld. (a) Transverse profile, (b) plan view 100 μm below weld surface, (c) plan view 1 mm below weld surface and (d) section along the weld centreline.

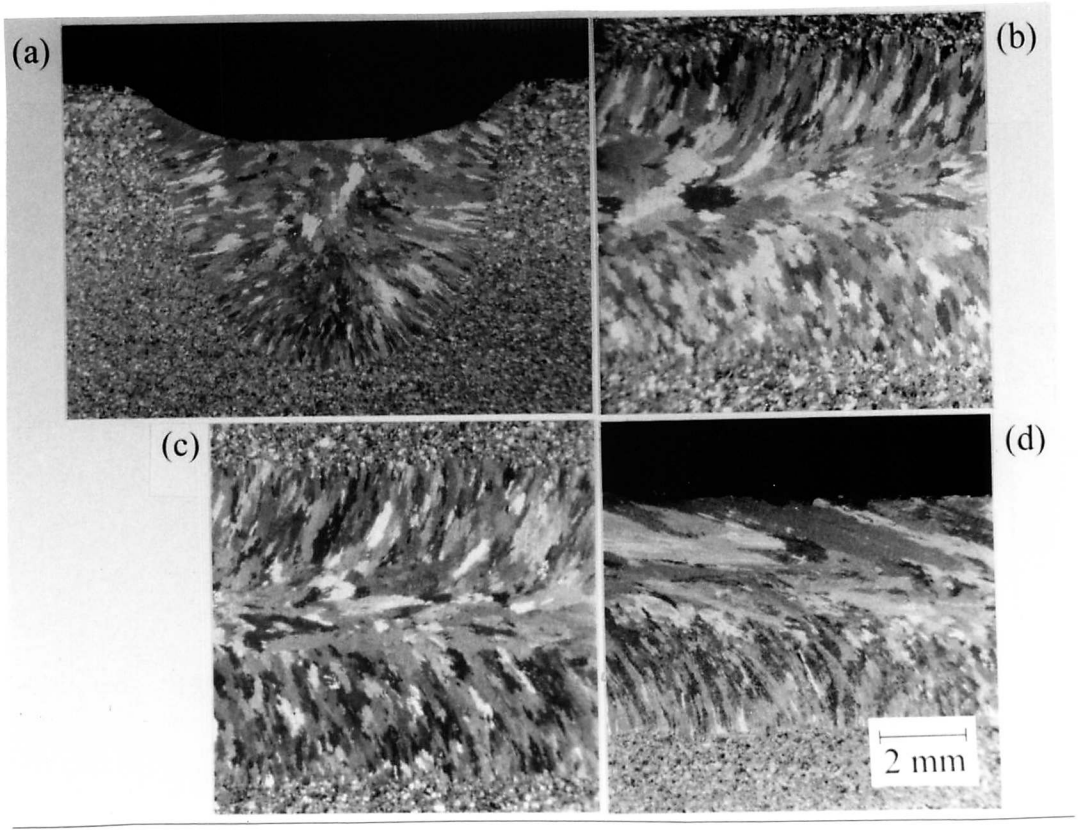

Fig. 5.22 - As-welded surfaces of (a) HfC and (b) TaN inoculated deposits.

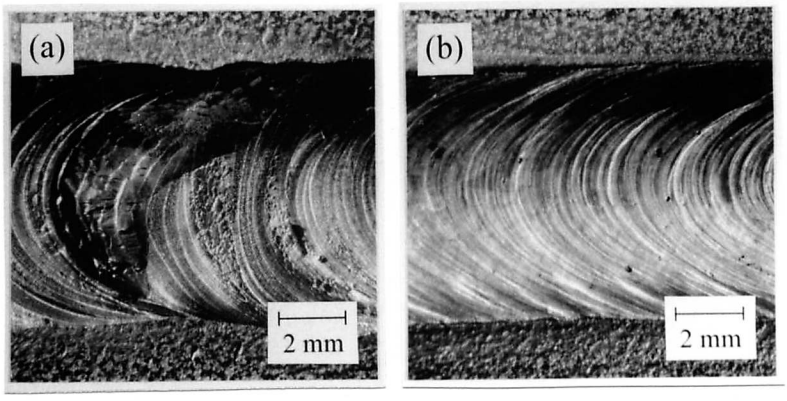

Fig. 5.23 - SEM images of (a) cuboidal inclusions within the HfC inoculated deposit and (b) a polyhedral inclusion within the TaN inoculated deposit. In each case the measured chemical composition corresponded to the inoculant used.

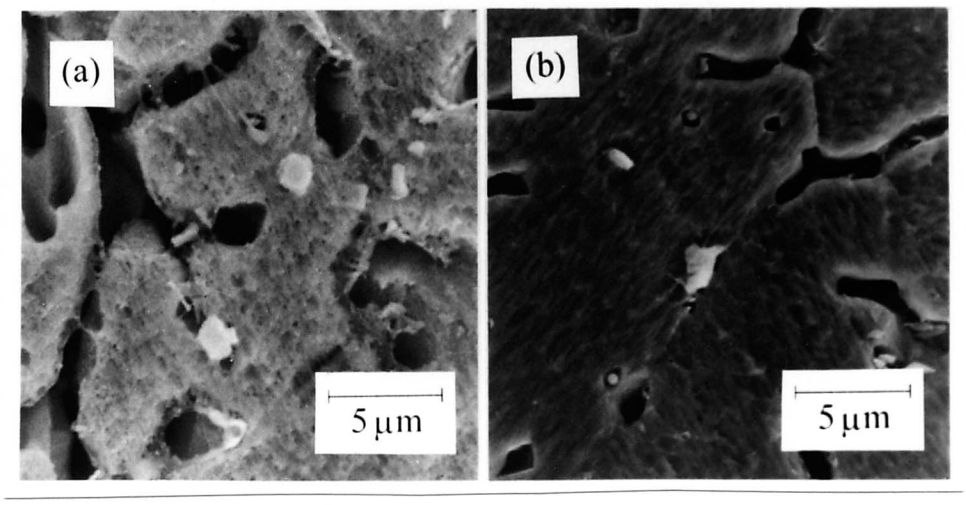

An increase in the depth-to-width ratio of the deposit was apparent as a result of using TaN flux (Fig. 5.21a), although as the A-TIG experiment demonstrated (Section 5.4.4), such a change in weld pool shape was not responsible for the observed refinement.

SEM and EDX analyses of the welds found both contained globular MnS inclusions. Each weld also contained inclusions corresponding to the flux addition. Cuboidal particles composed of Hf, Zr and C were observed throughout the HfC inoculated deposit (Fig. 5.23a; Table 5.8), and polyhedral inclusions containing Ta and N with traces of Nb, La and Ce were present in TaN inoculated weld metal (Fig. 5.23b; Table 5.9).

Table 5.8 - Typical measured composition in wt% of a cuboidal particle within the HfC inoculated weld. Small amounts of Zr are always present in Hf compounds unless specially purified (Clark *et al.* 1973).

Hf	Zr	C
91.4	0.9	7.7

Table 5.9 - Typical measured composition in wt% of a polyhedral inclusion within the TaN inoculated weld. Nb, La and Ce are trace impurities.

Ta	N	Nb	La	Ce
92.0	7.6	0.2	0.1	0.1

From the method outlined in Section 5.3.4 and the filler material composition (Table 2.1), the theoretical concentrations of dissolved species assuming total dissolution of the inoculant addition were estimated (Table 5.10). The measured concentrations of each are also listed in Table 5.10. A comparison of the initial inoculant particle size and the observed inclusion size is given in Table 5.11. The results show that in both cases inoculant particles survived in the melt, but that TaN particles dissolved to a greater extent than HfC. This is in agreement with the relative solubilities calculated in Section 4.3.3 (Fig. 4.6).

Fig. 5.24 - SEM images of flat, polished sections of (a) HfC and (b) TaN inoculated welds showing the relative inclusion densities.

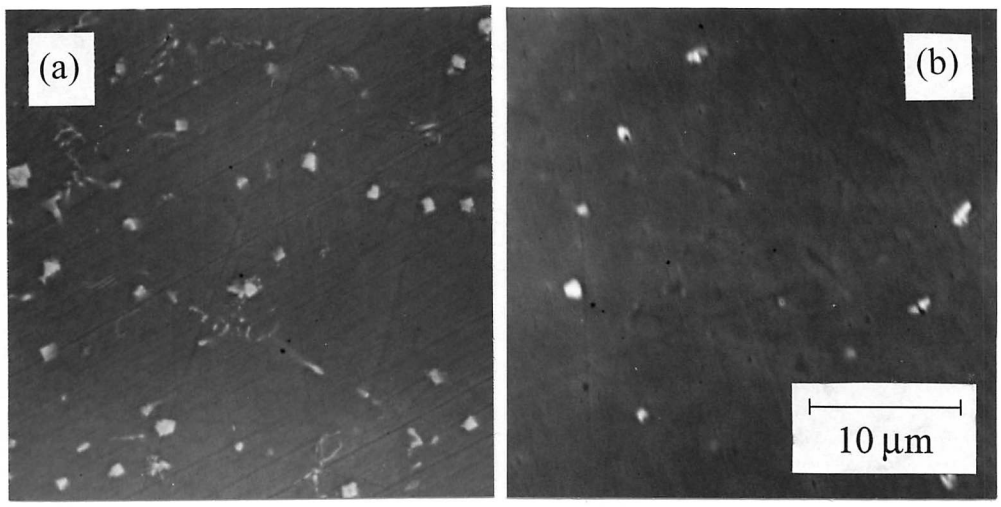

Fig. 5.25 - Variations in G_L and R within a weld pool (David and Vitek, 1993).

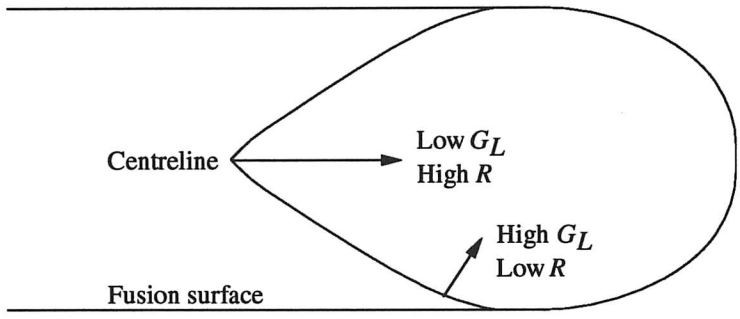

Table 5.10 - Concentrations of dissolved species. Theoretical refers to calculations assuming total inoculant dissolution. A greater proportion of TaN inoculant dissolves compared with HfC, indicating its higher relative solubility.

Weld	Concentration of dissolved species (wt%)
HfC theoretical	Hf=1.49, C=0.11
HfC measured	Hf=0.18 ± 0.02, C=0.02 ± 0.01
TaN theoretical	Ta=1.14, N=0.11
TaN measured	Ta=0.65 ± 0.04, N=0.06 ± 0.01

Table 5.11 - Comparison of initial inoculant particle size and observed inclusion size. TaN inclusions were significantly smaller than the added particles, whereas HfC inclusions were of similar size. This again illustrates the higher solubility of TaN.

Inoculant	Initial size (μm)	Final size (μm)
HfC	2	1–2
TaN	5	1–2

The electrostatic contribution to nucleation (Section 5.4.2) is favourable to the wetting of steel on HfC and TaN particles. HfC and TaN have primarily metallic conductivity, with low electrical resistivities in the order of 10^{-2}–10^{-1} ohm cm at the steel solidification temperature (Brook, 1991; Upadhyaya, 1996), facilitating the necessary charge redistribution when an austenite/particle interface forms. Consequently lattice mismatch provides the only barrier to nucleation and should thus determine the relative potency of HfC and TaN nucleants (Section 3.3.3).

The nucleation efficiencies of HfC and TaN were gauged by relating the number of inclusions to the extent of refinement attained. If the inclusions are assumed to be cubes, then from a random two-dimensional section, the number of inclusions per unit volume is given by

$$N_V = \frac{2N_A^2}{3N_L} \tag{5.10}$$

where N_A is the number of interceptions of inclusions per unit test area, and N_L is the number of interceptions per unit length of test line (Underwood, 1970). Counting was performed on flat, polished sections of each weld, viewed in the SEM with a grid superimposed over the

screen. In the secondary electron imaging mode intersected inclusions were clearly seen as light dots on a dark background (Fig. 5.24), the strong contrast arising from the large difference in relative atomic mass between the matrix and inclusions.

For the TaN inoculated weld, $N_V = 3.2 \pm 0.3 \times 10^{14}\,\mathrm{m}^{-3}$. For the HfC inoculated weld, $N_V = 1.5 \pm 0.4 \times 10^{16}\,\mathrm{m}^{-3}$. This indicated that the number of potential nucleation sites was ~ 50 times greater than in the TaN inoculated weld. However, the microstructure was much less refined.

The results show that TaN is a more potent nucleant for austenite than HfC, and are therefore consistent with disregistry theory. The lattice mismatch between austenite and TaN is 1.95% compared with 8.84% for HfC (Section 4.2.5), hence TaN inoculants would be expected to produce more efficient grain refinement.

However, the refinement by TaN inoculation can still be considered inefficient if it is taken that 1 inclusion per grain constitutes 100% nucleation efficiency. From the measured value of N_V, a typical equiaxed grain, roughly approximated as a cube $100 \times 100 \times 100\,\mu\mathrm{m}^3$, would contain in the order of 300 TaN inclusions. Similar levels of nucleation efficiency have been reported for TiN particles in ferritic stainless steel welds (Heintze and McPherson, 1986), and for Al_3Ti-coated TiB_2 particles in aluminium casts (Greer *et al.* 2000).

It has been suggested that "poisoning" of nucleants by impurities or thin layers of other phases can impair nucleation efficiency. It is well documented that Zr additions to aluminium casts reduce the degree of refinement attainable, by substituting for Ti in the TiB_2 particles and their Al_3Ti coating (Jones and Pearson, 1976). Some evidence exists that sulphide layer formation stifles the effect of TiN nucleants in ferritic steels (Ostrowski and Langer, 1979b), although this has been dismissed by others (Heintze and McPherson, 1986).

Whilst it is true that the HfC and TaN inclusions contained impurities, the content was extremely low (Tables 5.8 and 5.9), and their effect on nucleation could not be assessed without comparison with 100% pure inoculants. SEM and EDX analyses did not reveal any apparent coating layers on inclusions, although as these may be only a few monolayers thick, the sensitivity of the equipment may have been inadequate for their detection.

Nucleation efficiency is also affected by solidification conditions which control the extent of nucleation and growth, and thus microstructural development within the weld pool. The ratio G_L/R (G_L=thermal gradient within the liquid, R=crystal growth rate) is frequently used to describe this. A low G_L/R ratio promotes the formation of an equiaxed structure (Section 3.2.6).

G_L and R both vary considerably from the fusion surface where G_L/R is high, to the centreline where G_L/R is low (Fig. 5.25) (David and Vitek, 1993). In accordance with this theory, both the HfC and TaN inoculated welds show the greatest degree of refinement close to the weld centre. However, parameters such as welding speed and heat input influence the absolute values of G_L and R throughout the weld pool, hence as the experiments demonstrate, even at the weld centre the nucleation efficiency can be low.

In summary, grain refinement of austenitic stainless steel welds can be achieved by inoculation with HfC and TaN. The presence of such inclusions within refined grains suggested that refinement occurred by the intended mechanism; particles remained stable in the melt and acted as heterogeneous nucleation sites as a result of close lattice matching. The experiments verified the predictions made in Chapter 4. The observed nucleation potency of the compounds tallied with the calculated disregistries, and TaN was shown to be more soluble in steel than HfC.

5.5 - Summary

The experiments have shown that grain refinement of austenitic stainless steel welds can be achieved by inoculation with Si_3N_4, TaN and HfC particles, in decreasing order of effectiveness. A number of predictions made during the inoculant selection procedure presented in Chapter 4 were verified:

- Oxide inoculants were insoluble.
- BN additions completely dissolved, no grain refinement ensued, and detrimental effects on weld quality were observed.
- HfC and TaN had low solubilities; HfC was less soluble than TaN.
- HfC and TaN nucleated austenite; TaN was a more potent nucleant as a result of closer lattice matching.

Other results contradicted predictions:

- α-Al_2O_3, cubic-HfO_2, SiO_2 (β-cristobalite), and cubic-ZrO_2 additions did not nucleate austenite.
- Extensive grain refinement occurred using Si_3N_4 additions, which were predicted to undergo complete dissolution.

The experiments thus indicated the incompleteness of the inoculant selection procedure, which was based only on the disregistry and solubility of compounds with respect to austenitic steels.

However, where results did not match predictions, further research into the inoculants' properties yielded satisfactory explanations. The proposed existence of an electrostatic contribution explained the failure of the oxides to nucleate austenite and was also consistent with the results for other inoculants. The chemical reaction between Si_3N_4 and steel provided a plausible reason for the unexpected observations, although further work is needed before this can be confirmed.

Chapter 6 - Single-pass welds : Part 2

6.1 - Introduction

The initial single pass experiments detailed in Chapter 5 established that the microstructures of austenitic stainless steel welds could be refined by additions of nucleant particles. Further experiments were thus performed to confirm the usefulness of inoculant fluxes and to gain an improved understanding of the factors involved and possible limitations. TaN inoculant flux offered the best prospects for achieving these aims, as it had been shown to efficiently nucleate austenite via the intended mechanism of providing inert heterogeneous nucleation sites.

6.2 - Effect of increased welding speed and heat input on inoculant performance

Experimental work carried out by Ganaha *et al.* (1980) showed that increasing welding speed and heat input favoured columnar-to-equiaxed transitions in aluminium welds refined by Al_3Ti-coated TiB_2 particles. Higher welding speeds increased growth rates and higher heat inputs minimised thermal gradients. The G_L/R ratio was thus lowered throughout the weld pool (Fig. 5.25). Higher welding speeds also tended to reduce the time available for dissolution, allowing more potential nucleants to survive.

Control and TaN inoculated welds (S1–S4) were made to investigate such effects on nucleation efficiency. The weld geometry shown in Figure 5.1 was again used, but with welding parameters modified as shown in Table 6.1.

Table 6.1 - Modified welding parameters for control and TaN inoculated welds (S1–S4).

Weld	TaN flux	Current (A)	Voltage (V)	Welding speed ($mm\,min^{-1}$)	Heat input ($kJ\,mm^{-1}$)
S1	×	335	13	125	1.25
S2	√	335	13	125	1.25
S3	×	450	14	150	1.5
S4	√	450	14	150	1.5

Fig. 6.1 - Transverse cross-sections of (a–d) S1–S4.

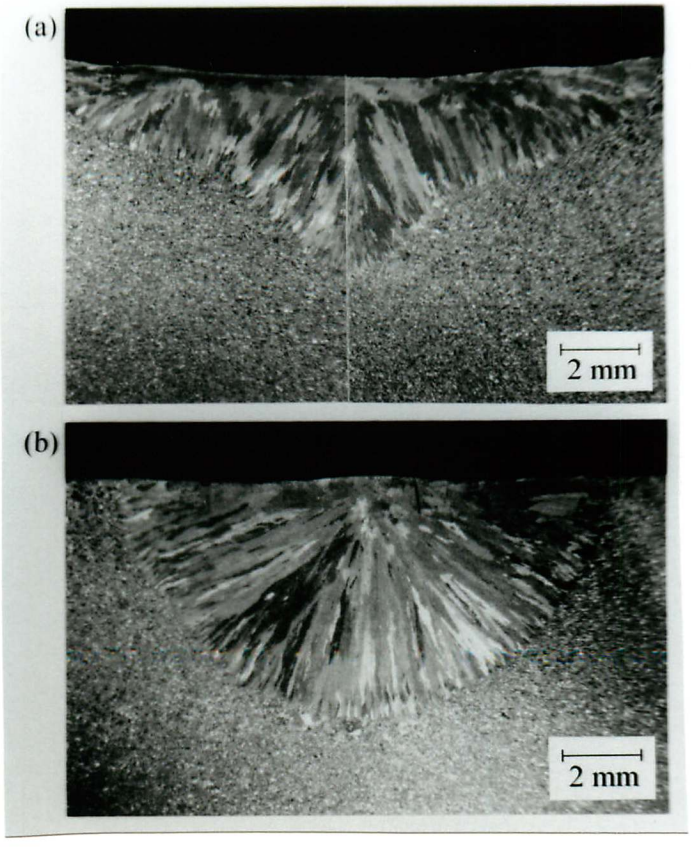

(Fig. 6.1 continued)

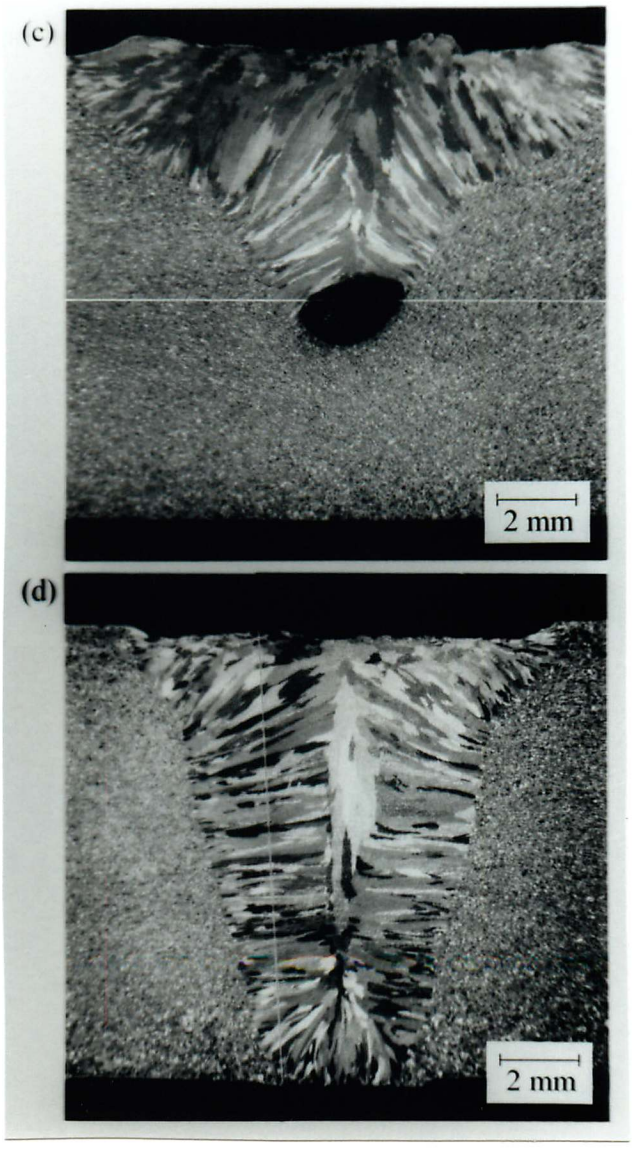

However, a comparison of transverse profiles of the control and inoculated welds (Fig. 6.1) clearly shows that grain refinement did not occur in spite of the TaN additions. The reason for this was that the same area of grooved plate had been covered with TaN flux for welds S2 and S4 as it had for the original TaN inoculated weld (Section 5.4.5). The much higher heat inputs, though, produced deposits of over double the volume. Consequently, the additions of TaN to S2 and S4 as estimated from Equation 5.7 were reduced to 0.56 wt% and 0.39 wt% respectively, corroborated by chemical analyses of S2 and S4 (Table 6.2). Substitution into the temperature dependent solubility product equation for TaN in liquid steel (Table 4.6), suggests that at these concentrations TaN particles should not survive in the melt. The absence of TaN inclusions in S2 and S4 was confirmed by SEM examination.

Table 6.2 - Concentrations of dissolved inoculant species in welds S2 and S4. Ta from EDX measurements, N from ICPS by Bodycote Materials Testing Ltd.

Weld	Ta (wt%)	N (wt%)
S2	0.60 ± 0.04	0.05 ± 0.01
S4	0.33 ± 0.04	0.04 ± 0.01

A key point is thus apparent from these experiments; the importance of particle solubility. TaN has been shown to be a good nucleant for austenite, but if the level of addition is too low, such that all TaN particles completely dissolve, then grain refinement does not occur. Therefore the use of inoculant powder fluxes is limited. For a given level of flux coverage the ratio between the plate area covered by flux, A_p, and the weld pool volume, V_w, must exceed a certain value, such that the addition provides high enough M and X concentrations for MX particles to remain stable within the weld pool. These experiments demonstrate that this may not be possible to achieve for all welding procedures and geometries.

It is also immediately obvious from Fig. 6.1 that the use of TaN flux led to enhanced penetration. A small change in weld profile had been observed in the original TaN inoculated weld (Section 5.4.5), but the effect was much more pronounced with increased heat input. The conditions used for S3 and S4 were outside the normal operating range of the welding unit, and S3 contained a tunnel-like void running under the length of the deposit (Fig. 6.1c). Such defects are often seen in material TIG welded under extreme conditions, and are attributed to the high arc force on molten weld metal entrapping shielding gas (Leonard, 1999). The full penetration in S4, however, prevented this from occurring (Fig. 6.1d).

In A-TIG welding (Section 5.4.4), activating fluxes are used to increase penetration. The mechanism by which this occurs has only recently been investigated properly (Segar, 2000). The presence of flux affects the arc forces acting on the weld pool. A diagram of a conventional TIG arc is shown in Fig. 6.2. Electrons are thermionically emitted at the cathode spot on the tungsten electrode, and travel through the plasma column to be absorbed by the workpiece at the anode spot. Hence there is a net current flow into the weld pool. The interaction of this current with its own magnetic field generates an electromagnetic force, called the Lorentz force, directed away from regions of high current density, *i.e.* the anode spot (Lancaster, 1987). Lorentz forces thus affect the flow of weld metal.

When activating flux is present, it melts and floats on the weld pool surface beneath the arc. This has been observed using video techniques (Segar, 2000). Current flow is concentrated through the flux and the arc is constricted. The size of the anode spot is reduced, increasing the current density. The Lorentz force downwards into the pool at the weld centreline is thus magnified, and the hottest liquid is forced to flow towards the weld root, thereby increasing penetration (Fig. 6.3).

The effect is accentuated by Marangoni convection (Section 2.2.2). The primary constituent of activating flux, TiO_2 (Table 5.6), is partially reduced and some of the liberated oxygen dissolves in the weld pool (Heiple and Roper, 1982). Oxygen imparts a positive coefficient of surface tension to liquid steel, thus flow is directed downwards at the weld centre.

However, the use of TaN flux is not consistent with this explanation. Firstly, activating fluxes float on the weld pool surface; apart from a minute increase in oxygen content the deposit composition is unaffected. After welding, the deposit is covered with a fused slag corresponding to non-stoichiometric Ti oxides. The TaN inoculated weld surfaces were clean and free from slag, and chemical analyses (Table 6.2) indicated that all the TaN flux had been incorporated into the deposit. Secondly, Marangoni effects are unlikely. Nitrogen is not surface active in steel, and although no data exist for Ta, transition metals are not generally thought to have an effect (Halden and Kingery, 1955). Further investigations of the effects of TaN flux on weld penetration need to be undertaken before a full explanation of the phenomenon can be made.

Fig. 6.2 - Conventional TIG arc (Lancaster, 1987).

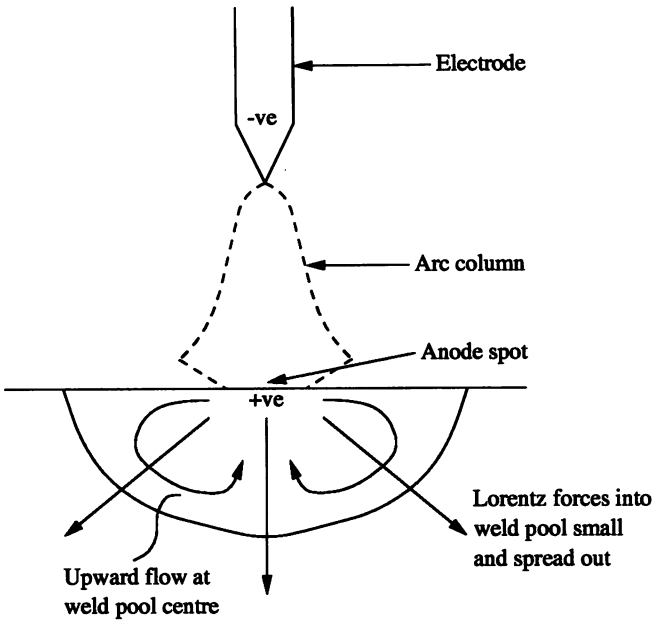

Fig. 6.3 - TIG arc when activating flux present (Segar, 2000).

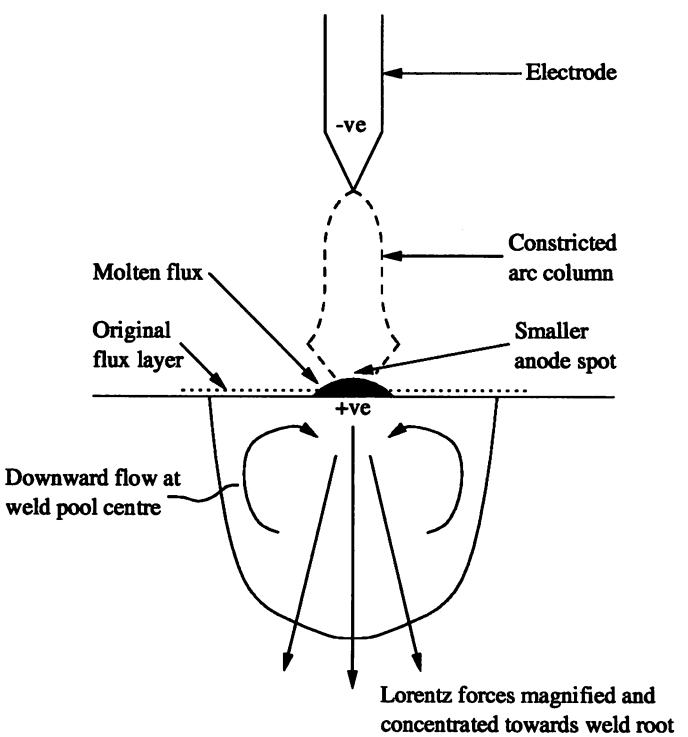

Fig. 6.4 - TIG welding with filler wire and inoculant flux.

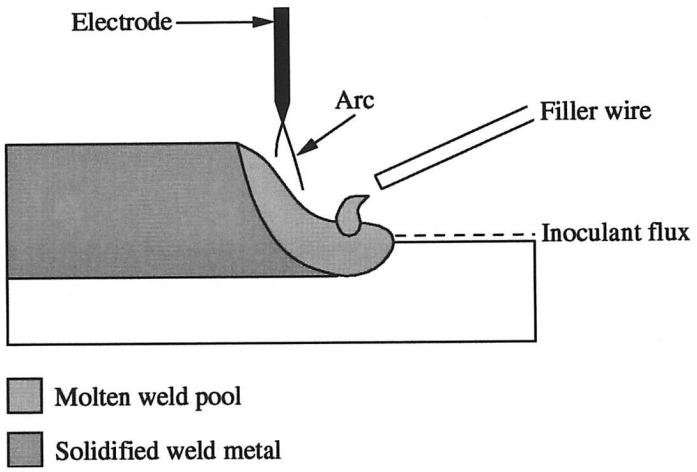

Fig. 6.5 - Autogenous TIG welding with inoculant flux.

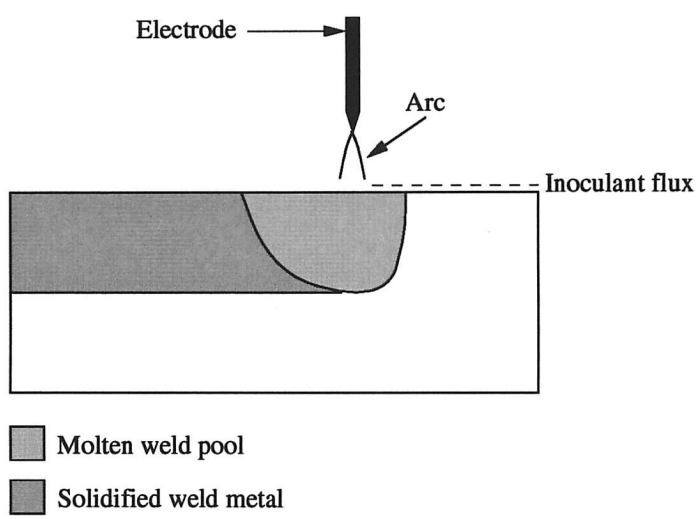

6.3 - Direct inoculant flux additions to autogenous welds

All of the inoculated welds discussed thus far have been made using the TIG process with filler material. During welding in this manner, the arc is kept near to the back of the pool and filler material is fed in from the front (Fig. 6.4), because if the wire made direct contact with the arc, excessive back-melting would cause it to collapse (Kearns, 1978; Davies, 1989). When inoculant flux is present, it enters the weld pool near the base and away from the arc.

Flux would have more intimate contact with the arc during autogenous welding (Fig. 6.5). The effect of the inoculant addition on grain refinement, weld pool shape, deposit quality and so on may thus be significantly different. Control and TaN inoculated autogenous welds were made to investigate this. To further study penetration effects (Section 6.2), welding with TiO_2 (the primary constituent of activating flux) and TaN-TiO_2 mixed fluxes was also performed. The experiments are summarised in Table 6.3 together with the welding parameters. Welds were made over coupons of flat plate 150×100×12 mm.

Table 6.3 - Autogenous welds (S5–S8) and welding parameters.

Weld	Flux	Current (A)	Voltage (V)	Welding speed ($mm\,min^{-1}$)	Heat input ($kJ\,mm^{-1}$)
S5	None	150	10	150	0.36
S6	TaN	150	10	150	0.36
S7	TiO_2	150	10	150	0.36
S8	TaN-TiO_2 mixed	150	10	150	0.36

The microstructures of the four deposits are illustrated in Figs. 6.6 and 6.7. S5 is fully columnar, and has a wide, shallow profile. S6 shows that the TaN flux has produced extensive grain refinement. Penetration is also enhanced, but only by a small margin, which is consistent with the trend that this effect of TaN is less significant at low heat inputs. S7 is unrefined, but the TiO_2 flux has greatly increased penetration. The mixed flux used for S8 has led to grain refinement and enhanced penetration, but each to a lesser degree than addition of pure TaN and TiO_2 respectively.

Fig. 6.6 - Transverse cross-sections of (a–d) S5–S8.

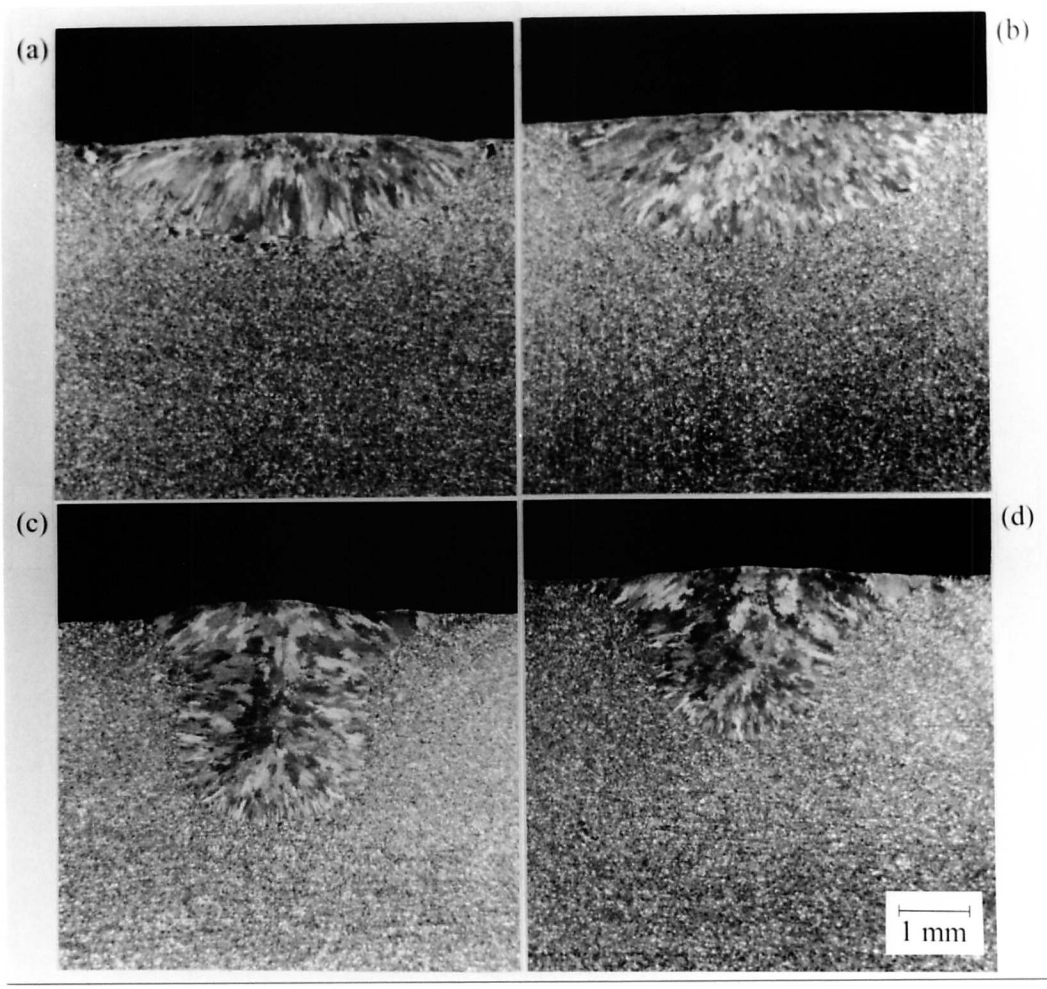

Fig. 6.7 - Plan views 100 μm below weld surface of (a–d) S5–S8.

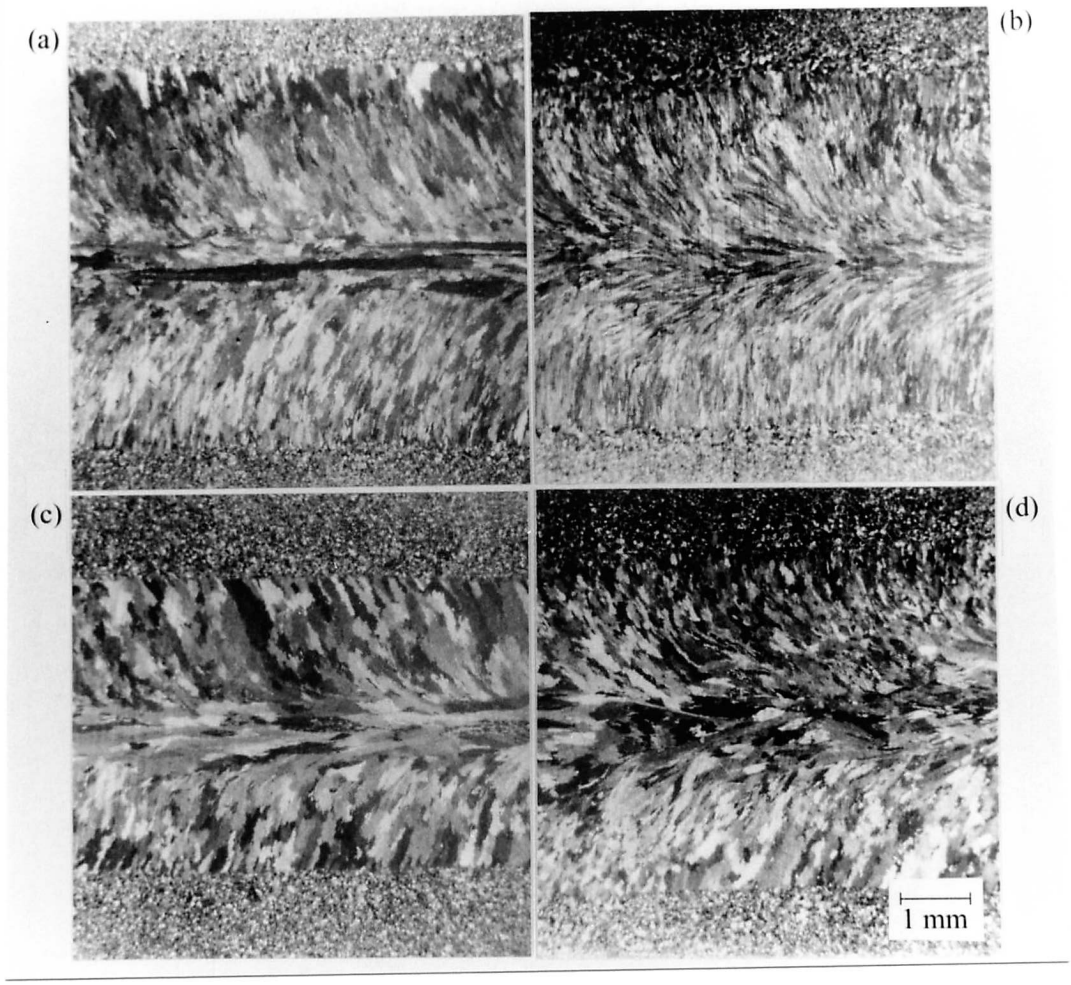

Fig. 6.8 - As-welded surfaces of (a–d) S5–S8.

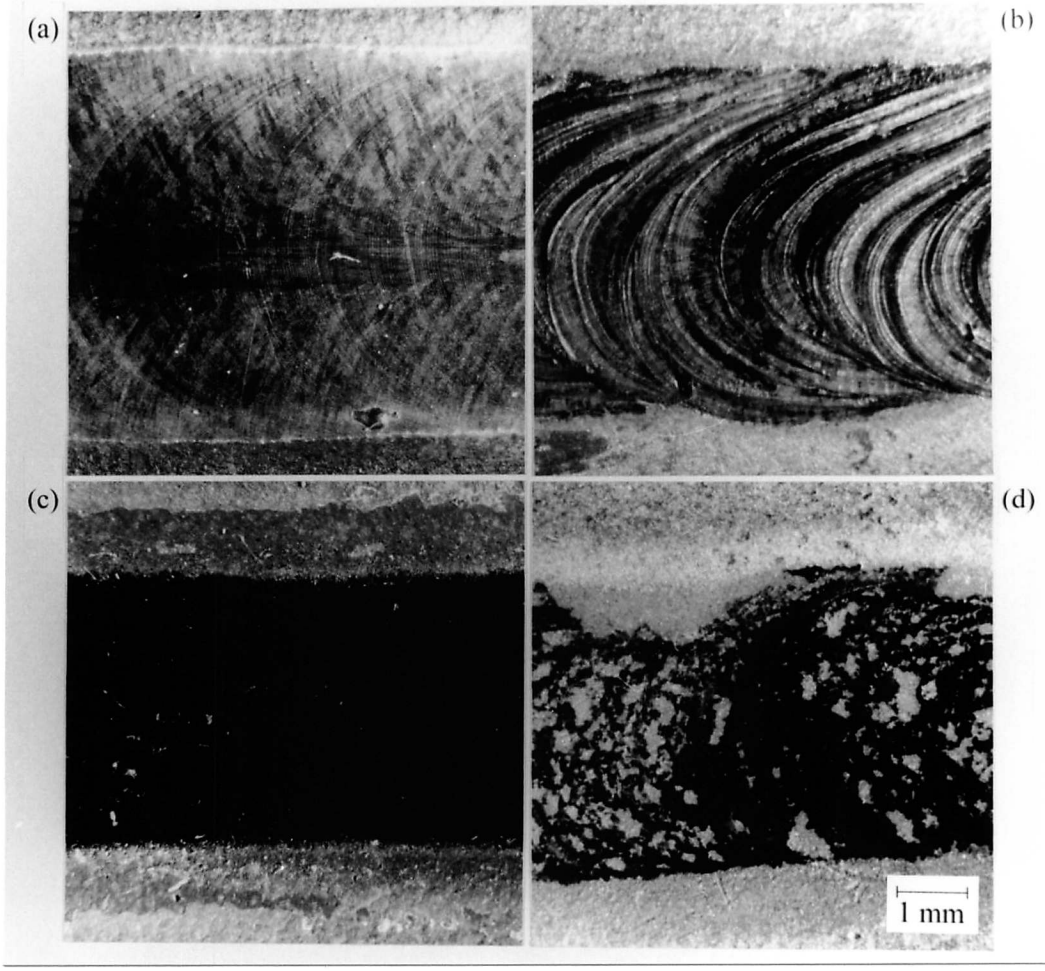

The as-welded surfaces of each deposit are shown in Fig. 6.8. The control weld, S5, is clean, even and exhibits an elliptical pool tail shape. Whilst the surface of S6 is free from slag and the pool tail shape remains elliptical, autogenous welding over TaN flux has produced a much more uneven deposit, with the level of disruption far greater than when the same flux is used during welding with filler material (Fig. 5.22b). This can be attributed to the more intimate contact between flux and arc during autogenous welding. S7 is covered with a fused black slag, which is also present over S8 albeit intermittently.

SEM and EDX analyses showed that all four deposits contained MnS inclusions. S6 and S8 also contained TaN inclusions, although the number density of particles was substantially lower in S8 (Table 6.4). No TiO_2 inclusions, dissolved Ti, or detectable increase in oxygen content were apparent in S7 and S8. The slag coverings present over these deposits, however, were composed almost entirely of Ti and O. The correlation between grain refinement and the presence of TaN inclusions for these welds provides further evidence that such particles nucleate austenite. Similarly, significantly enhanced penetration occurs only in the presence of TiO_2 flux. When mixed TaN-TiO_2 flux is used, each component appears to act independently.

Table 6.4 - Number of TaN inclusions per unit volume.

Weld	N_V (m^{-3})
S6	$6.0 \pm 0.3 \times 10^{15}$
S8	$1.8 \pm 0.4 \times 10^{14}$

The amount of TaN added to S6 and S8 was calculated using a modified form of Equation 5.7, which takes into account the different weld geometry:

$$x_{MX} = \frac{w\overline{m}_p}{7.8A_w + w\overline{m}_p} \times 100 \qquad (6.1)$$

where w is the width of the weld deposit at the surface in cm. For S6, $\overline{m}_p = 0.030\,g\,cm^{-2}$ (Table 5.2), thus the addition of TaN was ~2.0 wt%. S8, however, used a mixed TaN-TiO_2 flux in which $0.5\,cm^3$ of each powder was added to 10 ml acetone to give the required consistency (Section 5.2.1). Because each component acts independently, the coverages can be treated separately. The mean TaN coverage from the mixed flux was thus half that from the pure TaN flux, *i.e.* $\overline{m}_p = 0.015\,g\,cm^{-2}$, hence the TaN addition to S8 was ~1.0 wt%.

According to the solubility product from Table 4.6, the additions to both S6 and S8 are sufficient for TaN particles to survive in the melt and hence act as nucleation sites, but to a lesser extent in S8 (Fig. 6.9). Consequently, as was observed, S6 contained more TaN inclusions and thus displayed a higher degree of grain refinement in accordance with the theory that increasing the number density of nucleation sites favours columnar-to-equiaxed transitions (Fig. 3.9).

Qualitatively the same argument applies to the enhanced penetration effect of TiO_2 flux. In S8 only half as much TiO_2 was present compared with S7 hence penetration was reduced accordingly, as was the resulting amount of slag which prevented complete coverage of the S8 deposit.

Careful close observation of the molten pool was made during welding using a protective visor (Fig. 6.10). For S6, TaN flux was seen to become incorporated into the melt, moving outwards from the centre of the weld pool. For S7, a globule of TiO_2 flux could be seen floating beneath the arc, consistent with observations made on activating fluxes (Section 6.2). When the mixed TaN-TiO_2 flux was employed for S8, a small globule of flux floated on the pool surface under the arc, whilst other flux became incorporated into the melt, moving in towards the pool centre. It was assumed that these were the TiO_2 and TaN components respectively. The TaN flux also acted as a marker to indicate the direction of flow within the weld pool. In S6 no significant increase in penetration occurred, hence as would be expected, the flux motion indicated upward flow at the pool centre. Conversely, in S8 the flux motion confirmed downward flow at the pool centre, consistent with the observed increased penetration.

In a manner identical to that presented above, Villafuerte *et al.* (1995) attempted to grain refine autogenous welds of ferritic stainless steel. They used TiN flux as an inoculant, the compound having been shown on numerous occasions to be an excellent nucleant for ferrite (Section 3.3.6). However, their experiments were unsuccessful as the flux merely floated on the weld pool surface without becoming incorporated into the melt. Only by manually stirring TiN powder into large stationary welds was grain refinement achieved.

In conjunction with the present results, this suggests that another factor may be important when welding with inoculant fluxes—the density of the compound. The densities of steel (assumed to be approximately the same as Fe), TiO_2, TiN and TaN are given in Table 6.5. Both TiO_2 and TiN have lower densities than steel, hence during welding when flux meets the approaching molten pool it simply floats on the liquid surface (Fig. 6.11a). On the other hand, the much denser TaN flux immediately begins to sink allowing its incorporation into the melt (Fig. 6.11b).

Fig. 6.9 - Liquid/liquid+TaN phase boundary in austenitic stainless steel at 1750 K, *i.e.* just above the solidification temperature. Additions to both S6 and S8 sufficient for TaN particles to exist within the melt, but to a lesser extent in S8. *n.b.* Additions converted to at% and inherent nitrogen content of the steel added.

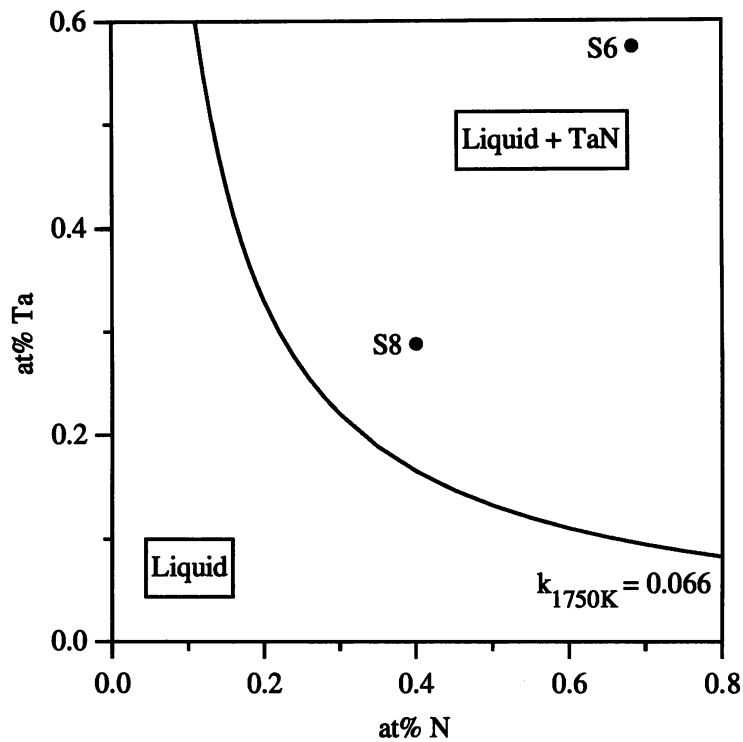

Fig. 6.10 - Appearance of pool surfaces during welding. (a) S5; control weld pool, (b) S6; TaN becomes incorporated into the melt, moving outwards from the pool centre, (c) S7; TiO_2 floats beneath arc and (d) S8; small TiO_2 globule floats beneath arc whilst TaN becomes incorporated into the melt, moving in towards the pool centre.

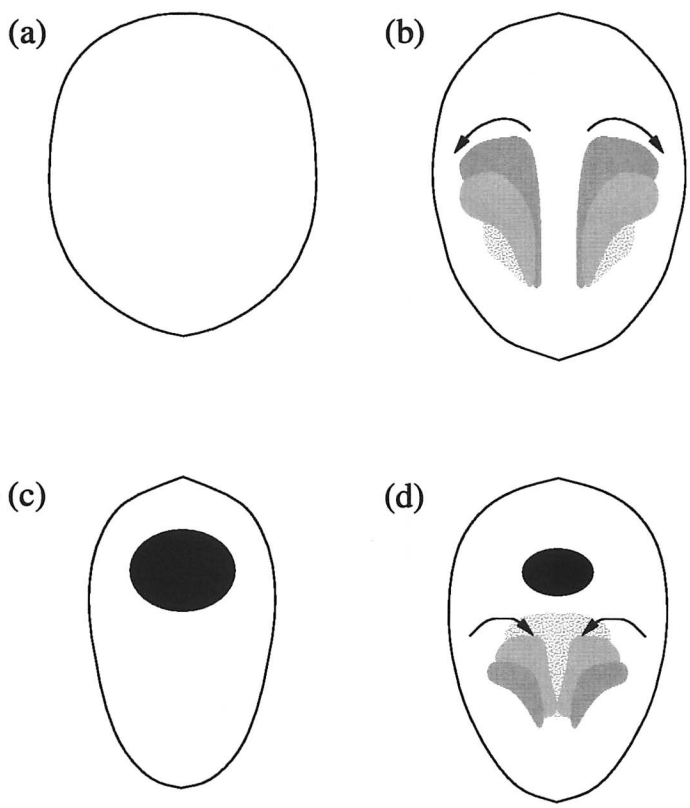

Fig. 6.11 - Comparison between flux welding with inoculants (a) less dense than the steel, *e.g.* TiN or TiO_2, and (b) more dense than the steel, *e.g.* TaN.

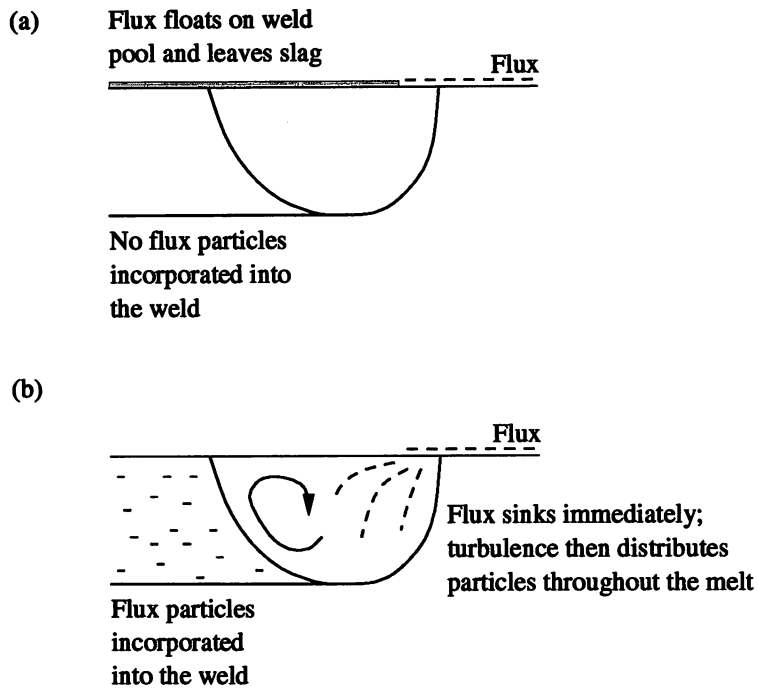

Table 6.5 - Room temperature densities of steel and inoculant compounds.

Material	ρ_{298K} ($g\,cm^{-3}$)
Steel	7.8
TiO_2	4.2
TiN	5.2
TaN	14.4

However, this hypothesis alone implies that TiN particles should also float out of welds in which they are precipitated as a result of alloying additions, thus precluding them from acting as nucleants for ferrite. It is well established, though, that this is not the case. Work by Sugden and Bhadeshia (1988) provides an explanation of this apparent anomaly.

Particles within a weld pool are subjected to extremely turbulent conditions as a result of the flow generated by Lorentz forces (Section 6.2), which distributes them throughout the melt. The turbulence subsides as the heat source recedes and the temperature in the melt is reduced (Easterling, 1984), leaving a fine dispersion of particles within the liquid. Particles with densities lower than that of the steel will then tend to float upwards with a terminal velocity given by Stokes' law, for a spherical particle, as

$$v = \frac{2gr^2}{9\eta}(\rho_s - \rho_p) \tag{6.2}$$

where g is the gravitational constant, r is the radius of the particle, η is the coefficient of viscosity for the steel—$\sim 5 \times 10^{-3}\,N\,s\,m^{-2}$ @ 1750–2000K (Brandes, 1983)—and ρ_s and ρ_p are the densities of the steel and particle respectively (Rodriguez, 1982). Thus for a $5\,\mu m$ TiN particle, $v = 10\,\mu m\,s^{-1}$. If the weld pool is molten for, say, 5s, then the particle will travel only $50\,\mu m$. Consequently, such particles do not have time to float out of weld pools in which they are already incorporated, hence can remain to provide nucleation sites.

6.4 - Discussion

The experiments presented in Sections 6.2 and 6.3 have demonstrated further that TaN inoculants can be used to grain refine austenitic stainless steel welds—both autogenous and with filler material—providing the level of addition is sufficient to allow nucleant particles to survive in the melt.

However, this criterion places limitations on the usefulness of introducing the required inclusions via powder fluxes, despite the method being cheap, fast, and simple to perform.

The problem arises because every weld geometry and procedure produces a different A_p/V_w ratio. Consequently for a given flux coverage the wt% addition of TaN—hence the number density of nucleation sites and degree of refinement attained—varies between different deposits.

Table 6.5 lists in ascending order the A_p/V_w ratio, the wt% addition of TaN (x_{TaN}), the number of TaN inclusions per unit volume (N_V), and the resultant degree of grain refinement for S2, S4, S6, S8 and the original TaN inoculated weld reviewed in Section 5.4.5 (Weld A). For S2 and S4, A_p/V_w is such that the addition of TaN is not sufficient for particles to remain stable in the melt, thus no refinement ensues. As the ratio increases, it becomes more favourable for TaN inclusions to survive. Higher degrees of grain refinement are thus attained.

Table 6.5 - Effect of A_p/V_w on the level of addition and thus degree of grain refinement attained for the TaN inoculated welds presented in Chapters 5 and 6.

Weld	A_p/V_w	x_{TaN} (wt%)	TaN particles stable in melt	N_V (m^{-3})	Degree of refinement
S4	1.02	0.39	×	0	None
S2	1.47	0.56	×	0	None
S8	3.13	1.00	√	$1.8 \pm 0.4 \times 10^{14}$	Mild
Weld A	3.77	1.23	√	$3.2 \pm 0.3 \times 10^{14}$	Strong
S6	6.88	2.00	√	$6.0 \pm 0.3 \times 10^{15}$	Strong

For welds in which A_p/V_w is low, a seemingly obvious method of raising the TaN addition to the level required for grain refinement would be to use flux mixed to a more viscous consistency, thereby giving a higher mean coverage. However, there is a practical drawback to this suggestion. When flux is applied to plate, only a thin layer adheres to the surface well. During welding over thick layers shielding gas from the TIG unit blows away excessive flux.

Ideally the required degree of grain refinement should be achieved from a minimal TaN addition (Section 2.4). Thus if A_p/V_w is too high, the weld may become undesirably oversaturated with inoculant.

Consequently, a method of inoculation is required which gives a more consistent level of TaN addition regardless of weld geometry and procedure. The most practical way to achieve this would be to use welding consumables alloyed such that the necessary quantity of TaN nucleants precipitate within the steel. Provision of nucleants in this manner has led to successful

grain refinement of magnesium, aluminium and ferritic stainless steel welds, and is the standard technique employed. However, further work is needed to verify that Ta and N alloying additions to austenitic stainless steels will facilitate TaN precipitation and subsequently induce grain refinement.

6.5 - Summary

It has been confirmed that TaN is a potent nucleant for austenite during solidification. However, grain refinement of austenitic stainless steel welds by inoculation with TaN powder fluxes is inconsistent. This is because every weld geometry and procedure gives a different A_p/V_w ratio, meaning each deposit receives a different level of TaN addition. The use of alloyed filler material should alleviate this problem.

The use of TaN flux during welding leads to enhanced penetration, the effect becoming more prominent with increased heat input. The phenomenon also occurs when A-TIG welding, but the proposed mechanism for this does not concur with the observations made when using TaN flux. Comparison with results when alloyed welding consumables are employed would reveal whether the effect of TaN arises because of flux interaction with the arc or through weld pool flow alterations produced by dissolved Ta and N.

Comparison between the present experiments and previous work also suggests that the density of inoculant compounds is important if additions are made via the use of powder fluxes. Compounds with densities lower than that of the steel float on the weld pool surface, thus do not become incorporated into the melt to provide nucleation sites. On the other hand, TaN is effective as it has a much higher density than steel.

Chapter 7 - Extended inoculant selection and accompanying welds

7.1 - Introduction

Experiments have shown that TaN and, to a lesser extent, HfC particles nucleate austenite via the intended mechanism of providing inert heterogeneous nucleation sites (Section 5.4.5). The results were in accordance with predictions made in Chapter 4, whereby potentially effective inoculant compounds were selected on the basis that they satisfied the criteria of close lattice matching with austenite and low solubility in molten steel. However, four other species identified in the same manner—Al_2O_3, HfO_2, SiO_2 and ZrO_2—did not behave as predicted (Section 5.4.2). Furthermore, inoculation with Si_3N_4, which failed to satisfy the solubility criterion, unexpectedly led to significant grain refinement (Section 5.4.4).

Clearly an extension to the inoculant selection procedure is thus required. Fortunately, observations and further investigations made during analysis of the welding experiments detailed in Chapters 5 and 6 have highlighted additional factors which need to be considered when attempting to predict effective nucleants for a given phase.

7.2 - Extended inoculant selection

7.2.1 - Additional factors

Further to the disregistry and solubility criteria discussed in Chapter 4, potentially effective nucleant compounds must also fulfil the following requirements:-

i) Electrostatic considerations

A good nucleant must have a similar bond type and strength to the nucleated solid to allow the electrochemical potentials either side of the interface to equate (Section 5.4.2). To nucleate austenite, compounds are thus required to exhibit primarily metallic conductivity and have a low electrical resistivity at the steel solidification temperature.

ii) Chemical reactions

The nucleation of austenite by Si_3N_4 appears to be stimulated by a chemical reaction (Section 5.4.4). However, the exact mechanism by which this occurs is unclear. For the purposes of identifying compounds to act as inert heterogeneous nucleation sites, chemical reactions with steel will thus be regarded as undesirable.

iii) Density

The autogenous welding experiments discussed in Section 6.3 suggest that if inoculant additions are made using powder fluxes, the density of the compound must be higher than that of the steel for it to become incorporated into the weld pool and hence provide potential nucleation sites.

7.2.2 - Compounds subject to investigation

The original selection procedure in Chapter 4 was applied to compounds of elements within transition metal groups IV, V and VI. A new series of compounds had to be established to which the modified process could be applied. As low solubility was a requirement, an approach was made based on the hypothesis that the solubility of a compound in steel correlates with its heat of formation, ΔH_f (Porter and Easterling, 1992). For example, TiN has a low heat of formation ($-338\,\mathrm{kJ\,mol^{-1}}$ at 298 K) and is known from the literature to exhibit low solubility in steel (Section 3.3.6). In general, for transition metals the trend is that ΔH_f of particular compound types, *e.g.* metal-nitrides, increases from left to right across a period and decreases down a group (Fig. 7.1). Thus group III and rare-earth compounds are likely to exhibit low solubilities in liquid steel. However, of the rare-earth elements, complete sets of the necessary data were only available for Ce compounds. The compounds investigated using the extended nucleant selection procedure are listed in Table 7.1.

Table 7.1 - Compounds to which the extended selection procedure was applied.

Element	Boride	Carbide	Nitride	Oxide
Ce	CeB_6	Ce_2C_3	CeN	CeO_2
La	LaB_6	La_2C_3	LaN	La_2O_3
Sc	ScB_2	Sc_2C_3	ScN	Sc_2O_3
Y	YB_2	Y_2C_3	YN	Y_2O_3

Fig. 7.1 - ΔH_f at 298 K of transition metal nitrides
(Barin and Knacke, 1973; Horovitz, 1975; Barin *et al.* 1977).

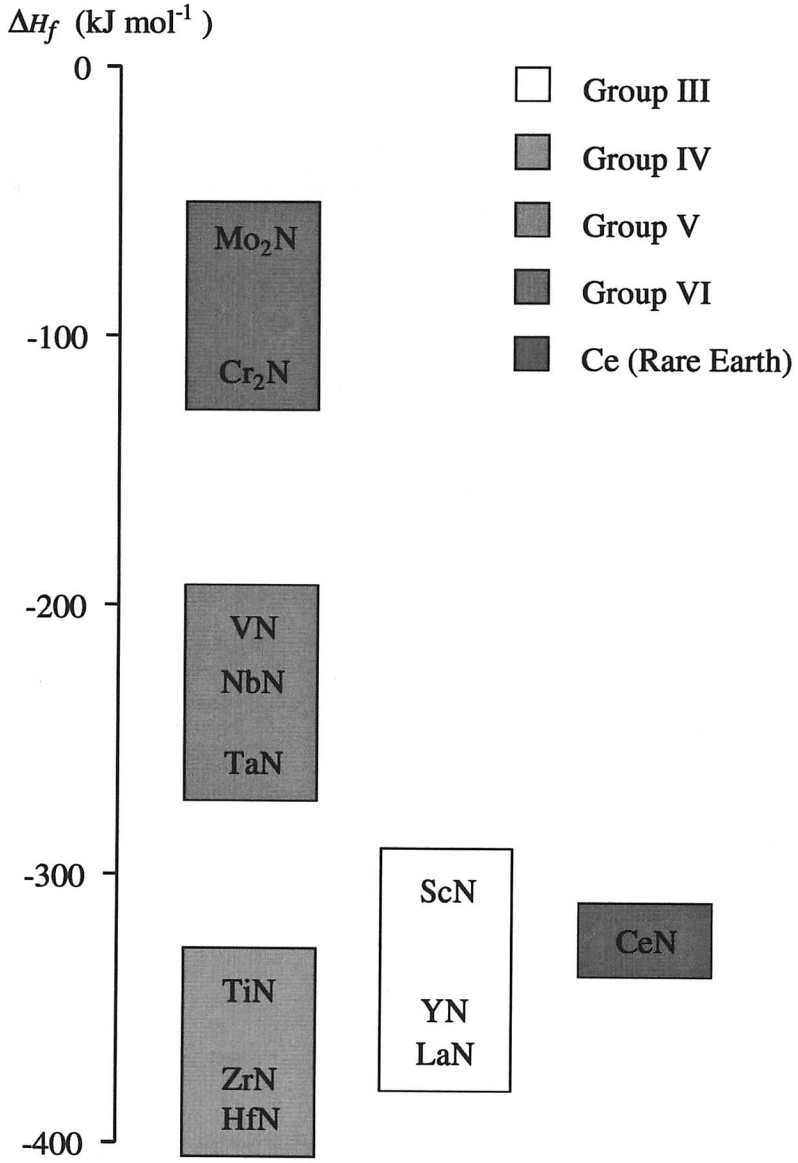

Fig. 7.2 - Solubility products in at% of Sc_2C_3, CeN and YN in molten austenitic stainless steel as a function of temperature, compared with that of TiN.

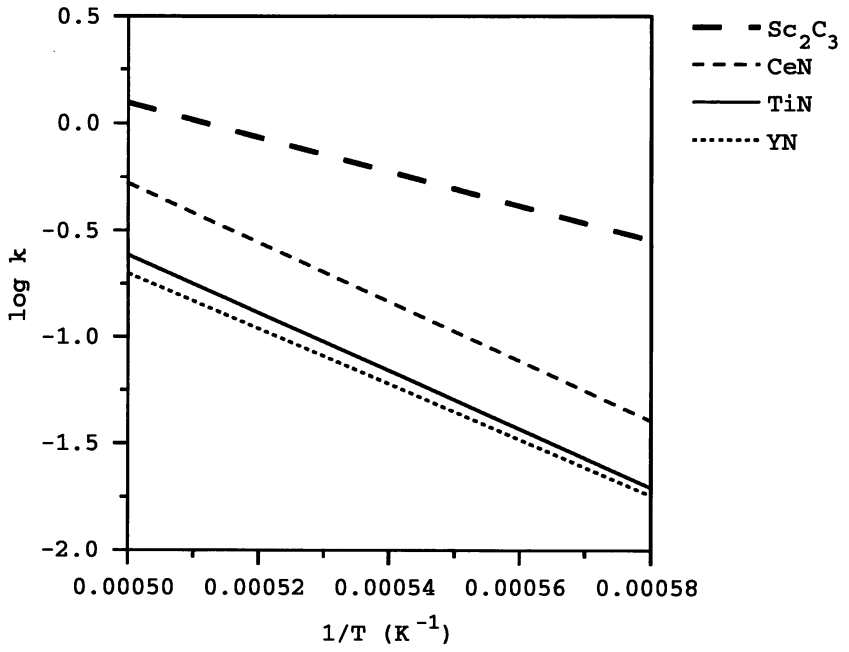

7.2.3 - Results

i) Disregistry calculations

The disregistry between each compound and austenite was calculated following the method presented in Section 4.2. Where this was less than 10%, compounds were deemed to have satisfied the lattice matching criterion for a potent nucleant. These compounds, their lowest disregistry with austenite, and the corresponding orientation relationship are given in Table 7.2.

Table 7.2 - Compounds exhibiting low disregistries with austenite.

Compound	Lattice type	Disregistry (%)	Orientation relationship
Sc_2C_3	bcc	0.07	$(100)_m \parallel (100)_s$, $[001]_m \parallel [001]_s$
CeN	fcc	1.38	$(100)_m \parallel (100)_s$, $[011]_m \parallel [001]_s$
YN	fcc	4.21	$(100)_m \parallel (100)_s$, $[011]_m \parallel [001]_s$
CeO_2	fcc	6.28	$(100)_m \parallel (100)_s$, $[011]_m \parallel [001]_s$
Sc_2O_3	bcc	3.31	$(100)_m \parallel (100)_s$, $[011]_m \parallel [001]_s$
Y_2O_3	bcc	1.81	$(100)_m \parallel (100)_s$, $[001]_m \parallel [001]_s$

ii) Solubility calculations

The temperature dependent equilibrium solubility products for the compounds in Table 7.2 were determined with MTDATA using the method outlined in Section 4.3. The three oxides were found to be insoluble over the temperature range 1900–1750 K. Table 7.3 lists the values for Sc_2C_3, CeN and YN. Fig. 7.2 illustrates more clearly the relative thermodynamic stabilites of these compounds compared with TiN, known from the literature to exhibit low solubility in molten stainless steel (Section 3.3.6). CeN and YN appear to display acceptably low solubility. Conversely, the solubility of Sc_2C_3 is significantly higher, hence undesirably excessive additions may be required for such particles to remain stable in the melt.

iii) Electrostatic considerations

CeO_2, Sc_2O_3 and Y_2O_3 are all excellent insulators, with electrical resistivities in the order of 10^7–10^8 ohm cm at the steel solidification temperature (Ryshkewitch, 1960; Brook, 1991). Wetting of steel on these compounds would not be favoured. CeN and YN, however, both exhibit

primarily metallic conductivity and have low electrical resistivities at elevated temperatures—10^{-2}–10^{-1} ohm cm (Brook, 1991)—which would facilitate the charge redistribution necessary for the nucleation of austenite. No data were avaliable for Sc_2C_3.

Table 7.3 - MTDATA calculated solubility products in at%.

Compound	Solubility
Sc_2C_3	$\log k = (-8018/T) + 4.1$
CeN	$\log k = (-13955/T) + 6.7$
YN	$\log k = (-13004/T) + 5.8$

iv) Chemical reactions

No chemical reactions have been reported between steel and the six compounds from Table 7.2. As desired, all should thus remain inert if added to the melt.

v) Density

The densities of the six compounds are given in Table 7.4. CeN and YN have higher densities than steel, thus would be expected to sink into the weld pool and provide potential nucleation sites if added as powder flux.

Table 7.4 - Room temperature densities of steel and potential nucleants.

Material	ρ_{298K} ($g\,cm^{-3}$)
Steel	7.8
Sc_2C_3	4.5
CeN	10.4
YN	8.2
CeO_2	7.2
Sc_2O_3	3.8
Y_2O_3	5.0

vi) Summary

Of the six compounds in Table 7.2 which satisfied the initial criterion of close lattice matching with austenite, only CeN and YN fulfilled all four of the subsequent requirements for a potent nucleant. The results are summarised in Table 7.5.

Table 7.5 - Summary of results from the extended nucleant selection process. All six compounds satisfied the disregistry and chemical reaction criteria.

Compound	Solubility	Electrostatics	Density
Sc_2C_3	×	?	×
CeN	√	√	√
YN	√	√	√
CeO_2	√	×	×
Sc_2O_3	√	×	×
Y_2O_3	√	×	×

7.3 - Welding experiments

7.3.1 - Experimental design

CeN and YN were not commercially available, so 1 g of each powder (particle size $<5\,\mu$m, purity >99%) was supplied by the Department of Chemistry, Cornell University, Ithaca, New York, having been prepared via the method presented by Niewa *et al.* (1998). Because of the limited quantities of inoculant, additions were made to small scale welds.

Full penetration autogenous welds were made across coupons of austenitic stainless steel plate (composition in Table 2.1) cut to 80 × 50 × 2 mm. Inoculant powder flux was mixed and applied to the plate as described in Section 5.2.1. To prevent oxidation of the bottom surface of the weld metal, the rig included a groove in the specimen stage through which back-shielding gas was passed at regulated pressure to keep the weld pool flat and avoid sagging. A mechanised TIG unit was used to complete the welds under the conditions given in Table 7.6.

Four welds were made; a control and TaN, CeN, YN inoculated, designated E1–E4 respectively. The TaN inoculated weld was included for further comparison, the compound having already been established as an effective nucleant for austenite.

Table 7.6 - Welding parameters.

Current	100 A (d.c. negative)
Voltage	10 V
Weld speed	150 mm min^{-1}
Heat input	0.24 kJ mm^{-1}
Electrode	2% thoriated tungsten
Shielding gas	Argon
Gas flow rate	10 l min^{-1}

7.3.2 - Results

The microstructures of the four welds are illustrated in Fig. 7.3. E2 shows extensive grain refinement as a result of the TaN addition. The microstructures of E3 and E4, however, are identical to the control, i.e. wholly columnar with no trace of refinement. The as-welded surfaces of E1 and E2 were clean and even (Fig. 7.4a–b). Conversely, E3 and E4 were covered with surface layers of slag (Fig. 7.4c–d).

SEM and EDX analyses revealed that all four welds contained MnS inclusions. Polyhedral inclusions pertaining to TaN were also present in E2. No CeN/YN inclusions or dissolved Ce/Y were apparent in E3 and E4 respectively. The compositions of the slag layers from E3 and E4 are given in Table 7.7. In both cases the analyses corresponded to oxygen-rich compounds.

Table 7.7 - Typical measured compositions in wt% from slag layers covering CeN and YN inoculated deposits.

Weld	Ce	Y	La	N	O
E3	80.2	0	0.4	1.4	18.0
E4	0	78.5	0	1.6	19.9

Fig. 7.3 - Plan views of the microstructures of full penetration welds (a–d) E1–E4.

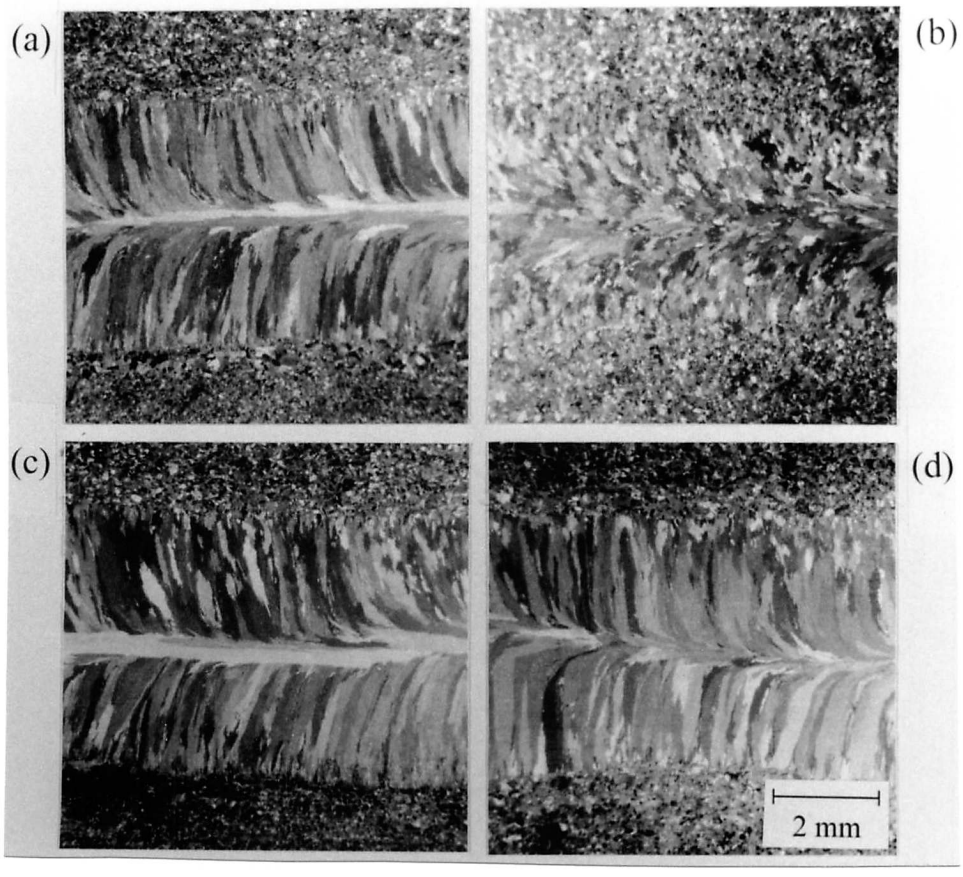

Fig. 7.4 - As-welded surfaces of E1–E4.

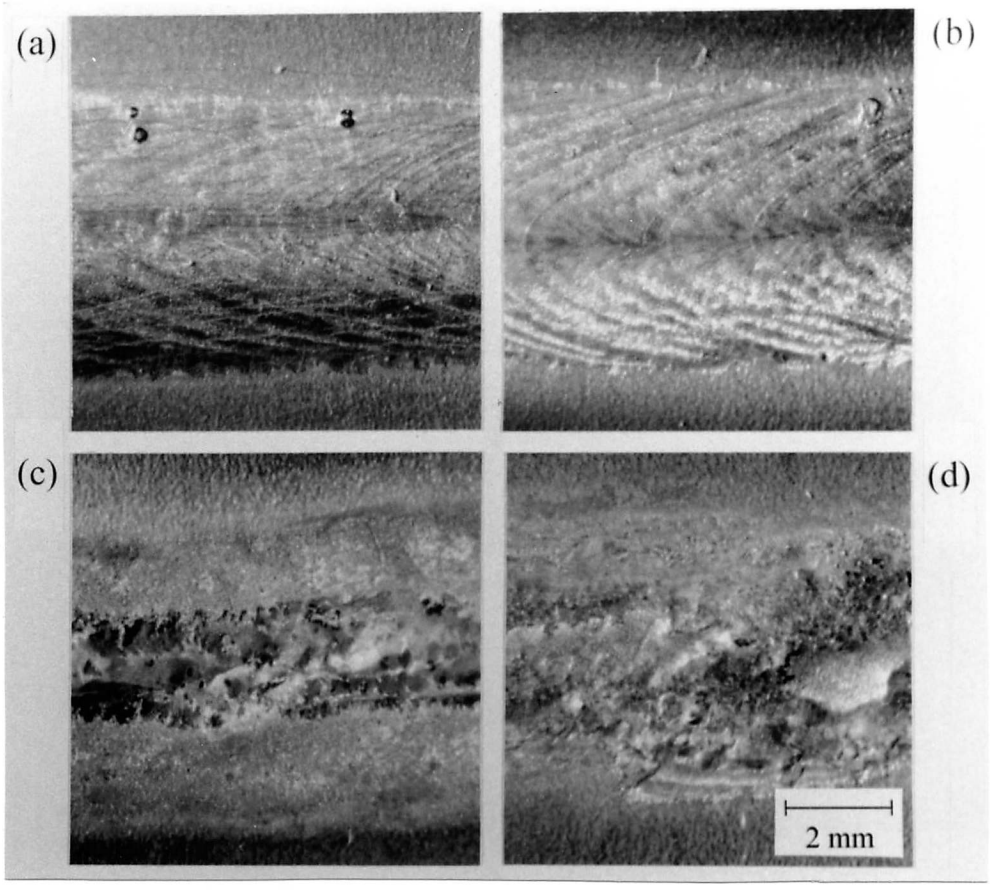

7.4 - Discussion

As in previous experiments TaN particles were incorporated into the weld pool and induced grain refinement. However, this was not the case for CeN and YN additions even though they satisfy the extended criteria for a potent nucleant. Chemical analysis of the slags covering the CeN and YN inoculated welds leads to an explanation for this anomalous behaviour. Rather than indexing as nitrides, they instead appear to be predominantly oxides of Ce and Y (Table 7.7).

CeN and YN are both stable at room temperature. However, during welding the flux covered plate ahead of the weld pool increases in temperature due to heat flow away from the arc. At these elevated temperatures it is apparent that CeN and YN readily oxidise.

The oxides of Ce and Y have lower densities than steel, and do not exhibit electrical properties conducive to wetting by the steel (Section 7.2.3). Consequently the oxidised inoculants were not incorporated into the melt and instead floated on the weld pool surface resulting in the observed slags.

The oxidation of YN and CeN fluxes is further illustrated by a colour change upon heating (Table 7.8). Fig. 7.5a–b shows YN and CeN fluxes as applied to stainless steel plate. The same samples after heating to ~400 °C for 10 s are shown in Fig. 7.5d–e. In contrast TaN flux remains unaffected by heat (Figs. 7.5c and 7.5f).

Table 7.8 - Colour changes in inoculant fluxes upon heating the substrate steel plate.

Compound	Before	After
YN	Dark brown	Off-white
CeN	Golden yellow	Off-white
TaN	Dark grey	Dark grey

Thus although CeN and YN do not react with steel—a stipulated criterion for the provision of inert nucleation sites—they do undergo a chemical reaction associated with the welding environment. Hence if inoculant additions are to be made via the use of powder fluxes, investigation of such properties is another crucial consideration for the prediction of effective nucleants.

Fig. 7.5 - Effect of heat on inoculant powder fluxes. (a–c) YN, CeN and TaN respectively as applied to stainless steel plate. (d–f) Samples after heating to $\sim 400\,^{\circ}\mathrm{C}$ for 10 s.

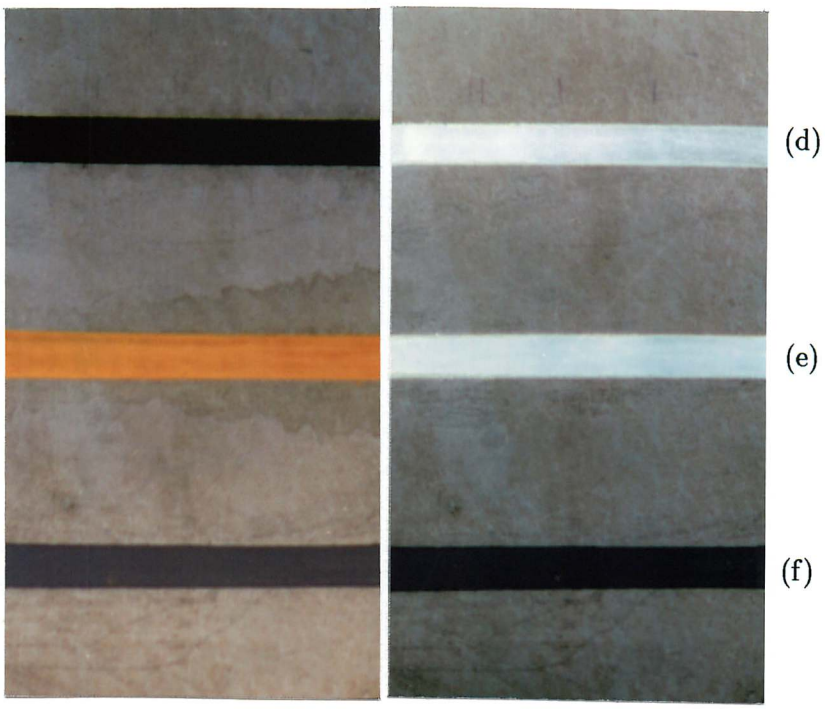

Fig. 7.6 - Proposed introduction of CeN/YN inoculant powder from within the gas shroud surrounding the weld pool.

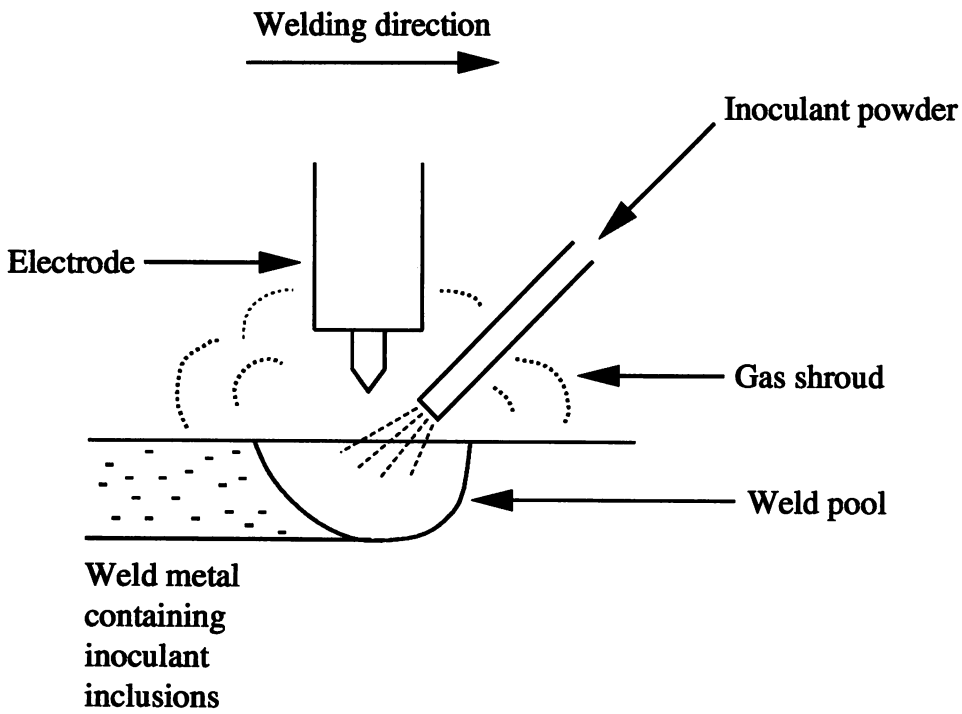

Fig. 7.7 - Results of MTDATA calculations. (a) and (b) illustrate that oxygen and sulphur combine preferentially with Ce and Y alloying additions. (c) In contrast, Ta has a weak affinity for these elements, which are instead bound by Mn.

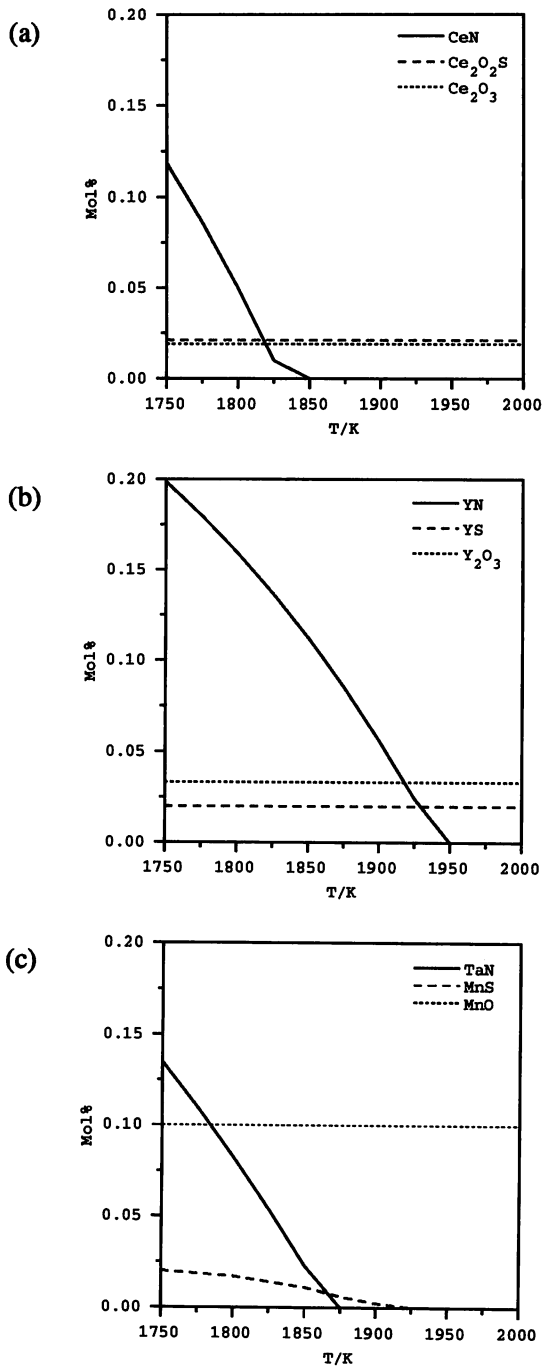

However, if the method of inoculation is altered it may yet prove possible to nucleate austenite on CeN and YN particles. For example, if the inoculant powder is introduced from within the gas shroud surrounding the weld pool then its oxidation may be prevented (Fig. 7.6).

As discussed in Section 6.4, though, it may be more desirable to produce alloyed welding consumables in which the required nucleants precipitate within the steel. In this way more consistent nucleant contents can be achieved regardless of weld geometry and procedure. Internally precipitated CeN and YN particles would also be shielded from oxidation.

It is well known, though, that Ce has preferred affinities for certain minor alloying elements in steel, chiefly oxygen and sulphur (Banks and Gladman, 1979; Luyckx *et al.* 1970; Wilson *et al.* 1974; Wilson and Wells, 1973). The required CeN precipitation may thus be impaired by the presence of such elements within austenitic stainless steels.

MTDATA calculations were performed to examine precipitation sequences in a hypothetical Ce-alloyed austenitic steel. Corresponding investigations of Y- and Ta-alloyed material were also made for comparison. The composition of the steel in at% is given in Table 7.9. 0.4 at% additions of Ce/Y/Ta and N are similar to the levels provided by powder flux inoculation of welds throughout this study. By weight, the oxygen and sulphur contents are equivalent to 250 and 100 ppm respectively. Mn is included because it is the usual oxide/sulphide former for AISI 300 series austenitic steels (Porter and Easterling, 1992).

Table 7.9 - Composition of steel in at% for inclusion stability calculations.

Fe	Cr	Ni	Mn	C	N	O	S	Ce/Y/Ta
to bal.	20	10	1.5	0.4	0.4	0.1	0.02	0.4

The thermodynamic stability of inclusions was studied within the liquid steel phase. Potential inclusion phases for the Ce-, Y- and Ta-alloyed cases in turn are listed in Table 7.10. MnO and MnS were also included in each calculation.

The calculations demonstrated that in steel Ce and Y have higher affinities for oxygen and sulphur than for nitrogen, and that their affinity for oxygen and sulphur is stronger than that of Mn. For Ta the opposite are true. Fig. 7.7a–b shows that in Ce- and Y-alloyed steels, even at very high temperatures all oxygen and sulphur combines with the addition. The concentration of Ce/Y in the liquid is thus reduced. However, because Ce/Y is present in excess of oxygen and sulphur, substantial quantities remain unbound and available for nitride

formation. Conversely, no oxygen or sulphur binds with Ta; instead Mn oxides/sulphides form (Fig. 7.7c). TaN formation is therefore completely unimpeded.

Thus in theory precipitation of the desired CeN and YN particles within austenitic stainless steel could be achieved. Welding experiments utilising such material may then be performed to establish whether the species do act as effective nucleants for austenite as predicted.

Table 7.10 - Additional phases included for calculations on Ce-, Y- and Ta-alloyed steels.

Ce-alloyed	Y-alloyed	Ta-alloyed
CeN	YN	TaN
Ce_2C_3	Y_2C_3	TaC
Ce_2O_3	Y_2O_3	Ta_2O_5
CeO_2	YS	TaS_2
Ce_2O_2S		
Ce_2S_3		
Ce_3S_4		
CeS		

7.5 - Summary

An extended selection procedure encompassing lattice matching, solubility, electrostatic considerations, chemical reactions with steel and density criteria predicted CeN and YN to be effective nucleants for austenite.

Unfortunately, grain refinement of austenitic stainless steel welds was not achieved via inoculation with CeN or YN powder fluxes due to oxidation of the compounds. In contrast TaN—established as a potent nucleant for austenite—is unaffected by this problem. Thus if inoculant additions are to be made in this manner, then potential compound interactions with the welding environment must also be investigated.

However, theoretical studies have illustrated that CeN and YN particles could be precipitated within steels as a result of alloying additions, and hence provide potential nucleation sites for austenite.

Chapter 8 - Multipass welds and ultrasonic tests

8.1 - Introduction

The ultimate aim of this project was to determine a method of grain refining austenitic stainless steel welds to eliminate the coarse columnar microstructure which forms in multipass joints due to epitaxial growth and subsequently prevents satisfactory ultrasonic inspection by disrupting sound wave propagation.

Single pass welding experiments (Chapters 5–7) confirmed TaN to be a particularly effective nucleant for austenite during solidification, via the intended mechanism of inoculant particles within the melt providing inert heterogeneous nucleation sites.

A multipass welding experiment was thus performed to ascertain whether TaN inoculation would interrupt continuous grain growth between successive passes. Ultrasonic tests were then carried out to quantitatively measure the effect of any grain refinement on sound wave propagation.

8.2 - Multipass welding experiments

8.2.1 - Experimental design

Control (M1) and TaN inoculated (M2) multipass welds were constructed as follows. Coupons of austenitic stainless steel (composition in Table 2.1) $100 \times 100 \times 12$ mm were machined with a 60° single bevel and a 1 mm root face preparation along one of the 100 mm sides on each. Pairs were then butt-welded together by seven passes, each performed using a mechanised TIG unit under the conditions given in Table 5.3. TaN inoculant flux was mixed as described in Section 5.2.1 and applied in ~1 cm wide strips prior to each pass of M2.

8.2.2 - Results

Transverse cross-sections of M1 and M2 are shown in Fig. 8.1. In the control weld columnar grains can be seen growing continuously through successive passes. In contrast, TaN inoculation has produced significant interruptions. Plan views taken at the levels indicated in Fig. 8.1 further illustrate the elimination of the columnar structure in M2 (Fig. 8.2).

Fig. 8.1 - Transverse cross-sections of (a) M1 and (b) M2.

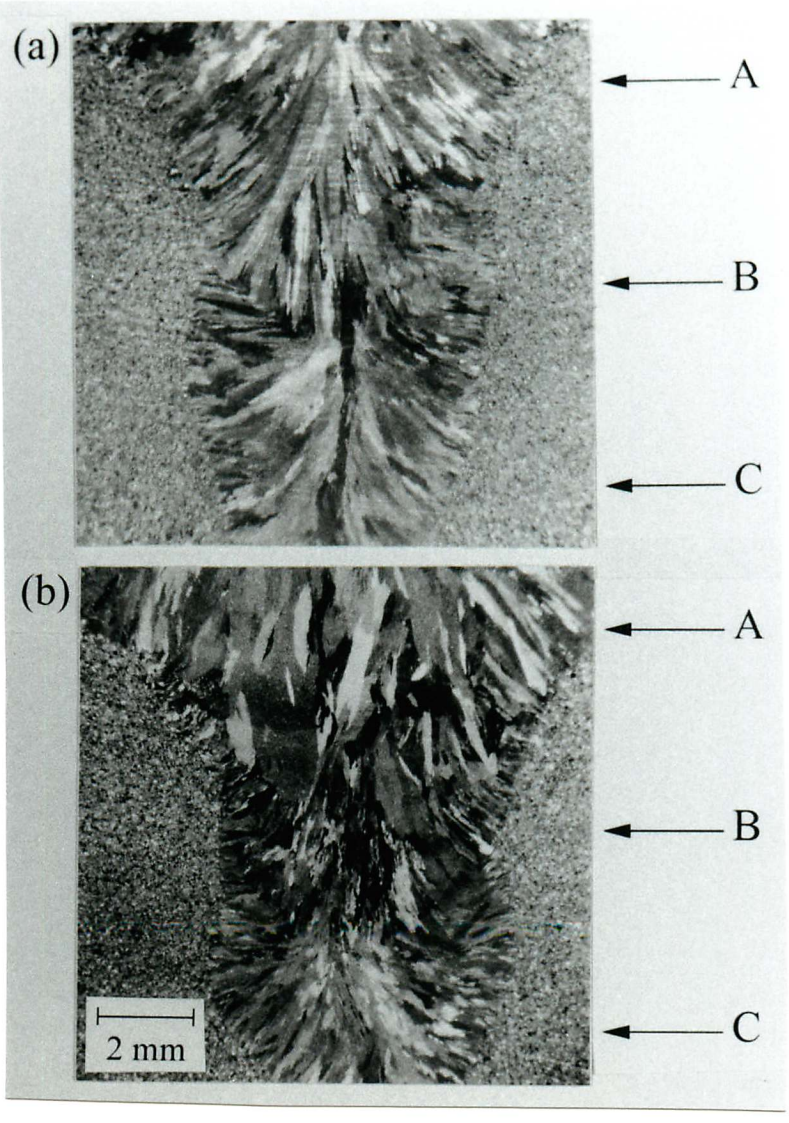

Fig. 8.2 - Plan views at levels indicated in Fig. 8.1.
(a–c) M1 and (d–f) M2 at levels A, B, and C respectively.

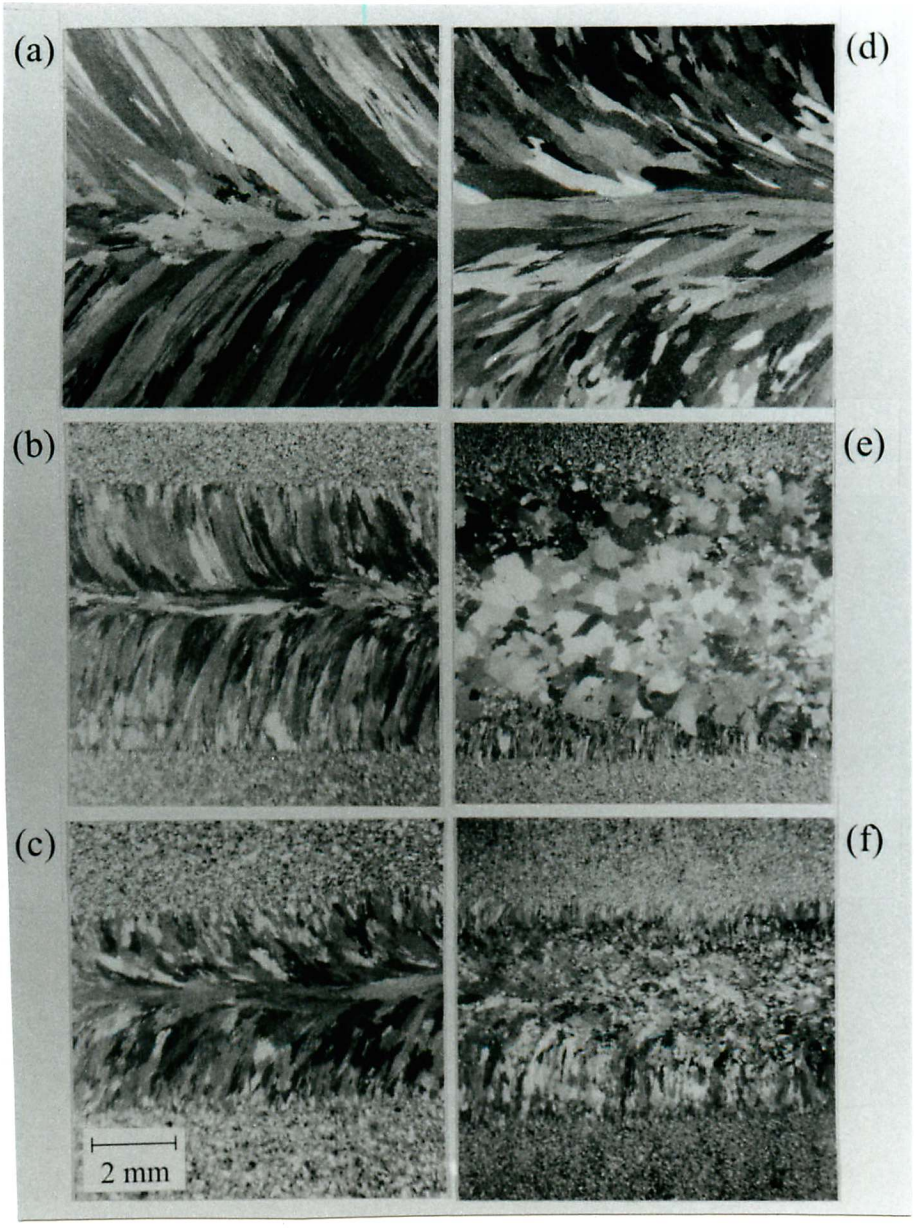

Fig. 8.3 - Appearance of δ-ferrite network in (a) M2 lower portion, (b) M2 upper portion and (c) throughout M1. Note TaN inclusions also apparent in both portions of M2.

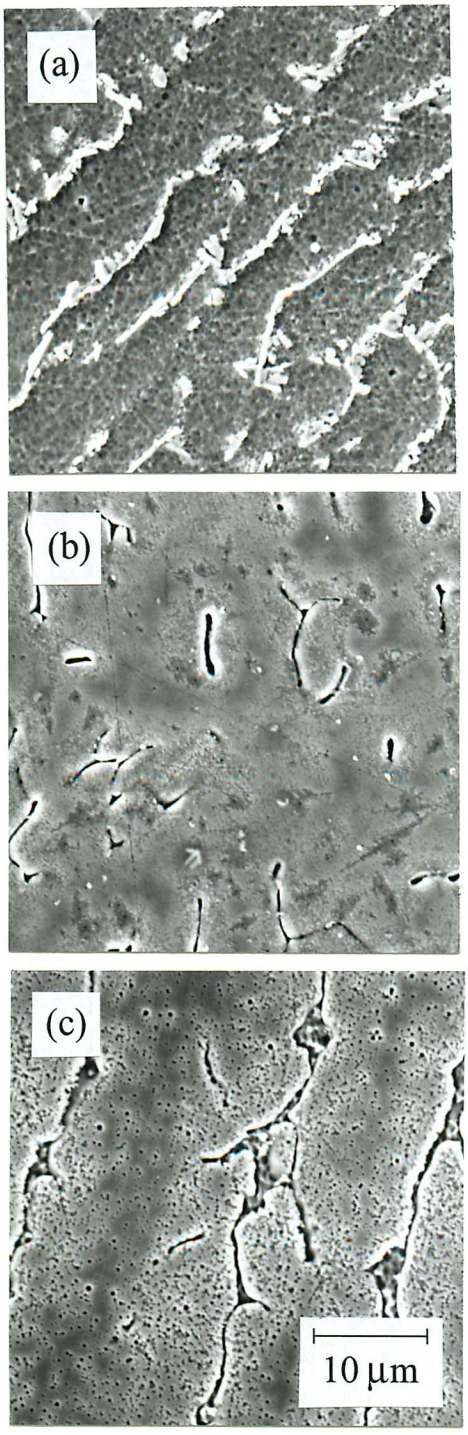

SEM and EDX analyses revealed that both deposits contained globular MnS inclusions. Polyhedral inclusions pertaining to TaN were present throughout M2. Electron microscopy also showed the appearance of the δ-ferrite network to be markedly different in the lower portion of M2 compared with both the upper portion and M1 (Fig. 8.3). The measured compositions of δ-ferrite from each of these cases are given in Table 8.1.

Table 8.1 - Measured compositions in wt% of δ-ferrite within multipass welds.

Weld	Fe	Cr	Ni	Mn	Mo	Si	P	S	Ta
M1	69.4	23.3	5.8	0.8	0.2	0.5	0.02	0.01	0.0
M2 Upper	68.6	23.0	6.4	0.7	0.2	0.5	0.02	0.01	0.6
M2 Lower	61.4	20.8	5.0	0.5	0.2	0.4	0.02	0.01	11.7

8.2.3 - Discussion

It is clear that TaN inoculation generates significant grain refinement in multipass austenitic welds, preventing the formation of undesirable continuous columnar grains. However, the degree of refinement achieved varies throughout the joint, being more pronounced in the lower portion.

Weld pool volume is directly proportional to heat input and inversely proportional to welding speed (David and Vitek, 1989). These parameters were identical for each pass, thus each pass produced a weld pool of approximately the same volume. However, the vee-butt geometry caused the pool shape and heat flow characteristics to differ between each pass. A schematic comparison between the upper and lower passes is shown in Fig. 8.4.

In the upper passes weld pools were subjected to a larger heat sink, thus cooled more rapidly (Granjon, 1991). Faster cooling is usually expected to produce a finer grain size, but in this case the opposite was apparent.

Because the weld pools in each pass were of equal volume, the use of a constant width strip of inoculant flux should have ensured consistent levels of addition. Approximately equal numbers of TaN particles were therefore introduced to each pass. The grain size of each deposit varied significantly though, hence so too did the nucleation efficiency.

It is well established that in welding, nucleation efficiency—and hence the degree of refinement attained—is strongly dependent on the G_L/R ratio (David and Vitek, 1989). A low G_L/R ratio promotes the formation of equiaxed structures (Section 3.2.6).

Fig. 8.4 - Comparison between weld pool shape and heat flow characteristics of (a) upper pass and (b) lower pass.

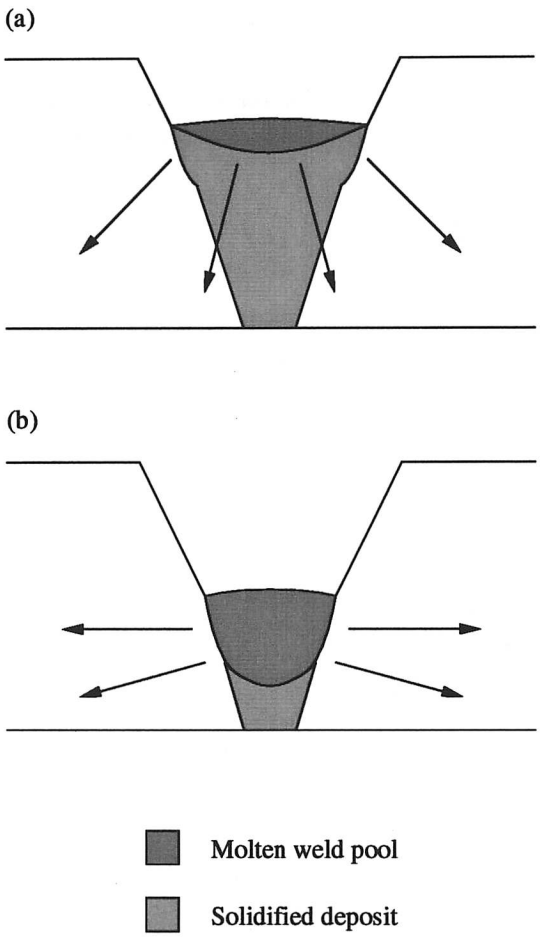

In the multipass joint, changes in pool shape and heat flow characterisitcs would inevitably have produced different G_L/R values throughout each weld pool. Unfortunately, it is not possible to give a quantitative measure of G_L/R for each case. However, from the observed degree of refinement it can be inferred that G_L/R increased with successive passes, and that the parameter was more influential in determining microstructural development than cooling rate.

Fortunately, it may be possible to overcome the unfavourable solidification conditions within the upper passes by increasing the level of TaN addition. This would raise the number density of potential nucleation sites, which is known to enhance the achievable degree of grain refinement (Fig. 3.9; Section 6.4).

Another phenomenon was also apparent in the TaN inoculated multipass weld, namely the unusual appearance of the δ-ferrite network in the lower portion of the joint. Fig. 8.3a shows the phase to be lighter than and in relief of the surrounding austenite, whereas in both the upper portion (Fig. 8.3b) and the control weld (Fig. 8.3c) δ-ferrite appears as dark pits having been preferentially attacked during etching.

The appearance of δ-ferrite in the lower portion of M2 is akin to that of the TaN inclusions. As microanalysis confirmed it to be rich in Ta (Table 8.1), it is most probable that δ-ferrite in this part of the joint is coated in TaN precipitated during reheating of the initial deposits by subsequent weld passes. TaN is not attacked by acids thus during etching protected the δ-ferrite beneath from corrosion giving rise to its unusual appearance.

This hypothesis is corroborated by further EDX analysis (Table 8.2). As well as TaN inclusions, the upper portion of M2 contains a significant amount of dissolved Ta as a result of inoculation. However, in the lower portion dissolved Ta is virtually absent, presumably having been removed from solution via the proposed recombination with nitrogen.

Table 8.2 - Concentration of dissolved Ta in M2.

Weld portion	Ta concentration (wt%)
Upper	0.70 ± 0.04
Lower	0.05 ± 0.02

8.3 - Ultrasonic tests

Simple ultrasonic tests were performed on the multipass welds M1 and M2 to investigate changes in sound beam propagation as a result of microstructural differences between the two deposits (Fig. 8.5).

Pulse-echo traces were recorded on a Krautkramer USM-2 ultrasonic detector as the transmitter/receiver probe was moved across each weld using a 2 MHz sound beam calibrated for stainless steel (velocity=6000 m s^{-1}, wavelength=3 mm) with constant pulse energy and amplification. The weld surfaces were ground flat to give 10 mm thick blocks and coated with an ultrasonic couplant gel. A fixed weight of 1 kg was attached to the probe to ensure equal contact in each case. The intensity of the returning sound thus gave a quantitative measure of the degree of attenuation due to interactions between the sound beam and the microstructure (Krautkramer and Krautkramer, 1969).

The results are shown in Fig. 8.6. Each trace shows the intensities of successive backwall echoes. Intensities were highest over the plate, and reached a minimum over the weld centrelines. For M1, only the first backwall echo was apparent. However, for M2, three backwall echoes were visible, with the minimum recorded intensity for the first peak more than double that from M1. This demonstrates that greatly improved transmittance of ultrasound was facilitated by the refined grain structure of the TaN inoculated weld.

8.4 - Summary

It has been shown that the addition of TaN inoculant particles induces significant grain refinement and thus prevents continuous columnar growth in multipass welds of austenitic stainless steel. The degree of grain refinement attained varied throughout the deposit due to differing solidification conditions within each pass which arose from the joint geometry.

The necessity of providing sufficient additions for TaN particles to remain stable in the melt also led to appreciable quantities of dissolved Ta and N. During reheating of the initial deposits by subsequent passes these species recombined, hence TaN precipitated at δ/γ grain boundaries.

Ultrasonic experiments confirmed that the refined grain structure of the TaN inoculated multipass weld facilitated improved sound transmittance, thus the primary goal of the project was achieved.

Fig. 8.5 - Design of ultrasonic experiment.

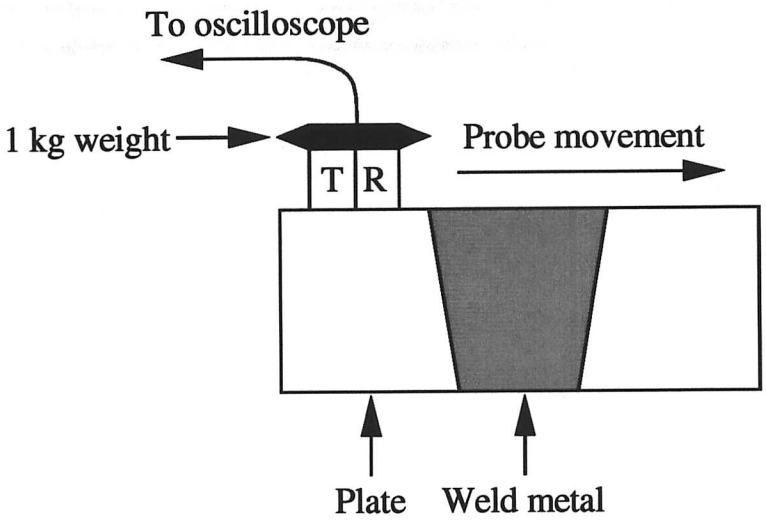

Fig. 8.6 - Results of ultrasonic tests showing intensities of backwall echoes over (a) plate, (b) M1 weld centreline and (c) M2 weld centreline.

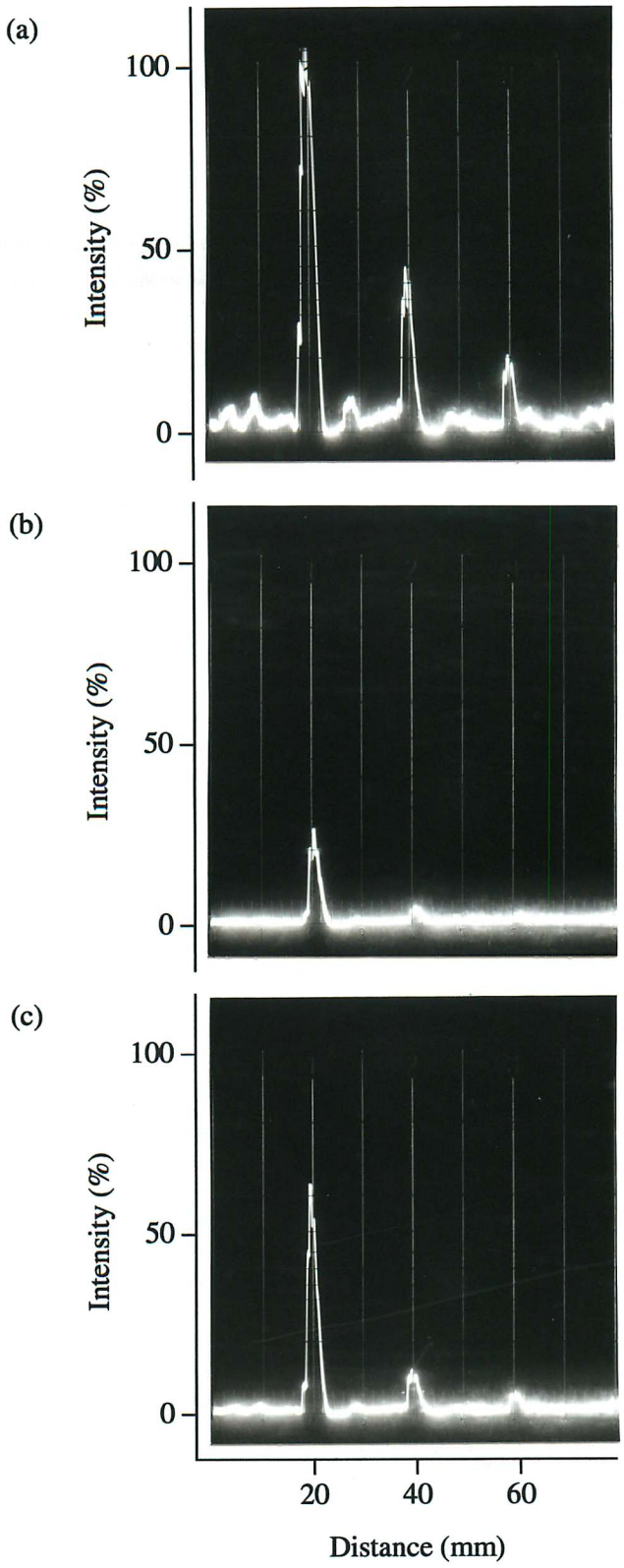

Chapter 9 - Conclusions and further work

9.1 -Conclusions

The aim of this project was to grain refine austenitic stainless steel welds to produce equiaxed microstructures that facilitate ultrasonic inspection. This may be realised by increasing the number density of crystals growing in the weld pool ahead of the solidification front such that columnar growth is stifled. Previous attempts to achieve this have involved dynamic stimulation of the weld pool to fragment the solidifying interface. However, the necessary operating parameters for grain refinement were heavily material and weld geometry dependent, thus industrial application of such methods is not practicable.

In contrast, an increased number density of crystals—hence grain refinement—in welds of magnesium, aluminium and fully ferritic stainless steel is easily achieved by the addition of certain inclusions to provide heterogeneous nucleation sites. To fulfil the aim of the current project it was thus decided to seek an effective nucleant for austenite.

From the literature and experimental results, if particles are introduced to welds using direct powder additions, it was found that six criteria had to be fulfilled for a compound to be a potent nucleant. The inoculant compound must:

i) have good lattice matching with the nucleating phase;

ii) have low solubility in the molten alloy, such that solid particles can survive in the melt to provide nucleation sites;

iii) satisfy an electrostatic criterion—in the present case to exhibit primarily metallic conductivity and have a low electrical resistivity at the steel solidification temperature;

iv) not undergo chemical reaction with the steel;

v) not undergo chemical reaction with the welding environment;

vi) have a higher density than the steel, such that particles sink into the weld pool.

TaN satisfied all of the criteria and was shown to induce grain refinement in austenitic stainless steel welds. Successful results were achieved using a number of weld geometries and procedures, including the key target of eliminating continuous columnar grain growth in a multipass weld.

A minimum level of addition— ~ 1 wt% TaN —is required for particles to be thermodynamically stable in molten austenitic steel. Above this threshold grain refinement occurs, with the degree of refinement and the nucleation efficiency dependent on the number density of inclusions and the solidification conditions as described by the ratio G_L/R in accordance with established theory.

Ultrasonic experiments demonstrated that the refined grain structure of the TaN inoculated multipass weld permits improved sound wave propagation, hence the prime objective of the project was achieved.

9.2 - Suggestions for future work

Several areas worthy of further investigation are prompted by the results of this project:

i) Consistent TaN inoculation of austenitic welds using powder fluxes is complicated because the level of addition varies as a function of the ratio between the plate area covered by flux, A_p, and the weld pool volume, V_w. The development of alloyed welding consumables in which the necessary quantity of TaN nucleants precipitate within the steel should alleviate this problem.

ii) Before they can be employed in plant service, it must be shown that TaN inoculated welds meet the corrosion resistance and mechanical property specifications set by the industry regulators, although it is worth noting some key points with regard to this matter. In general, the corrosion and mechanical behaviour of equiaxed welds is improved compared with those exhibiting a columnar microstructure, because of reduced segregation and isotropy of properties (Garland, 1974; Kou and Le, 1986). However, the composition of austenitic steels in nuclear fuel reprocessing is strictly controlled with respect to corrosion resistance. In addition to providing discrete TaN inclusions, inoculation also leads to a small change in the steel matrix composition from dissolved Ta and N. Fortunately, dissolved nitrogen is generally believed to have a beneficial impact on corrosion resistance (Stein and Menzel, 1995; Murata and Sakamoto, 1997). Furthermore, for many years AISI 347 steels containing dissolved Nb were satisfactorily employed in nitric acid environments (Gladman, 1998). Ta in solution in steels behaves almost identically to Nb (Miller, 1959), hence the dissolved Ta in inoculated welds should not present a problem. Nevertheless, extensive testing will still be required to confirm these hypotheses.

iii) A side effect of inoculation using TaN powder flux was an increase in weld penetration. The phenomenon also occurs when welding with activating fluxes, *i.e.* the A-TIG process. However, the proposed mechanism for this does not concur with the observations made when using TaN flux, hence further work is required.

iv) The ability of inoculant additions to provide heterogeneous nucleation sites must also depend on the particle size. For a given undercooling, there is a critical radius for nuclei formation. If the inclusions are too small they will not induce nucleation unless the level of undercooling increases, hence it may not be possible to form sufficient new crystals in the liquid ahead of the solidification front to suppress columnar grain growth. Alternatively, the provision of larger inoculant particles may facilitate grain refinement in cases where the level of addition is such that solid inclusions are not thermodynamically stable in the melt. This is because insufficient time may be avaliable prior to solidification for complete particle dissolution.

v) CeN and YN powder fluxes failed to induce grain refinement because during welding they oxidised before they could become incorporated into the deposit. However, if these inoculants are introduced from within the gas shroud surrounding the weld pool then their oxidation may be prevented. Theoretical studies have also shown that CeN and YN particles could be precipitated within steels as a result of alloying additions, and hence provide potential nucleation sites for austenite.

vi) Inoculation with Si_3N_4—a compound which failed to satisfy the solubility criterion for a potent nucleant—unexpectedly led to significant grain refinement of a single-pass austenitic weld. However, no direct evidence for nucleation on Si_3N_4 inclusions could be attained, hence the compound was excluded from further investigation within the present study. It would be useful to perform more experiments to provide a full explanation of its anomalous behaviour.

References

ADDINALL, E (1982): Nuclear power in perspective, Kogan Page, London

ATKINS, P. (1994): Physical chemistry, 5th edition, Oxford University Press, Oxford

BAIKIE, B., WAGG, A., WHITTLE, M. and YAPP, D. (1976): Ultrasonic inspection of austenitic welds, *Journal of the British Nuclear Energy Society*, **15**, 257–261

BAIKIE, B., WAGG, A. and YAPP, D. (1975): The relationship between the preferred crystallographic orientation in "Type 316" austenitic stainless steel weld metal and the ultrasonic attenuation coefficient, in *Texture and the properties of materials, eds. Davies, G., Dillamore, I., Hudd, R. and Kallend, J.*, The Metals Society, Cambridge

BAILEY, N. and SCOTT-LAWSON, W. (1975): The prospects for grain refinement during welding, *The Welding Institute Research Bulletin*, **16**, 289–293

BANKS, T. and GLADMAN, T. (1979): Sulphide shape control, *Metals Technology*, **6**, 81–94

BARIN, I. and KNACKE, O. (1973): Thermochemical properties of inorganic substances, Springer-Verlag, Berlin

BARIN, I., KNACKE, O. and KUBASCHEWSKI, O. (1977): Thermochemical properties of inorganic substances—Supplement, Springer-Verlag, Berlin

BERGLUND, G. (1981): Metallurgical problems in nitric acid plants and the use of special stainless steels, *Paper for presentation at the 2nd UHDE nitric acid symposium*, Dortmund, 21–23 September

BLOM, U. and KVARNBACK, B. (1975): The importance of high purity in stainless steels for nitric acid service, *Materials Performance*, **14**, 43–46

BRAGG, L. and CLARINGBULL, G. (1965): The crystalline state—Volume IV: Crystal structures of minerals, Bell & Sons Ltd., London

BRAMFITT, B. (1970): The effect of carbide and nitride additions on the heterogeneous nucleation behaviour of liquid iron, *Metallurgical Transactions*, **1**, 1987–1995

BRANDES, E. (ed.) (1983): Smithells metals reference book, 6th edition, Butterworths, London

BROOK, R. (ed.) (1991): Concise encyclopedia of advanced ceramic materials, Pergamon Press, Oxford

BURKE, J., KENYON, R., BURGHOFF, H. and HOBBS, J. (1949): Grain control in industrial metallurgy, American Society for Metals, Cleveland, Ohio

CARRICK, L., HICK, A., SALMON, S. and WAREING, A. (1985): A new technique for stainless steel pipe butt welds, *Metal Construction*, **17**, 354–358

CASTRO, R. and DE CADENET, J. (1974): Welding metallurgy of stainless and heat-resisting steels, Cambridge University Press, Cambridge

CAWLEY, J. and LEE, W. (1994): Oxide ceramics, in *Structure and properties of ceramics, ed. Swain, M.*, VCH, Weinheim

CHAMPION, F. (1964): Corrosion testing procedures, 2nd edition, Chapman and Hall, London

CHRISTIAN, J. (1975): Theory of transformations in metals and alloys, 2nd edition, Pergamon Press, Oxford

CIBLUA, A. (1949): The mechanism of grain refinement of sand castings in aluminium alloys, *Journal of the Institute of Metals*, **76**, 321–360

CIBULA, A. (1952): The grain refinement of aluminium alloy castings by additions of titanium and boron, *Journal of the Institute of Metals*, **80**, 1–16

CLARK, R., BRADLEY, D. and THORNTON, P. (1973): The chemistry of titanium, zirconium and hafnium, Pergamon Press, Oxford

CLARK, R. and BROWN, D. (1973): The chemistry of vanadium, niobium and tantalum, Pergamon Press, Oxford

COWAN, R. and TEDMON, C. (1973): Advances in corrosion science and technology—Volume 3, Plenum Press, New York

CROSSLEY, F. and MONDOLFO, L. (1951): Mechanism of grain refinement in aluminium alloys, *Journal of Metals*, **3**, 1143–1148

CROOK, C. and SHAW, R. (1979): Materials applications in the Windscale nuclear fuel reprocessing plant—Pipework, in *Welding and fabrication in the nuclear industry*, British Nuclear Energy Society, London

DAVID, S. and VITEK, J. (1989): Correlation between solidification parameters and weld microstructures, *International Materials Reviews*, **34**, 213–245

DAVID, S. and VITEK, J. (1993): Analysis of weld metal solidification and microstructures, in *Mathematical modelling of weld phenomena, eds. Cerjak, H. and Easterling, K.*, Institute of Materials, London

DAVIES, A. (1989): The science and practise of welding—Volume 2: The practise of welding, 9th edition, Cambridge University Press, Cambridge

DAVIES, G. and GARLAND, J. (1975): Solidification structures and properties of fusion welds, *International Metallurgical Reviews*, **20**, 83–106

DILLON, C. (1960): Compositional effects in corrosion of stainless steels in chemical environments, *Corrosion*, **16**, 433t–440t

EASTERLING, K. (1984): Solidification microstructure of fusion welds, *Materials Science and Engineering*, **65**, 191–198

EASTERLING, K. (1992): Introduction to the physical metallurgy of welding, 2nd edition, Butterworth-Heinemann, Oxford

EDWARDS, G. (1996): Review of ultrasonic test procedures for stainless steel weldments—Preliminary report, *TWI Report 621259/1/96*

EMLEY, E. (1966): Principles of magnesium technology, Pergamon Press, Oxford

FREDRIKSSON, H. (1972): The solidification sequence in an 18-8 stainless steel investigated by directional solidification, *Metallurgical Transactions*, **3**, 2989–2997

GANAHA, T., PEARCE, B. and KERR, H. (1980): Grain structures in aluminium alloy GTA welds, *Metallurgical Transactions A*, **11A**, 1351–1359

GARLAND, J. (1974): Weld pool solidification control, *Metal Construction*, **6**, 121–127

GILL, T. and GNANAMOORTHY, J. (1982): A method for the quantitative analysis of delta-ferrite, sigma and $M_{23}C_6$ carbide phases in heat treated Type 316 stainless steel weldments, *Journal of Materials Science*, **17**, 1513–1518

GLADMAN, T. (1988): Developments in stainless steels, *Metals and Materials*, **4**, 351–355

GLADMAN, T. (1997): The physical metallurgy of microalloyed steels, Institute of Materials, London

GLASSON, E. and EMLEY, E. (1968): Heterogeneous nucleation in the solidification of aluminium and magnesium alloys, in *Solidification of metals*, Iron and Steel Institute, London

GRANJON, H. (1991): Fundamentals of welding metallurgy, Abington Publishing, Cambridge

GREENWOOD, N. (1973): The chemistry of boron, Pergamon Press, Oxford

GREER, A., BUNN, A., TRONCHE, A., EVANS, P. and BRISTOW, D. (2000): Modelling of grain refinement by inoculation of metallic melts, submitted to *Acta Materialia*

HALDEN, F. and KINGERY, W. (1955): Surface tension at elevated temperatures—2: Effect of C, N, O and S on liquid iron surface tension and interfacial energy with Al_2O_3, *Journal of Physical Chemistry*, **59**, 557–559

HALE, G. and NUTTING, J. (1984): Overheating of low-alloy steels, *International Metals Reviews*, **29**, 273–298

HALL, E. (1951): The deformation and ageing of mild steel—III: Discussion of results, *Proceedings of the Physical Society*, **64B**, 747–753

HALMSHAW, R. (1987): Non-destructive testing, Edward Arnold, London

HAMPSHIRE, S. (1994): Nitride ceramics, in *Structure and properties of ceramics, ed. Swain, M.*, VCH, Weinheim

HASHIMOTO, S., KOBAYASHI, K. and MIURA, S. (1983): Roles of the lattice coherency to the heterogeneous nucleation in the Al-Ti system, *Zeitschrift für Metallkunde*, **74**, 787–792

HEINTZE, G. and MCPHERSON, R. (1986): Solidification control of submerged arc welds by inoculation with Ti, *Welding Journal*, **65**, 71s–82s

HEIPLE, C. and ROPER, J. (1982): Mechanism for minor element effect on GTA fusion zone geometry, *Welding Journal*, **61**, 97s–102s

HODSON, S. (1989): MTDATA—Metallurgical and thermochemical databank, National Physical Laboratory, Teddington

HONEYCOMBE, R. (1984): The plastic deformation of metals, 2nd edition, Edward Arnold, London

HONEYCOMBE, R. and BHADESHIA, H. (1995): Steels—Microstructure and properties, 2nd edition, Edward Arnold, London

HOROVITZ, C. (ed.) (1975): Scandium—Its occurrence, chemistry, physics, metallurgy, biology and technology, Academic Press, London

HUNT, J. (1984): Steady state columnar and equiaxed growth of dendrites and eutectic, *Materials Science and Engineering*, **65**, 75–83

INOUE, K., OHNUMA, I., OHTANI, H., ISHIDA, K. and NISHIZAWA, T. (1998): Solubility product of TiN in austenite, *ISIJ International*, **38**, 991–997

JONES, G. and PEARSON, J. (1976): Factors affecting the grain refinement of aluminium using titanium and boron additives, *Metallurgical Transactions B*, **7B**, 223–234

KEARNS, W. (ed.) (1978): AWS Welding Handbook—Volume 2: Welding processes, arc and gas welding and cutting, brazing and soldering, 7th edition, Macmillan Press Ltd. London

KOU, S. and LE, Y. (1986): Nucleation mechanisms and grain refining of weld metal, *Welding Journal*, **65**, 305s–313s

KRAUTKRAMER, J. and KRAUTKRAMER, H. (1969): The ultrasonic testing of materials, Allen and Unwin, London

LAKHLIFI, A., LEROUX, C., SATRE, P., DURAND, B., ROUBIN, M. and NIHOUL, G. (1995): Hafnia powders (HfO_2)—Elaboration and characterisation by transmission electron microscopy, *Journal of Solid State Chemistry*, **119**, 289–298

LANCASTER, J. (1987): Metallurgy of welding, 4th edition, Allen and Unwin, London

LANDOLT, D., MISCHLER, S., VOGEL, A. and MATHIEU, H. (1990): Chloride ion effects on passive films on FeCr and FeCrMo studied by AES, XPS and SIMS, *Corrosion Science*, **31**, 431–440

LEMAITRE, P., KOBLE, T. and DOCTOR, S. (1994): Status of the capability studies on austenitic steel welds conducted in the framework of Action 4 of PISC III, in *NDE practise and results, eds. Borloo, E. and Lemaitre, P.*, JRC, Lille

LEONARD, A. (1999): Private communication

LEONE, G. and KERR, H. (1982): The ferrite to austenite transformation in stainless steels, *Welding Journal*, **62**, 13s–21s

LI, M. and BROOKS, J. (1998): Mechanism of single centreline grain formation in titanium alloy welds, *Science and Technology of Welding and Joining*, **3**, 89–96

LUCAS, W. and HOWSE, D. (1996): Activating flux—Increasing the performance and productivity of the TIG and plasma processes, *Welding and Metal Fabrication*, **64**, 5–9

LUYCKX, L., BELL, J., MCLEAN, A. and KORCHYNSKY, M. (1970): Sulphide shape control in high strength low alloy steels, *Metallurgical Transactions*, **1**, 3341–3350

MALINOWSKI-BRODNICKA, M., DEN OUDEN, G. and VINK, W. (1990): Effect of electromagnetic stirring on GTA welds in austenitic stainless steel, *Welding Journal*, **69**, 52s–59s

MARSHALL, P. (1984): Austenitic stainless steels—Microstructure and mechanical properties, Elsevier Applied Science Publishers Ltd., London

MCCARTNEY, D. (1989): Grain refining of aluminium and its alloys using inoculants, *International Materials Reviews*, **34**, 247–260

MILLER, G. (1959): Metallurgy of the rarer metals—Volume 6: Tantalum and niobium, Butterworths, London

MISCHLER, S., VOGEL, A., MATHIEU, H. and LANDOLT, D. (1991): The chemical composition of the passive film on Fe-24Cr and Fe-24Cr-11Mo studied by AES, XPS and SIMS, *Corrosion Science*, **32**, 925–944

MITROVIC-SCEPANOVIC, V., MACDOUGALL, B. and GRAHAM, M. (1987): The effect of Cl^- ions on the passivation of Fe-26Cr alloy, *Corrosion Science*, **27**, 239–247

MIX, P. (1987): Introduction to non-destructive testing—A training guide, John Wiley & Sons, New York

MOHANTY, P. and GRUZLESKI, J. (1995): Mechanism of grain refinement in aluminium, *Acta Metallurgica et Materialia*, **43**, 2001–2012

MORITA, Z. and KUNISADA, K. (1978): Solubility of nitrogen and equilibrium of titanium nitride forming reaction in liquid Fe-Ti alloys, *Transactions of the Iron and Steel Institute of Japan*, **18**, 648–654

MOTHERSILL, H. (1993): Consumable socket ring welding technology, *Welding and Metal Fabrication*, **31**, 380–381

MURATA, T. and SAKAMOTO, M. (1997): Nitrogen-alloyed steels—Fundamentals and applications, AGNE Publishing Inc., Tokyo

MUSGRAVE, M. (1954): On the propagation of elastic waves in aeolotropic media—1: General principles, *Proceedings of the Royal Society*, **226A**, 339–355

NIEWA, R., VAJENINE, G., DISALVO, F., LUO, H. and YELON, W. (1998): Unusual bonding in ternary nitrides—Preparation, structure and properties of Ce_2MnN_3, *Zeitschrift für Naturforschung Section B—Journal of Chemical Sciences*, **53**, 63–74

OSTROWSKI, A. and LANGER, E. (1979a): Influence of alloying elements on the as-cast structure of 17% chromium stainless steels, *Scandinavian Journal of Metallurgy*, **8**, 177–184

OSTROWSKI, A. and LANGER, E. (1979b): Precipitation of titanium carbonitrides in as-cast 17% chromium stainless steels, *Scandinavian Journal of Metallurgy*, **8**, 153–160

PASKELL, T., LUNDIN, C. and CASTNER, H. (1997): GTAW flux increases weld joint penetration, *Welding Journal*, **76**, 57–62

PEARCE, B. and KERR, H. (1981): Grain refinement in magnetically stirred GTA welds of aluminium alloys, *Metallurgical Transactions B*, **12B**, 479–486

PETCH, N. (1953): The cleavage strength of polycrystals, *Journal of the Iron and Steel Institute*, **173**, 25–28

PICKERING, F. (1976): Physical metallurgy of stainless steel developments, *International Metals Reviews*, **21**, 227–268

POLMEAR, I. (1995): Light alloys—Metallurgy of the light metals, 3rd edition, Edward Arnold, London

PORTER, D. and EASTERLING, K. (1992): Phase transformations in metals and alloys, 2nd edition, Chapman and Hall, London

QUAYLE, B. (1997): Unpublished research

RIVLIN, V. and RAYNOR, G. (1980): Phase equilibria in iron ternary alloys—1: Critical evaluation of constitution of chromium-iron-nickel system, *International Metals Reviews*, **25**, 21–38

ROBERTS, C. (1960): Magnesium and its alloys, John Wiley & Sons, New York

ROBERTS, T. (1994): Choosing materials for nuclear fuel reprocessing, *Materials World*, **2**, 628–631

ROCHOW, E. (1973): The chemistry of silicon, Pergamon Press, Oxford

RODRIGUEZ, F. (1982): Principles of polymer systems, 2nd edition, McGraw-Hill, New York

ROLLINSON, C. (1973): The chemistry of chromium, molybdenum and tungsten, Pergamon Press, Oxford

RYSHKEWITCH, E. (1960): Oxide ceramics—Physical chemistry and technology, Academic Press, New York

SALTER, W. (1979): Some aspects of the formation of sulphide inclusions in alloy steels, in *Inclusions, ed. Pickering, F.*, Institution of Metallurgists, Sheffield

SCHUMACHER, P., GREER, A., WORTH, J., EVANS, P., KEARNS, M., FISHER, P. and GREEN, A. (1998): New studies of nucleation mechanisms in aluminium alloys—Implications for grain refinement practise, *Materials Science and Technology*, **14**, 394–404

SCOTT, H. (1975): Phase relationships in the zirconia-yttria system, *Journal of Materials Science*, **10**, 1527–1535

SCOTT-LAWSON, W. (1975): Microstructure of modulated current TIG welds in stainless steel, *The Welding Institute Research Bulletin*, **16**, 125–130

SEGAR, R. (2000): Dissertation to be submitted for the degree of Doctor of Philosophy, University of Cambridge

SHREIR, L., JARMAN, R. and BURSTEIN, G. (1994): Corrosion—Volume 1: Metal/environment reactions, 3rd edition, Butterworth-Heinemann, Oxford

SILK, M. (1987): The ultrasonic inspection of difficult materials, in *Non-destructive testing, eds. Farley, J. and Nichols, R.*, Pergamon Press, Oxford

STEIN, G. and MENZEL, J. (1995): Nitrogen-alloyed steels—A new generation of materials with extraordinary properties, *International Journal of Materials and Product Technology*, **10**, 290–302

SUGDEN, A. and BHADESHIA, H. (1988): The non-uniform distribution of inclusions in low-alloy steel weld deposits, *Metallurgical Transactions A*, **19A**, 669–674

SUMITO, M., TSCHIYA, N., OKABE, K. and SANBONGI, K. (1981): Solubility of titanium and carbon in molten steel Fe-Ti alloys saturated with carbon, *Transactions of the Iron and Steel Institute of Japan*, **21**, 414–421

SVENSSON, L. (1994): Control of microstructures and properties in steel arc welds, CRC Press Inc., Boca Raton, Florida

TEWARI, S. (1993): Influence of vibration on grain size and degree of grain refinement in mild steel weldments, *Journal of Materials Research*, **8**, 2228–2230

TEWARI, S. (1999): Effects of transverse oscillation on tensile properties of mild steel weldments, *ISIJ International*, **39**, 570–574

TILLER, W., JACKSON, K., RUTTER, J. and CHALMERS, B. (1953): The redistribution of solute atoms during the solidification of metals, *Acta Metallurgica*, **1**, 428–437

TILLER, W. and RUTTER, J. (1956): The effect of growth conditions upon the solidification of a binary alloy, *Canadian Journal of Physics*, **34**, 96–121

TILLER, W. and TAKAHASHI, T. (1969): The electrostatic contribution in heterogeneous nucleation theory—Pure liquids, *Acta Metallurgica*, **17**, 483–496

TOMLINSON, J., WAGG, A. and WHITTLE, M. (1980): Ultrasonic inspection of austenitic welds, *British Journal of Non-destructive Testing*, **22**, 119–127

TURNBULL, D. and CECH, R. (1950): Microscopic observation of the solidification of small metal droplets, *Journal of Applied Physics*, **21**, 804–810

TURNBULL, D. and VONNEGUT, B. (1952): Nucleation catalysis, *Industrial and Engineering Chemistry*, **44**, 1292–1298

UNDERWOOD, E. (1970): Quantitative stereology, Addison-Wesley, Reading, Massachusetts

UPADHYAYA, G. (1996): Nature and properties of refractory carbides, Nova Science Publishers Ltd., New York

VANDER-VOORT, G. (1984): Metallography—Principles and practise, McGraw-Hill, New York

VELARDE, M. and NORMAND, C. (1980): Convection, *Scientific American*, **243**, 78–93

VILLAFUERTE, J. and KERR, H. (1990a): Electromagnetic stirring and grain refinement in stainless steel GTA welds, *Welding Journal*, **69**, 1s–13s

VILLAFUERTE, J. and KERR, H. (1990b): Grain structures in gas tungsten arc welds of austenitic stainless steels with ferrite primary phase, *Metallurgical Transactions A*, **21A**, 979–986

VILLAFUERTE, J., KERR, H. and DAVID, S. (1995): Mechanisms of equiaxed grain formation in ferritic stainless steel gas tungsten arc welds, *Materials Science and Engineering*, **A194**, 187–191

WADE, K. and BANISTER, A. (1973): The chemistry of aluminium, gallium, indium and thallium, Pergamon Press, Oxford

WATANABE, T., NAKAMURA, H. and EI, K. (1987): Grain refinement of austenitic stainless steel welds by pulsed TIG welding, *Transactions of the National Research Institute for Metals*, **29**, 204–211

WEISSMANN, S., POST, B., MORSE, M., MCMURDIE, H., MORRIS, M. and MCLUNE, W. (eds.) (1978): Metals and alloys data book, JCPDS, Swarthmore, Pennsylvania

WEITZER, F. and SCHUSTER, J. (1987): Phase diagrams of the ternary systems Mn, Fe, Co, Ni-Si-N, *Journal of Solid State Chemistry*, **70**, 178–184

WHITING, A., GREER, A. and MCELROY, J. (1978): The difficulties of applying non-destructive evaluation to stainless steel components in the nuclear industry, in *Non-destructive evaluation in the nuclear industry, ed. Natesh, R.*, American Society for Metals, Ohio

WILSON, W., KAY, D. and VAHED, A. (1974): The use of thermodynamics and phase equilibria to predict the behaviour of the rare-earth elements in steel, *Journal of Metals*, **26**, 14–23

WILSON, W. and WELLS, R. (1973): Identifying inclusions in rare-earth treated steels, *Metal Progress*, **104**, 75–77